Nuclear Structure, Nuclear Reactions

Maria Cristina Berisso de Etchegoyen

Wolfson College

Thesis submitted for the degree of Doctor of Philosophy
University of Oxford

February 1982

BODLEIAN LIBRARY OXFORD
DEPOSITED
THESIS
8 · 2 · 83

Addenda

p.37	Table 3.1 lower part: There is no 0^+ $(sd)^4$ cluster state in ^{18}F.
p.41	Second sentence: in particular changes by a factor 2 in spectroscopic factor can occur.
p.52	Subsequent analyses showed that the proton and deuteron decays arise from background states.
Fig.3.9	The $J^\pi = 5^+$ and 7^+ theoretically calculated correlations are incorrectly plotted: the correct curves show a shift in symmetry axis towards larger angles for lower spin assignments.
p.73 Tab.4.3 Fig.4.6	Although it is true that the total cross-section only differs by 5.8%, this is not relevant to the experiment where angular distributions over a limited angular range have been measured. In table 4.3 a 12% discrepancy exists for $d\sigma(20^\circ)$, and from Fig.4.6 it is clear that the comparison between post and prior calculations is most favourable at 20° compared to other angles in the range $10^\circ - 40^\circ$ for which data exist.
p.102	End of first paragraph: high spin assignments give a displacement of the symmetry axis towards smaller angles than low spin assignments. (e.g. $\Theta_{cms} = 45^\circ$ for $3/2^+$ states and $\Theta_{cms} = 15^\circ$ for $15/2^+$ states).
p.112	A.1.8(b) should be $m_{s''} + m_{\ell''} = m_{I'}$

References:

p.3	Delete ART71, ART74 and ART75.
p.34	Delete '(as found by Buck and Tomusiak (BUC74))'.
p.43	Delete ART71
p.57	BUC77b should be BUC77a.
p.69	KUB71 should be KUB72.
p.87	BIN71 should be BIN73 (twice)
p.135	Delete BUN64.
p.144	Add RAE76: W.D.M. Rae D.Phil Thesis, Oxford 1976, unpublished.

Para Alberto

ABSTRACT

In this thesis, particle - particle angular correlations for reactions in non-zero degree geometry and with non-zero spin nuclei are performed and found to be a valuable tool for spin determination. (d-α) angular correlations in the reaction process $^{14}N(^{6}Li,d)^{18}F^{*}$ $(\alpha)^{14}N$ are measured for three high excited states in ^{18}F with a ^{6}Li beam of 36MeV. Spins and parities for two of the observed states are determined, and in agreement with theoretical predictions, these states are suggested as members of the $K^{\pi}=1^{+}$ α-rotational band. The three analysed 9.58MeV 6^{+}, 11.2MeV, 14.1MeV 8^{+} states are found to undergo a predominant α-particle decay to the ground state of ^{14}N. Gamow unbound formalism is carried out for the state descriptions. Angular distributions are measured and analysed under Hauser Feshbach and exact finite range DWBA formalisms. Spectroscopic factors are extracted and compared to shell model predictions, showing a reasonable agreement.

(^{3}He-α) and (t-α) angular correlations for the reaction processes $^{14}N(^{6}Li,^{3}He)^{17}O^{*}$ $(\alpha)^{13}C$ and $^{14}N(^{6}Li,t)^{17}F^{*}$ $(\alpha)^{13}N$ respectively are measured at 36MeV of ^{6}Li. High selectivity is observed for the three particle transfer processes and percentages of the different particle decays for the high populated states are presented. Structureless angular correlations hinder definite spin and parity assignements, but the displacement of the preferred direction observed in the pattern decay gives some information on the range of plausible angular momenta. Shell model calculations are performed for comparison with the experimental data, and this allows tentative spin identifications. EFR DWBA calculations are carried out, providing some confirmation on the spin suggestions. Useful nuclear structure information is obtained for the mass 17 and 18 nuclear states.

The particle-particle angular correlation expression for a process where a direct reaction mechanism is involved is reviewed, programmed and used for obtaining the theoretical predictions to be compared to the experimental results.

ACKNOWLEDGEMENTS

I would like to express my gratitude to all the people who have helped in the work for this thesis and who have supported me throughout my stay as a postgraduate at Oxford. In particular I am indebted to the following:

Professor K.W.Allen (former Head of the Laboratory) and Professor D.H.Perkins for allowing me the use of the facilities at the Nuclear Physics Laboratory.

My supervisor, Dr D.Sinclair for his help and always valuable advice throughout this research and for being an almost endless source of new ideas for improving the conditions of the experiment and the data acquisition methods. Dr B.E.Cooke for his constant interest and guidance on experimental design and data analysis during the first year of my stay in Oxford. Mr M.Mineter for his help in prelimimary runs and for providing a VAX working version of STATIS. Mr A.Etchegoyen and Mr E.Belmont-Moreno for their valuable help in the definitory and almost interminable runs. Dr N.Godwin who tought me the techniques of gas cell making and the first steps in handling DWBA and shell model codes. Mr C.Graham and his group of experts for their assistance in manufacturing innumerable pieces of equipment. Mr T.W.Thacker for his help and patience with my computational work. Mr R.Hunt who constructed indispensable CAMAC equipment. Mr R.Evans and the machine operators for their expert assistance in running the experiments.

Drs B.A.Brown, M.Kawai, K.I.Kubo and P.Grossman for very helpful discussions on shell model, DWBA theories and statistics. Dr B.Buck and Dr K.Snover for their patience, interest and help in decay and angular correlation theories.

I would like to thank specially my husband, Alberto, who has been undoubtly a permanent source of support and help in running experiments and in theoretical discussions. The Comision Nacional de Energia Atomica for allowing me to come to Oxford and for the financial support troughout these years. In particular Dr E.Maqueda, Dr G.Dussel, Dr D.Bes and Dr O.Dragun for their trust, support, and endless efforts on helping their graduates.

My brother and systers in law, Ramon, Laura and Alicia for their patient encouragement, and Julian and Lucia for their help. Finally and with special gratitude, my parents for their trust and love throughout my career.

Contents

CHAPTER 4 $^{14}N(^{6}Li,d)^{18}F$. The Reaction Mechanism.

4.5 DWBA Calculations

CHAPTER 5 Three Particle Transfer Reactions on ^{14}N

APPENDIX A

CHAPTER 1

Introduction

Multinucleon transfer reactions induced by high energy heavy ions have proved to be a useful tool for studying the structure of light nuclei. The high selectivity in the types of nuclear configurations that are populated in these reactions is one of the most striking features. Particle-hole configurations and clustering phenomena in the final states can be disclosed when comparing the predictions of microscopic and macroscopic collective models to the experimental data.

Several investigations on four and three particle cluster structure have been performed lately. α-transfer reactions as (^{6}Li,d) and (^{7}Li,t) for example have shown almost invariably a high selectivity in the final state population of light nuclei [MID68, MEI68,COB76, CUN81]. Some three particle transfer reactions (^{6}Li,t) and (^{6}Li,^{3}He) indicated [BIN73] a high selectivity as well, produced by a predominant three nucleon transfer mechanism. This provides a very important tool for studying states of prevailing three-nucleon configurations. With the experimental evidence of substantial three and four particle clustering in the sd-shell nuclei, many rotational bands with J(J+1) energy dependence have been identified and many different models have been suggested to describe these cluster states. They range from the shell model with SU(3) configurations to simple cluster models as the folded potential model introduced by Buck Dover and Vary (BDV) [BUC75]. However, the description of the structure of the states and of the processes involved in terms of theoretical models is in many cases hindered by the lack of definite spin-parity assignments.

Some α-transfer experiments on ^{14}N, performed at Harwell [BRA77] with ^{13}C(105MeV) and ^{11}B(115MeV) incident beams, had shown strong population of ^{18}F states between 9 and 16 MeV of excitation energy. Very similar spectra were obtained with the two reactions. Two new states were identified at 14.18MeV and 15.8MeV, but no detailed study of these states was possible and further experimental as well as theoretical work on α-transfer on ^{14}N was suggested. Four and three nucleon transfer reactions on ^{14}N were performed in preliminary runs at 24MeV, 30MeV and 36MeV of ^{6}Li incident ion with the Oxford Folded Tandem accelerator. A highly selective behaviour was found for the three analysed transfer reactions (^{6}Li,d), (^{6}Li,t) and (^{6}Li,^{3}He). For the alpha transfer, four highly populated states were identified. The lowest at 6.56MeV is the already known 5^+ member of the $K^\pi=1^+$ band in ^{18}F. Two other states, 9.58MeV and 11.2MeV show very good agreement with the energy values predicted by Buck et al. [BUC77] for the 6^+ and 7^+ members of the same rotational band. A fourth strong populated state appears at 14.1MeV of excitation energy. The fairly high counting rate observed for the peaks of interest, suggests particle - particle angular correlations as a plausible method for spin determination. Angular correlations are indeed a well established method for spin assignment. In an early work by Litherland and Ferguson [LIT61] it was shown that for reactions when all nuclei but the recoil nucleus have spin zero and the ejectile is detected in the beam direction, the particle-ejectile angular correlation is independent of the reaction mechanism and characteristic of the recoil nucleus spin. The choice of spinless particles and of a zero-degree geometry allows only m=0 magnetic substates of the intermediate states to be populated, and under these conditions, the decay of a J spin state in the recoil nucleus has a simple $|P_J(\theta)|^2$ angular correlation shape. Further studies on particle - particle correlations free from Litherland's restrictions have proved that non-zero degree geometries with non-zero spin projectile and ejectile provide substantial information on the reaction mechanism involved as well as spin assignments. Predominant population of the m=0 magnetic substate for example can also be achieved in α-transfer reactions where the incident projectile has non-zero spin, and the ejectile is detected away from zero-degrees, provided that the rest of the projectile behaves as a simple spectator. Thus reducing the problem to one of having a beam of alpha particles impinging on the target in the recoil direction.

The non-zero degree geometry (depicted in figure 1.1) has been extensively used with (^{6}Li,d) and (^{7}Li,t) reactions to determine spins of ^{16}O and ^{20}Ne states [ART71, PAN74, ART74, AVR75, ART75]. For all ^{16}O and ^{20}Ne levels analysed in the literature, a simple $|P_J(\theta)|^2$ dependence is assumed for the angular correlations, since the theoretical expressions are greatly simplified by the use of zero-spin target and daughter nuclei. The simplicity of the experimental techniques required when detecting away from the beam direction (conventional ΔE-E telescopes can be used) shows a clear advantage of the non-zero degree geometry. Even more, the study of the displacement of the symmetry axis for the sequential decay from the recoil direction provides in some cases [LAM71] the necessary information to select the reaction mechanism

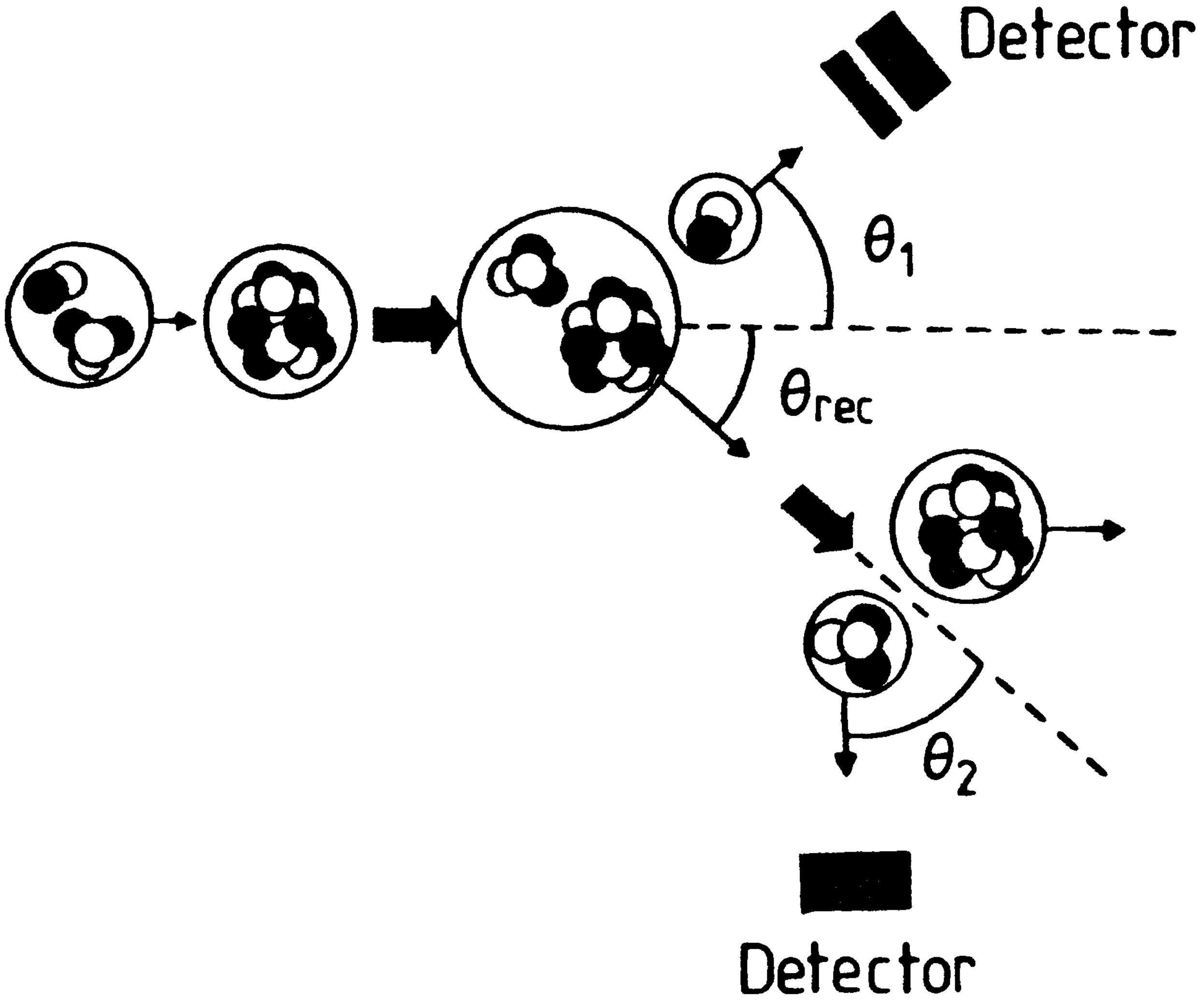

Figure 1.1 Particle-particle angular correlation in the non-zero degree geometry

involved.

To our knowledge, all previous experimental analyses of particle - particle angular correlations are restricted to zero spin target and daughter nuclei, and assume for the theoretical angular correlation a simple dependence on Legendre polynomials. Unbound states are fictitiously bound to small binding energies when transition amplitudes are required for estimating magnetic substate populations. It has been one of the aims of this thesis work to study angular correlations without any of the above mentioned restrictions.

When the spins of target, projectile, ejectile and daughter nuclei are different from zero, the theoretical expression for the angular correlation is not a simple $|P_J(\theta)|^2$, but for many cases a structure characteristic of the spin of the recoil nucleus is observed, and this can be used for spin determination.

Our experimental work is centred on (^{6}Li,d), (^{6}Li,t), (^{6}Li,^{3}He) reactions on ^{14}N gas targets. The particle decay of the highly populated states in the recoil nucleus is observed aiming at spin and parity assignments. The angular distributions for the primary reactions are studied as well, for adding completeness to the suggested assignments.

The work is organized as follows: in Chapter two, a description of experimental apparatus and techniques employed in angular distribution and angular correlation measurements is given. Particle identification, coincidence electronic circuits and the effect of the geometry of the detection system as well as the working conditions of the gas target in the energy resolution are described.

In Chapter three, the decay of excited states in ^{18}F is studied. Considering that the main reaction mechanism involved is the direct mode, theoretical angular correlations for the alpha decay of the recoil nucleus are estimated. Calculations are performed for different natural and unnatural parity states and the results compared in a χ^2 analysis to the experimental angular correlations. Percentages of alpha, proton and deuteron emission are quoted for each of the analyzed ^{18}F states.

In Chapter four, the experimental angular distributions and the theoretical compound nucleus and direct transfer predictions are shown. The α-unbound ^{18}F states are described in terms of Gamow wave functions, since simplified prescriptions for such states do not seem to be satisfactory for use in the distorted wave Born approximation (DWBA). Four nucleon spectroscopic factors are calculated by overlapping shell model wave functions to those of SU3 states, and compared to the experimentally deduced spectroscopic information. The shell model calculations are performed with a closed ^{12}C core and active p1/2, d5/2 and s1/2 shells, and the DWBA calculations are carried out using an exact finite range code. All nuclear and Coulomb interaction terms, usually neglected for one particle transfer calculations, are included in the estimation of transition amplitudes.

In Chapter five, the work on three nucleon transfer into mass 17 is presented. (^{6}Li,t) and (^{6}Li,^{3}He) reactions to mirror levels in ^{17}F and ^{17}O show large cross sections for states between 8 and 15 MeV of excitation. Experimental angular correlations are compared to DWBA predictions. The particle decay from the high populated states is followed, and alpha - angular correlation data obtained. For the theoretical calculation of the decay pattern, the complexity in the description of the intermediate states in the recoil nucleus (three cluster angular momenta to be considered for each recoil nucleus spin), makes indispensable the information on spectroscopic amplitudes. Shell model wave functions are calculated, the overlaps with SU(3) states are performed, and spectroscopic amplitudes estimated. EFR-DWBA calculations containing the theoretical spectroscopic information are compared to the experimental angular distributions and the relevant normalization factors presented. Theoretical angular correlations based on a predominant direct three nucleon transfer mechanism are calculated and compared to the experimental angular correlations.

Finally the conclusions are presented. Computational codes were written in order to account for a general angular correlation expression where non-zero degree geometry as well as non-zero spin particles can be considered. The unbound state treatment for the recoil nucleus is explicitly taken into account by including Gamow wave functions in the form factor of DWBA calculations, and therefore very realistic reduced amplitudes are used in the theoretical estimation of angular correlations. The theoretical expressions from which the programs were derived are deduced in this Appendix.

Appendix B gives highlights of the theory of cluster transfer in DWBA calculations, and Appendix C shows details of the use of Gamow unbound states in the DWBA transition amplitude formalism.

CHAPTER 2

Experimental Techniques and Apparatus

2.1 Introduction

The experiments analysed in this thesis work were performed at the Oxford Nuclear Physics Laboratory using the Folded Tandem accelerator with 36 MeV ^{6}Li ion beams and typical currents of 150-400 nAmps. Ejectiles and decay particles resulting from different reactions were detected in fully depleted silicon surface barrier detectors. Angular distributions as well as angular correlations were measured with two different experimental techniques: a) for detecting the ejectiles in angular distributions measurements, a standard particle identification technique based in a "telescope" assembly of two solid state silicon surface barrier counters was used and b) for the angular correlation measurements, a particle-particle coincidence technique between the light reaction product detected in the telescope with a subsequent decay particle from the recoil nucleus detected in any out of five single silicon surface barrier counters was used.

The design of the detection systems, description of the experimental lay-outs, apparatus, techniques and energy resolution are given in the following sections.

2.2 The Scattering Chamber

A schematic arrangement of the scattering chamber is shown in figure 2.1. A spherical scattering chamber with an internal diameter of 1.0 meter was used, with a gas cell situated at the centre and connected to the external gas handling system. A rotary pump and two nitrogen cooled cold traps were used to reach the starting pressure conditions required by a turbo pump, which, coupled to the already mentioned rotary pump would maintain an average operating pressure of 10^{-6} torr. The size and direction of the incident beam was defined by a 1.5 mm × 4 mm collimation system. In order to minimize the beam spreading across the target, an attachment for the already existent sliding collimator mounting was designed, which allowed the collimator slits to be placed as close as possible to the gas cell entrance window. The beam collimation system, the gas target position, and the detection collimation systems were optically aligned with the use of a theodolite. The scattering chamber has a horizontal rotating plate which allows to position detectors as far as 36 cm from its geometrical centre. In order to have independent movements for the different detection systems in the reaction plane to be commanded externally , a new rotatory hanging detector support was designed and coupled to an absolute shaft encoder for the angle reading. The already existent rotating plate as well as the new implemented supporting arm were remotely controlled by a VAX 11 computer and, with the use of the encoder, the angle was determined within 0.02°.

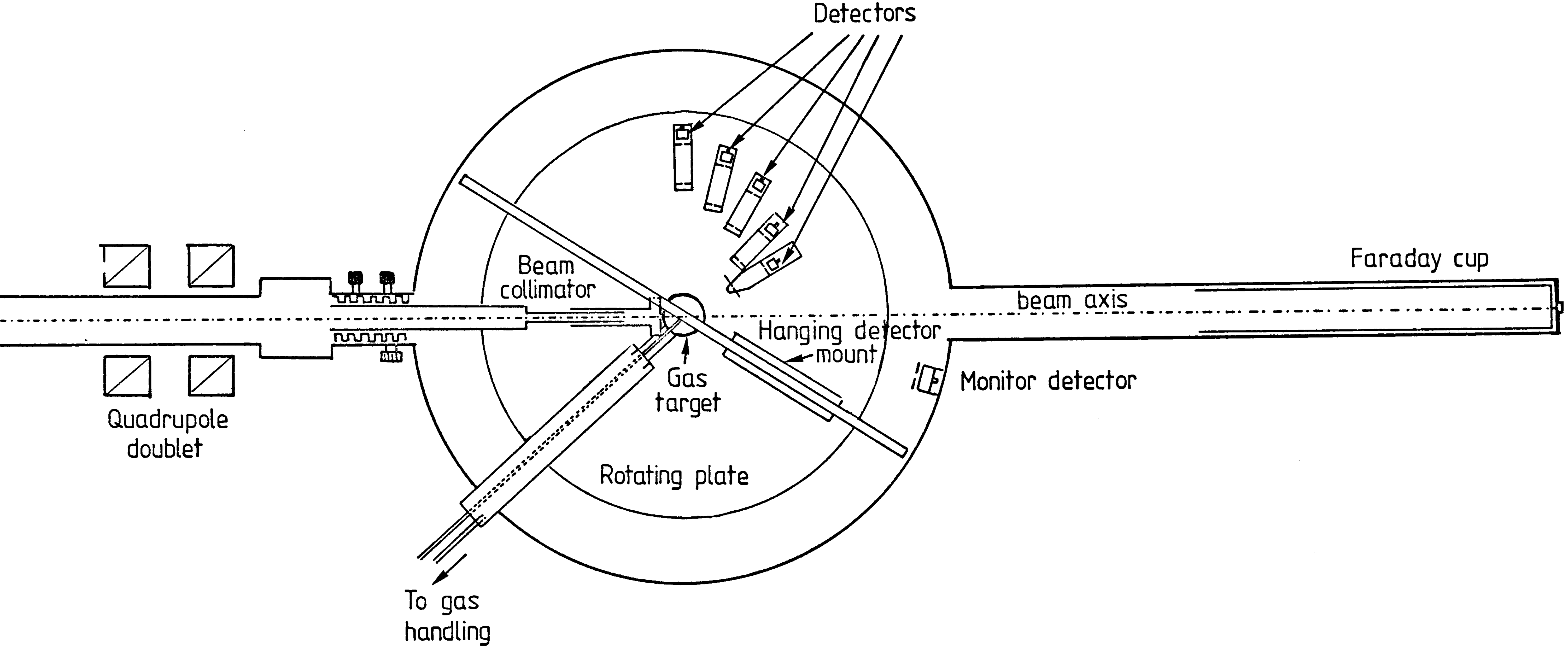

Figure 2.1 Schematic arrangement of scattering chamber.

The undeflected particles were collected in a 1.2 meter long Faraday cup whose entrance was situated at 1.8 meters from the centre of the chamber and the current striking the cup was integrated by an Ortec current digitizer. Since at the beam energies used in these experiments the ions were fully stripped of their electrons after passing through the target [MAR68] the incident beam exposure was calculated directly from the total charge collected in the Faraday cup. Due to the big length of the Faraday cup, and its position far away from the chamber centre, no suppression grid voltage was necessary in order to ensure collection of electrons inside the Faraday cup, and rejection of electrons produced in the target. An estimation of the effects of using suppression voltages ranging from 150V to 750V on this line, was performed recently [WOO81] and it showed less than 4% deviation in the integrated beam current.

Although a monitor detector with a single collimator would not have viewed the same region of gas target as seen, for example, by the telescope detector, they were used in elastic scattering measurements to give dead time corrections, and as an independent check of the Faraday cup beam current at different beam intensities in order to obtain the linearity in the Faraday cup response before each angular correlation experiment.

2.3 The Gas Target and the Detector Collimation System

For both angular correlations and angular distributions one gas cell design was used and it is illustrated in fig. 2.2. It consists of a cylindrical aluminium base with a top lid to which the gas connector is fixed. It is sealed with an O-ring. The gas cell has an internal diameter of 6 cm, a small rectangular aperture of 1.2 cm × 1.3 cm as entrance window and a wide exit side window of 1.2 cm × 7.2 cm. The apertures subtend angles of 24°49' and 137°30', respectively allowing a wide range of detection angles. The cylindrical entrance and exit windows consisted of thin aluminium foils 5 μm thick which for the incident ^{6}Li ion beam and the outgoing particles deuterons, tritons, ^{3}He and ^{4}He do not affect the total energy resolution as the straggling in the windows is low. On the other hand, this 5 μm Al foils, bonded to the gas cell with Araldite, can withstand differential pressures of 100 to 150 torr. During the runs the gas cell pressure was monitored continously with a closed circuit television camera set on a standard 0 to 760 torr pressure gauge. The detector collimation system for gas cells consist schematically of three collimators. The front collimator (closest to the exit gas cell window) and back collimators (closest to the particle detectors) define the region of the gas cell under observation (i.e the actual target) while the middle collimator screens the detectors from particles originating on the gas cell windows. A gas cell with large radius (as the one used in the present experiments) would allow particle detection at very forward laboratory angles (~ 8°) with no significant scattered particles from the window entering a

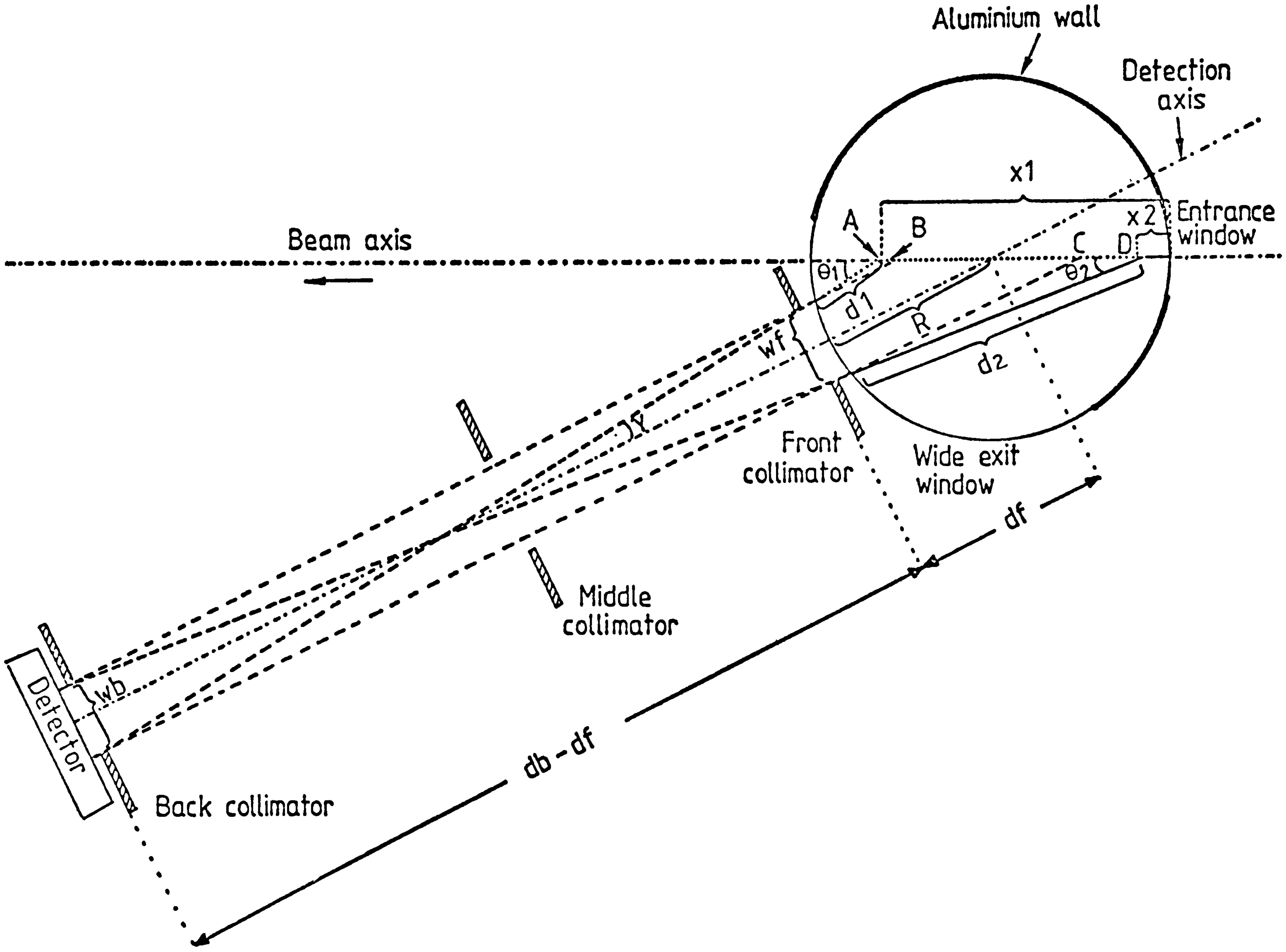

Figure 2.2 Gas cell and detector collimation system. Different rays entering the detection system are shown. The two extreme paths followed by the ions in the gas cell are plotted in solid line and dots.

detector. The position and slit sizes of the front and back collimator as well as the working gas pressure must be carefully selected with a compromise between counting rate and energy resolution. Wide collimator slits and higher gas pressures would increase the counting rate at the expenses of the loss of energy resolution by kinematical broadening (dependance of the ejectile energy with its detection angle), differences in path lengths within the gas cell resulting in different energy losses and straggling in the gas. Positions and slit widths for the collimators were obtained using this criteria and estimating the total energy resolution for different values.

2.4 Energy Identification and Resolution

In its path across both the gas and the gas cell metal windows the incident 36 MeV ^{6}Li beam loses energy. Reactions taking place at different points in the line BC shown in fig. 2.2 would have different average incident energy for the ^{6}Li ions. A kinematical calculation should take into account such variations in order to give more accurate energy estimations for the outgoing particles. At the same time, the different particles resulting from the reaction have to cross certain portion of the gas cell in order to reach the detectors. In order to identify the actual excitation energy of a recoil nucleus associated to the energy left by the ejectile in the detection system, all these energy losses have to be considered. Figure 2.2 shows a diagram of the two extreme paths defined by the collimation system in the gas cell. The two extreme trajectories followed by beam and emerging particles can be geometrically estimated with the gas cell radius and position and width of the collimation slits:

$$x_1 = R + df \times \cos(\Theta) - XF + Wf \times \sin(\Theta)/2 \qquad (2.1)$$

$$x_2 = R + df \times \cos(\Theta) - YF - Wf \times \sin(\Theta)/2 \qquad (2.2)$$

$$d_1 = d_{\ell 1} - (x_1 - R) \times \cos(\Theta_1) \qquad (2.3)$$

$$d_2 = d_{\ell 2} + (R - x_2) \times \cos(\Theta_2) \qquad (2.4)$$

$$\gamma = \mathrm{arctg}\left(\frac{Wf + Wb}{2(db - df)}\right) \qquad (2.5)$$

with

$$\Theta_1 = \Theta + \gamma \qquad (2.6)$$

$$\Theta_2 = \Theta - \gamma \qquad (2.7)$$

$$XF = (df \times \sin(\Theta) - Wf \times \cos(\Theta)/2) \times \sin(\pi - \Theta_1)/\sin(\Theta_1) \qquad (2.8)$$

$$YF = (df\times\sin(\Theta) + Wf\times\cos(\Theta)/2)\times\sin(\pi-\Theta_2)/\sin(\Theta_2) \qquad (2.9)$$

$$d_{\ell 1} = (R^2 - ((x_1 - R)\times\sin(\Theta_1))^2)^{\frac{1}{2}} \qquad (2.10)$$

$$d_{\ell 2} = (R^2 - ((R - x_2)\times\sin(\Theta_2))^2)^{\frac{1}{2}} \qquad (2.11)$$

The different energy losses along paths x_1 and x_2 can be estimated with the semi-empirical Bethe-Bloch formula. This calculation would then give the energy of the beam at the points A and D (see fig. 2.2) which can be, in turn, used to estimate the energy on reaching the detector of particles scattered through Θ_1 and Θ_2. It is very important to evaluate the energy spread in an effort to optimise the compromise between energy resolution and counting rate (i.e., the choice of acceptable collimation parameters). The contributions to the energy resolution are:

i) energy spread of the beam,
ii) energy straggling in windows and gas,
iii) energy spread due to the reaction taking place in different positions within the gas cell,
iv) kinematical broadening,
v) energy resolution of the detectors,

and

vi) energy resolution on the electronics.

Contribution ii), iii) and iv) can be estimated from the characteristics of the materials employed for the entrance and exit windows, the geometry of the collimation system and the working conditions of the gas cell. The energy spread due to differences in paths and kinematical broadening can be immediately obtained calculating the energy losses across gas and windows. The energy spread due to straggling in windows can be expressed as [HAM76]:

$$\Gamma_w = 0.811\ z \left(\frac{\rho_w\ Z\ \ell}{A_w\ \sin\alpha}\right)^{\frac{1}{2}} \quad \text{(MeV)} \tag{2.12}$$

where ρ_w and A_w are the density (in gr/cm^3) and the atomic weight of the material of the windows, ℓ is the path length (in cm) of the ion through the window, α is the angle of incidence to the window and z, Z the charges of the ion and window material, respectively. The energy straggling in the gas was estimated with [HAM76]:

$$\Gamma_s = 3.248\times10^{-3}\ z \left(\frac{Z\ m\ P\ \ell}{T}\right)^{\frac{1}{2}} \quad \text{(MeV)} \tag{2.13}$$

where m is the number of atoms per molecule, P is the pressure in Torr and T is the absolute temperature of the gas.

In order to perform the calculations labelled ii), iii) and iv) a computer code was written. This computer code also enables one to calculate with considerable accuracy the expected ejectile energies for different excited states of the recoil nucleus and to work backwards to the energy levels of the heavy products of the reactions based on the spectra of the outgoing ejectiles. The program uses an already available subroutine [RAE76] to integrate the Bethe-Bloch equation.

Due to the characteristics of the reactions studied in this thesis (light-heavy projectiles, light reaction products and maximum gas pressures of ~ 150 torr) the most important contributions to the loss of energy resolution are: kinematical broadening and energy losses due to different paths. Table 2.1 shows some energy spread values obtained for

Table 2.1

Energy Spread Contributions for the $^{14}N(^{6}Li,d)^{18}F^{*}$(11.2MeV) Reaction.

Angle of detection (degrees)	Slit front collimator (cm)	Slit back collim. (cm)	gas pressure (Torr)	Straggling ent. wind. (MeV)	Strag. in gas (beam) (MeV)	Kinematic broad. (MeV)	Strag. in gas (eje) (MeV)	Strag. in exit win. (MeV)	Path difference (MeV)	Total resolution (MeV)	Average energy of ejectile (MeV)
10	0.2	0.2	100	0.062	0.036	0.143	0.012	0.020	0.136	0.219	23.40
10	0.1	0.1	100	0.062	0.037	0.072	0.012	0.020	0.068	0.148	23.40
10	0.2	0.2	150	0.062	0.045	0.203	0.015	0.020	0.192	0.284	23.27
10	0.1	0.1	150	0.062	0.046	0.101	0.015	0.020	0.096	0.182	23.26
30	0.2	0.2	100	0.062	0.037	0.128	0.012	0.020	0.126	0.204	21.94
30	0.2	0.2	150	0.062	0.037	0.128	0.015	0.020	0.143	0.228	21.81
30	0.1	0.1	100	0.062	0.037	0.064	0.012	0.020	0.063	0.140	21.94
30	0.1	0.1	150	0.062	0.046	0.073	0.015	0.020	0.072	0.155	21.81

the $^{14}N(^{6}Li,d)^{18}F^{*}$ reaction, populating a ^{18}F excited state at 11.2 MeV and under different experimental conditions. The values which have been kept fixed in the different calculations are the distances of front and back collimator from the target centre (3.3 cm and 29.2 cm), the gas cell radius (3 cm), gas temperature (20°C) and characteristical figures for Aluminium windows 5 μm thick. The angle of detection is given in the laboratory frame and the incident energy of the ^{6}Li beam is 36 MeV. It can be clearly seen that the poorest resolutions arise for small laboratory angles and therefore these angles will set the limit in the energy resolution. For all cases the kinematical broadening and the path difference spread are seen to be the most important sources of loss of energy resolution.

2.5 Particle Detection

In the coincidence experiments as for the angular distribution measurements as well, a ΔE-E telescope detector was used in order to identify the ejectiles of the different nuclear reactions that were present. This particle identification technique is based on the energy lost by an ion passing through fully depleted silicon surface barrier detectors. When an ion transits a thin ΔE detector followed by a thick E detector (where it is completely stopped), each counter produces signals proportional to the energy lost by the charged particle. The addition of the two gives the total energy carried by the ion when entering the telescope system. The technique followed is based in the empirical relationship [ARM69] between the ion energy, E_{tot} and its range R in a given material:

$$R = \frac{A\, E_{tot}^{k}}{M^{k-1}\, Z^{2}} \tag{2.14}$$

where A is a characteristic constant of the stopping material, M and Z are the mass and the charge of the particle, respectively. k is a constant taken as 1.68 for all the ions (deuterons to ^{6}Li). Let us now assume that the ion being detected loses ΔE MeV in the first detector which has a thickness R_1 and that the remaining residual energy E, is lost in the second detector. We define the particle identification signal (PI) as:

$$PI = (\Delta E + E)^k - E^k = \frac{M^{k-1}\, Z^2}{A} (R_1 + R_2) - \frac{M^{k-1}\, Z^2}{A} R_2 =$$

$$= \frac{M^{k-1}\, Z^2}{A} R_1 \qquad (2.15)$$

The ΔE detector thickness must be carefully selected thin enough to allow the heavier particles of interest to pass through yet thick enough to allow the lighter particles to lose a considerable amount of energy compatible with the lower discriminator levels of the electronic circuit. The E detector has to be thick enough as to be able to stop the lightest particles of interest. Therefore, kinematical calculations for the reactions involved have to be performed and the range of expected energies for the different outgoing particles estimated. When measuring elastic scattering, where ^{6}Li ions have to be detected, a special set of ΔE-E detectors was used in order to improve the detection conditions: a thin 73.2 μm ΔE detector and a thick 2.2 mm E detector. The angular distributions and the angular correlations measurements were performed with another telescope assembly. For these measurements the aim was to detect light ejectiles and therefore a 200 μm thick ΔE detector and 4.1mm thick E detector were used. The ΔE detector would completely stop the elastically scattered particles.

An anular α source of ^{241}Am placed between the two detectors was used for checking the detector depletion voltages and for calibration purposes. Obviously, as a coincidence between the ΔE and E detector was required, this α signals did not introduce spurious pulses. The above mentioned coincidence signals were processed on-line and stored on magnetic tape for a further and more detailed off-line analysis. In particular, a spectrum of the previously defined PI signal is shown in fig. 2.3.

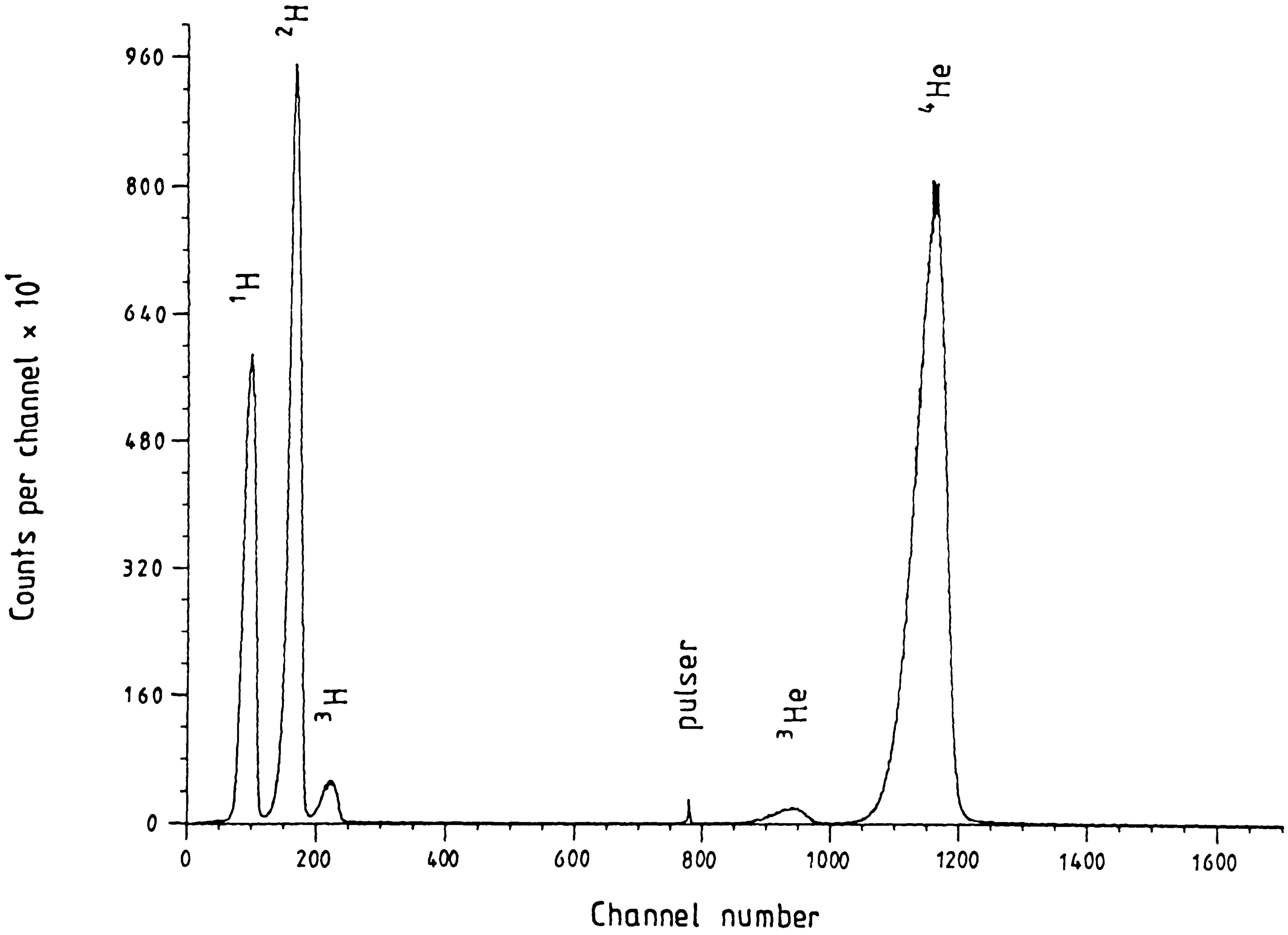

Figure 2.3 Particle identification spectrum.

2.6 Angular Distribution Experiments

2.6.1 Experimental Set up and Electronics

The typical experimental arrangement consisted in a telescope detector situated on the rotating plate of the scattering chamber, a collimation system of front, middle and back tantalum collimators of 0.2 cm slit width at 5 cm, 10 cm and 25 cm from the target centre, respectively. The gas cell, 3 cm in radius and with 5 μm thick aluminium windows, was operated at 100 torr. The gas was ^{14}N 99.5% purity. The telescope was placed at 8°, 9°, 11°, 12°, 14°, 16°, 18°, 20°, 23° and 26° from the beam direction in the laboratory system. The beam intensity was 60 - 80 nAmp. The electronic circuit used is shown in fig. 2.4. The timing was set up with a precision pulser. The gains in the ΔE and E detector were fix to matching values which allowed the expected energy range of the different particles to fit in 2048 channels. The pulses from the ΔE and E detectors were amplified and directly sent to fast Silena analog to digital converters (ADCs). The logic signals obtained from pulses above noise level were sent to a coincidence box and the output signals obtained when this requirement was fulfilled gated the ADCs in a delayed coincidence mode. The dead time corrections were carried out with the use of a precision pulser triggered externally by the output signal of the Faraday cup current digitizer (lower part of fig. 2.4). The number of counts in the pulser peak obtained in the spectra was compared to the number of events registered in the dual scaler and this relationship gave the dead time

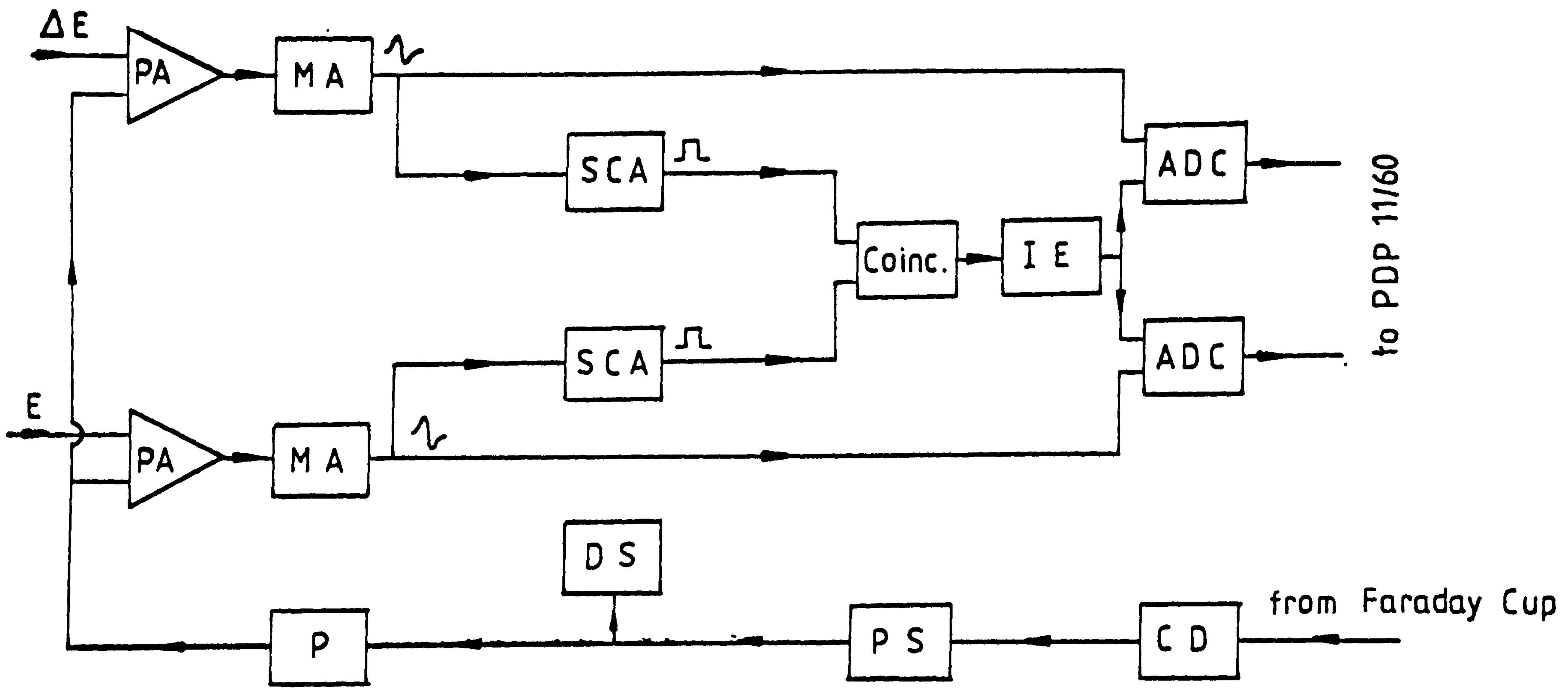

PA = preamplifier   MA = main amplifier   SCA = single channel analyzer

Coinc. = coincidence box   I E = interrupt encoder   CD = current digitizer

ADC = analog to digital converter   P = pulser   PS = prescaler   DS = dual scaler

Figure 2.4 Electronic arrangement for the angular distribution experiments.

correction. Data were recorded event by event on magnetic tape, and at the same time, on-line analysis was carried out. The set up of windows in the PI spectra allowed to observe different particle spectra during the experiment.

2.6.2 Experimental Cross Section and Errors

The differential cross section for a nuclear reaction in a gas target [BRA77] is similar to the expression for a thin solid target, and can be written as:

$$\frac{d\sigma(\Theta_{cm})}{d\Omega_{cm}} = 266.0 \frac{M_i\ C_s\ A_t}{Q_t\ I} \quad \text{(mb/sr)} \tag{2.16}$$

where:

M_i = number of detected particles,

C_s = charge state of beam

A_t = molecular weight in grammes divided by the number of interacting atoms per molecule,

Q_t = integrated beam current in units of 10^{-9} Coulombs (it is assumed that the loss of beam flux in the exit window and gas is negligible)

and

$$I = \int_D^A \rho\ \Delta\Omega_L(x) \frac{d\Omega_{cm}}{d\Omega_{lab}}\, dx \tag{2.17}$$

with

x = distance from the centre of the gas target along the beam direction (for the integration limits D and A see fig. 2.2)

ρ = density of the gas in $\mu g/cm^3$,

$\Delta\Omega_L(x)$ = laboratory solid angle substended by the detection system at point x in the gas (in sr),

and $\frac{d\Omega_{cm}}{d\Omega_L}$ is defined from the relationship between an angle Θ expressed

in the centre of mass and laboratory frames:

$$\Theta_{cm} = \Theta_L + \arcsin(\gamma \sin\Theta_L) \qquad (2.18)$$

where

$$\gamma = \left\{\frac{M_a M_b}{M_A M_B}/(1 + (1 + \frac{M_a}{M_A})\frac{Q}{E_i}\right\}^{\frac{1}{2}} \qquad (2.19)$$

for a reaction A(a,b)B, with Q-value Q and incident energy E_i.

The above mentioned integral "I" can be evaluated with the use of simple trigonometry making the following assumptions:

a) the detection collimation system is geometrically aligned with the gas target centre,

b) the thickness of the collimators are negligible,

c) the finite beam spot is also negligible,

d) $\frac{d\Omega_{cm}}{d\Omega_L}$ is independent of x and

e) ρ is constant throughout the gas.

As the gas is heated during the experiment by the energy loss of the beam in windows and gas, assumption (e) can be argued. In order to estimate this effect different runs with different beam currents have been performed and they showed agreement within 10-20%. With all these assumptions the calculation of "I" reduces to finding a expression for $\Delta\Omega_L(x)$ which will depend on the area of the detector seen from a point x within the segment AD. Two different expressions result [BRA77] since for points x within segments AD but outside segment BC and for points x within BC (see fig. 2.2) different collimator slits limit the "area" of the detector seen from x.

When calculating the experimental cross section statistical and systematic errors combine to give the final uncertainty. The total number of counts in each peak studied was obtained by a peak fitting routine which fits gaussian distributions with parabolic or linear backgrounds to the experimental data. As the number of counts (N) in each peak is supposed to follow a Poisson distribution in time, the statistical errors associated are proportional to the square root of N, to the contribution of the background counts and to contributions of nearby overlapping peaks. This statistical errors which are given by the fitting routine are the ones shown in this thesis work for the experimental cross sections. Actually, the Faraday cup read out and the number of monitor pulses introduce contributions to the statistical uncertainties. The systematical errors are less important, since they will affect only the absolute cross sections. They can arise from:

i) measurement of the collimator slit sizes and distances from the gas cell centre,

ii) uncertainties in the gas density and in its density distribution.

2.7 Angular Correlation Experiments

2.7.1 Experimental Set up and Electronics

For the detection of ejectiles coming from the initial transfer reaction a telescope ΔE-E detector assembly situated at 10° from the beam direction in the laboratory frame was employed. The ΔE counter consiting in a thin 200 μm solid state silicon surface barrier detector and the E counter a thick 4.1mm one. A typical gas target collimation system was used with tantalum collimators of 0.2 cm slit width and with front and back collimators positioned at 3.3 cm and 29.2 cm from the centre of the 3 cm radius gas target. The ΔE and E detectors, the α source for calibration, and the three detection collimators were mounted on the rotatory hanging arm described in section 1 of this chapter.

Decay particles from the recoil nucleus were detected with five single silicon surface barrier detectors. These detectors were spaced 15° from each other and on the opposite side of the chamber (with respect to the beam direction) to the telescope as shown in figs. 2.5 and 2.6. One set of data was taken with the first of these five detectors at 20° and a second set at 30° making a total of ten different data points for the angular correlations. The collimation system for the decay particles detection was very carefully selected in order to have each detector looking at the same active region defined by the telescope collimation system in the gas cell. This is shown in fig. 2.5 wherealso the limiting trajectories for the screening effect of the front collimators have been drawn. It was concluded that the best

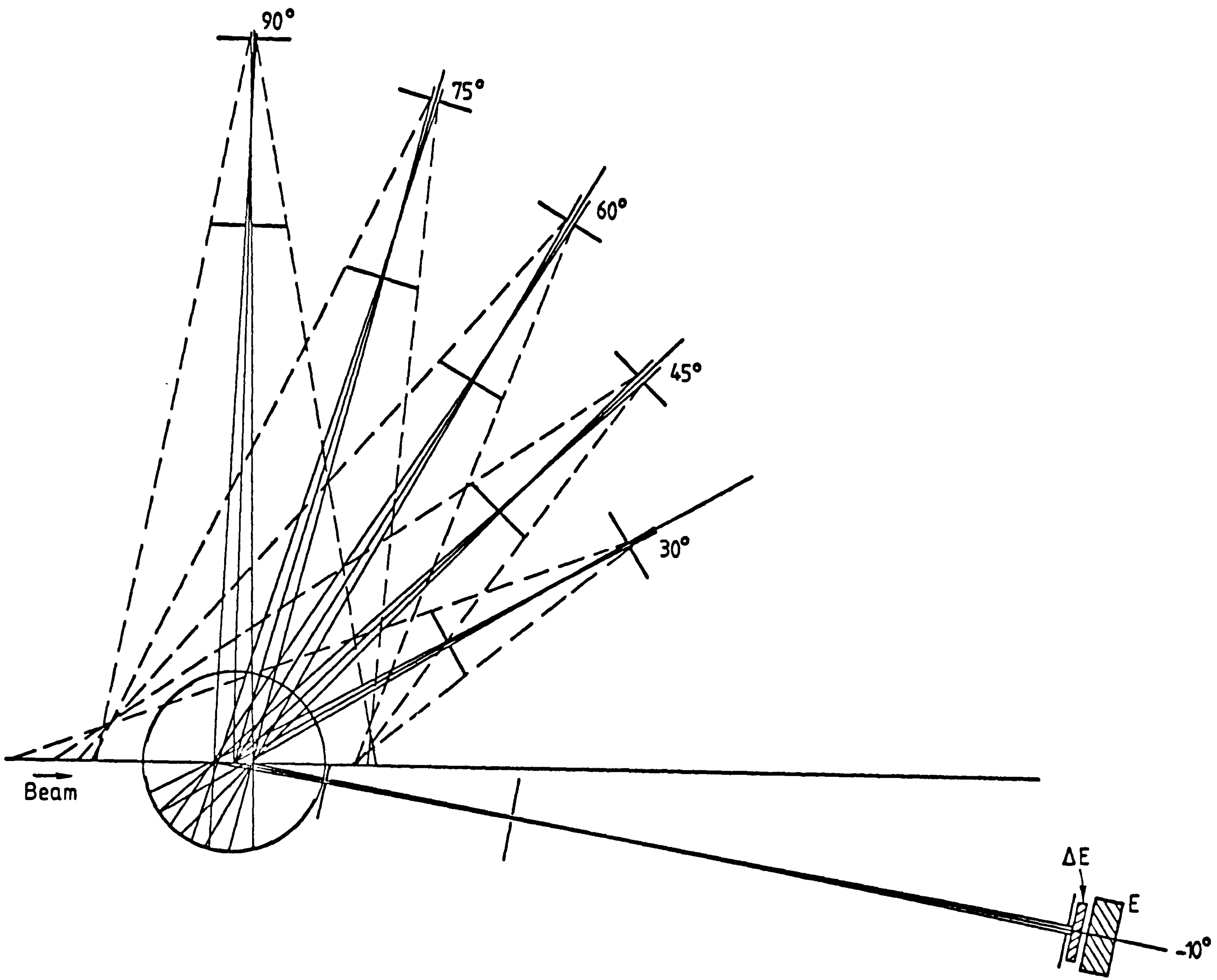

Figure 2.5 Extreme rays entering the side-detectors and ΔE-E and overlooking at the same active region in the gas cell. Extreme rays for the collimator shieldings are also shown.

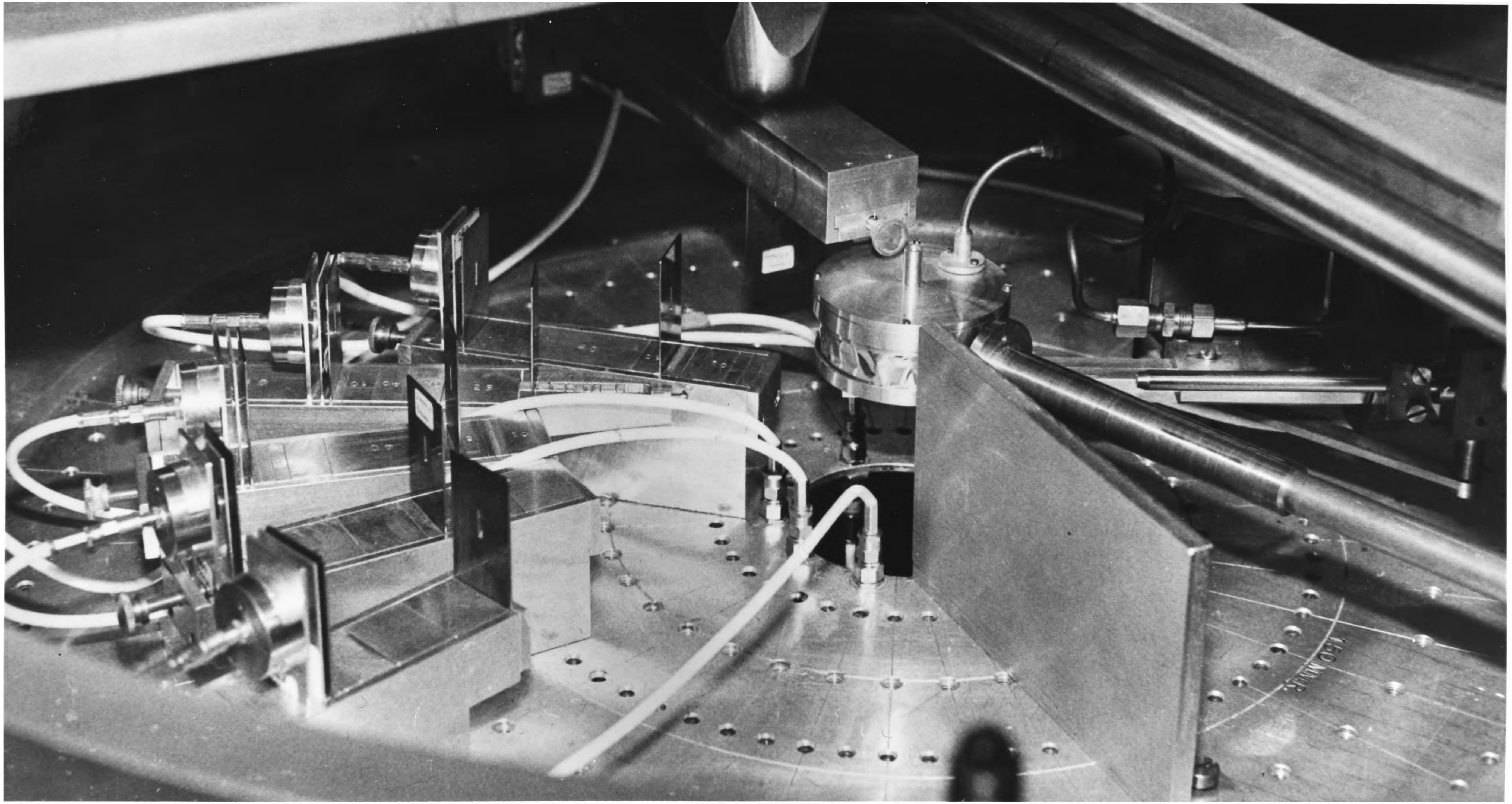

Figure 2.6 Experimental lay out

geometry is with the beam collimator as close as possible to the entrance gas cell window so as to have no scattered particles in the frame of the beam collimator entering one of the five detectors. It can also be seen that the scattering in the entrance and exit windows does not affect the detection of the decay particles. In figure 2.5 it is seen that the position of back and front collimators for each angle was chosen to be different. Table 2.2 shows the distances at which front and back collimators were placed at different detection angles in order to have the same region of the gas cell as actual target. The telescope was collimated with a 1 mm wide slit while the other detectors had a 2 mm wide slit. The front collimator of the telescope has a very narrow frame so as not to intercept the unscattered beam on its way to the Faraday cup. In order to increase the beam intensity gradual changes in the gas cell design had to be performed and finally 400-450 nAmps of ^{6}Li were used without burning the aluminium window's adhesive.

The electronic circuit employed for coincidence measurements is displayed in fig. 2.7. Fast Silena ADCs were used for the ΔE and E signals gated in prompt mode. The square pulses generated in the constant fraction discriminators by the timing signals from each detector were used for the slow part of the coincidences while the prompt pulses from the constant fraction discriminators were used for the fast coincidence circuit.

A standard slow coincidence box was used for the ΔE-E coincidence while for the signals from the five detectors a coincidence/or box was used. This box was employed to produce an output signal when there was a coincidence between the ΔE, E, time to amplitude converter (TAC)

Table 2.2

Collimation System for the Angular Correlation Experiment

Angle (degrees)	20	30	35	45	50	60	65	75	80	90
Distance front collimator (cm)	5.1	8.4	10.0	12.6	14.0	15.5	16.2	17.5	18.2	18.6
Distance back collimator (cm)	13.0	15.5	16.8	19.3	20.6	21.9	22.5	23.8	24.5	24.9
Angle acceptance (degrees)	2.90	3.22	3.36	3.42	3.48	3.58	3.64	3.64	3.64	3.64
X1 (cm)	3.62	3.64	3.66	3.65	3.66	3.66	3.66	3.67	3.68	3.68
X2 (cm)	2.28	2.29	2.28	2.30	2.29	2.31	2.31	2.31	2.31	2.31

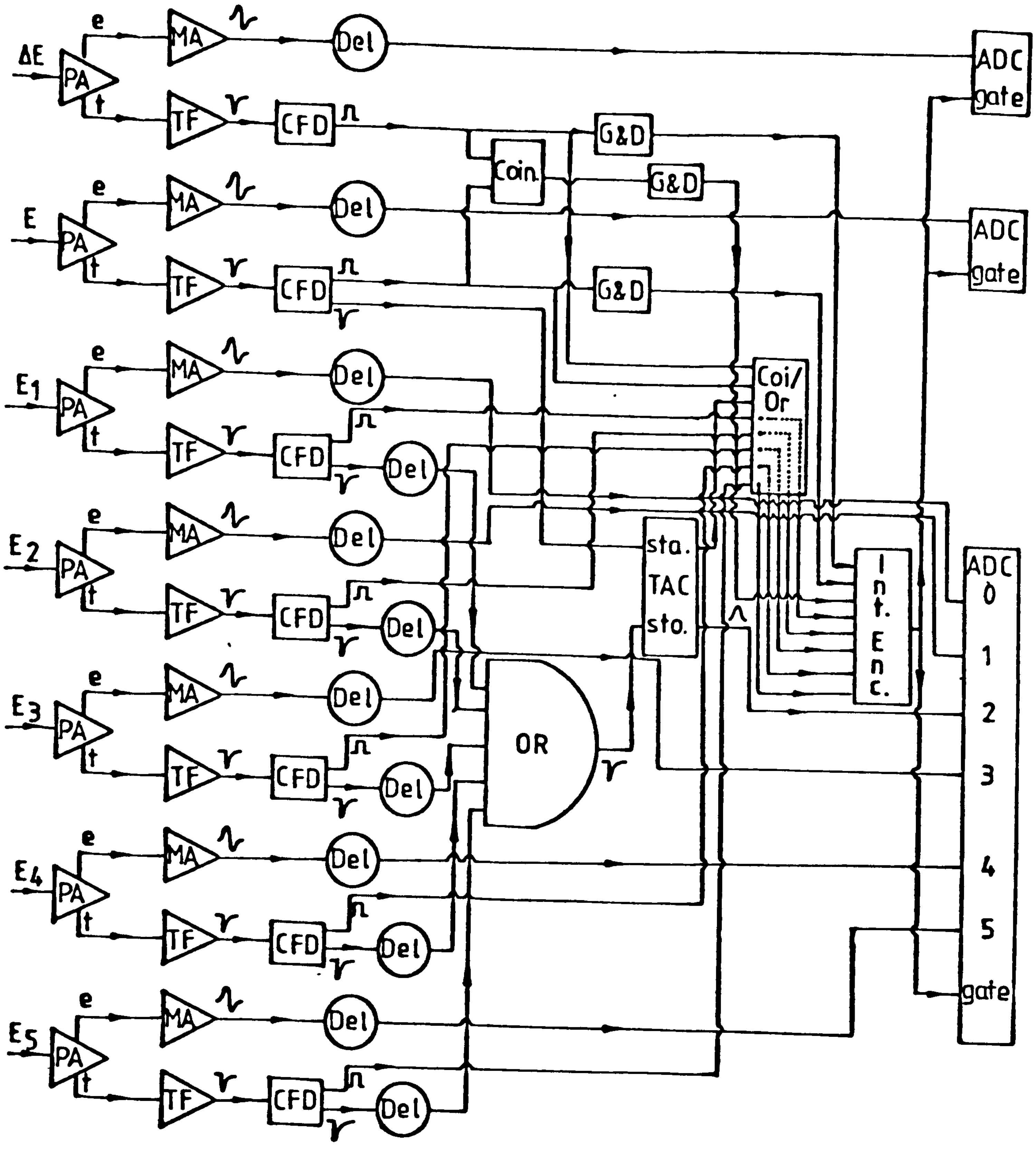

PA = preamplifier MA = main amplifier Coin. = coincidence box

CFD = constant fraction discriminator TF = timing filter amplifier

G&D = gate and delay generator ADC = analog to digital converter

TAC = time to amplitude converter Coi/Or = coincidence & or box

Int.Enc. = Interrupt encoder Del. = delay OR = fast or box

Figure 2.7 Electronic arrangement for the angular correlation experiment.

pulses and at least one signal from any of the five detectors. Only one TAC was used since a fast OR box generated the stop signal with any of the five (negative) input pulses. The box labelled interrupt encoder, developed in this laboratory, has eight different inputs. Each input socket has a priority according to its place, the uppermost having the lowest priority. When more than one input pulse reach the encoder, only the one with higher priority is processed. If singles events are not required, the corresponding two inputs in the interrupt encoder can be disabled, thus reducing the dead time and securing that only coincidence events are written onto magnetic tape. This CAMAC box transfers to the PDP11/60 computer the information on the particular detector (route) which generated the signal. Typically, short runs were performed in order to identify peaks of single events so as to set the relevant windows and then long runs with the requirement of telescope - detector coincidence events were carried out. Single event runs were also periodically performed as a check of a possible gain shift. The timing of the circuit was carried out before the runs with the aid of a precision pulser. TAC resolutions of ~ 3, 4 nsec were obtained with this procedure.

2.7.2 Data Collection and Reduction

The data were recorded on magnetic tape event by event for a later off line analysis and also sorted on line. Windows were set in the particle identification spectrum (obtained as explained with the signals from the telescope), TAC, router and particle spectra. These windows would then identify the particle, discard events which did not satisfy the TAC coincidence, identify the detector and the particular energy level of the recoil nucleus, respectively. As single counters were used for the residual nucleus decay detection, the corresponding particle identification was obtained from the kinematics. Some off line sorting was carried out with the energy level window set on different peaks so as to study all possible states populated in any particular recoil nucleus. Other sortings had a window off the TAC peak in order to study the random contributions.

The experimental cross sections were estimated with a similar expression as that used for the angular distributions assuming that the distance travelled by the recoil nucleus in the gas before particle decaying was negligible. Since the general theoretical expressions for the angular correlations are given in the centre of mass system of the recoil nucleus, the change to this new frame will now be introduced. Let us start by considering the kinematical relationships. Let V be the velocity of the recoil nucleus(in the laboratory system) before the break up, v and v_o the velocities of one of the resulting particles in the laboratory and centre of mass system, respectively, and Θ (Θ_o) the angle of emission in the laboratory (centre of mass) frame. The vector addition $\vec{v} = \vec{V} + \vec{v}_o$ is represented in fig. 2.8.

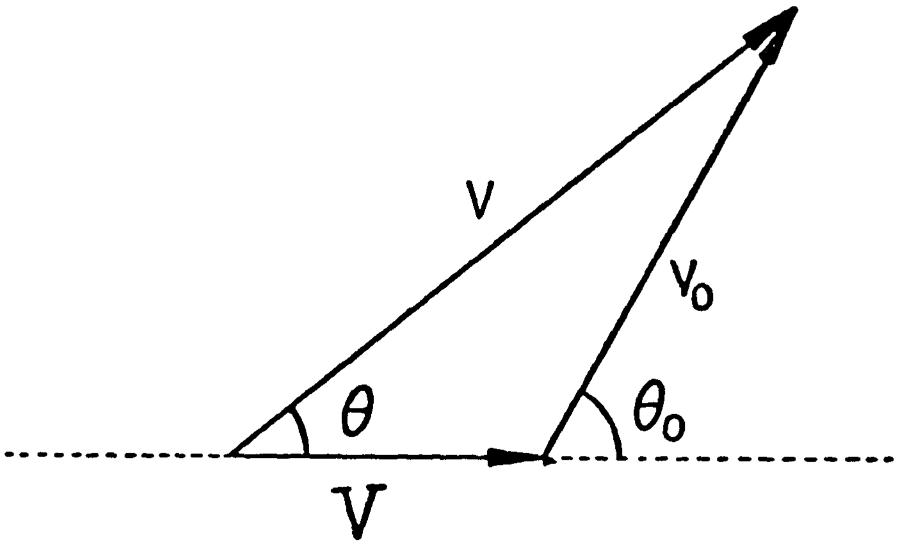

Figure 2.8 Vector addition diagram.

The relation between Θ and Θ_o is [LAN60]:

$$\cos\Theta_o = -\frac{V}{v_o}\sin^2\Theta + \cos\Theta\left((1-\frac{V^2}{v_o^2}\sin^2\Theta)^{\frac{1}{2}}\right) \qquad (2.20)$$

and therefore;

$$\frac{d\cos\Theta_o}{d\cos\Theta} = 2\frac{V}{v_o}\cos\Theta + (1-\frac{V^2}{v_o^2}\sin^2\Theta)^{\frac{1}{2}} + \frac{V^2\cos^2\Theta}{v_o^2\,(1-\frac{V^2}{v_o^2}\sin^2\Theta)^{\frac{1}{2}}} \qquad (2.21)$$

CHAPTER 3

States in ^{18}F: Angular Correlation Measurements

3.1 Introduction

Exploratory runs for alpha-transfer reaction with ^{6}Li incident ions on ^{14}N gas targets were performed at a bombarding energy of 36 MeV. They showed deuteron spectra of striking selectivity (fig 3.1) and strong population mainly between 5 and 15 MeV of excitation energy, following closely the pattern found by Cobern and Parker [COB77] in the $^{14}N(^{7}Li,t)^{18}F$ reaction. Some of the low lying levels observed here were seen by Rolfs et al. [ROL73] in their work on $^{14}N(\alpha,\gamma)^{18}F$, and identified as members of a $K^{\pi}=1^{+}$ 4p-2h rotational band. The cluster model [BUC77b] has suggested as well the existence of a $K^{\pi}=1^{+}$ band in ^{18}F based on $^{14}N + \alpha$ cluster configurations and predicted the excitation energies for some of its members. Tests could be performed on the ability of the cluster, shell and rotational models in predicting experimental results, if the higher spin states of this band were identified. The strong population of levels above 5 MeV, the fact that these states are unbound to α-decay and the knowledge that transfer reactions induced by heavy ions do not normally have angular distribution shapes strongly dependent on the spin of the final state, led us to study the possibility of spin determination by particle-particle (d-α) angular correlation measurements.

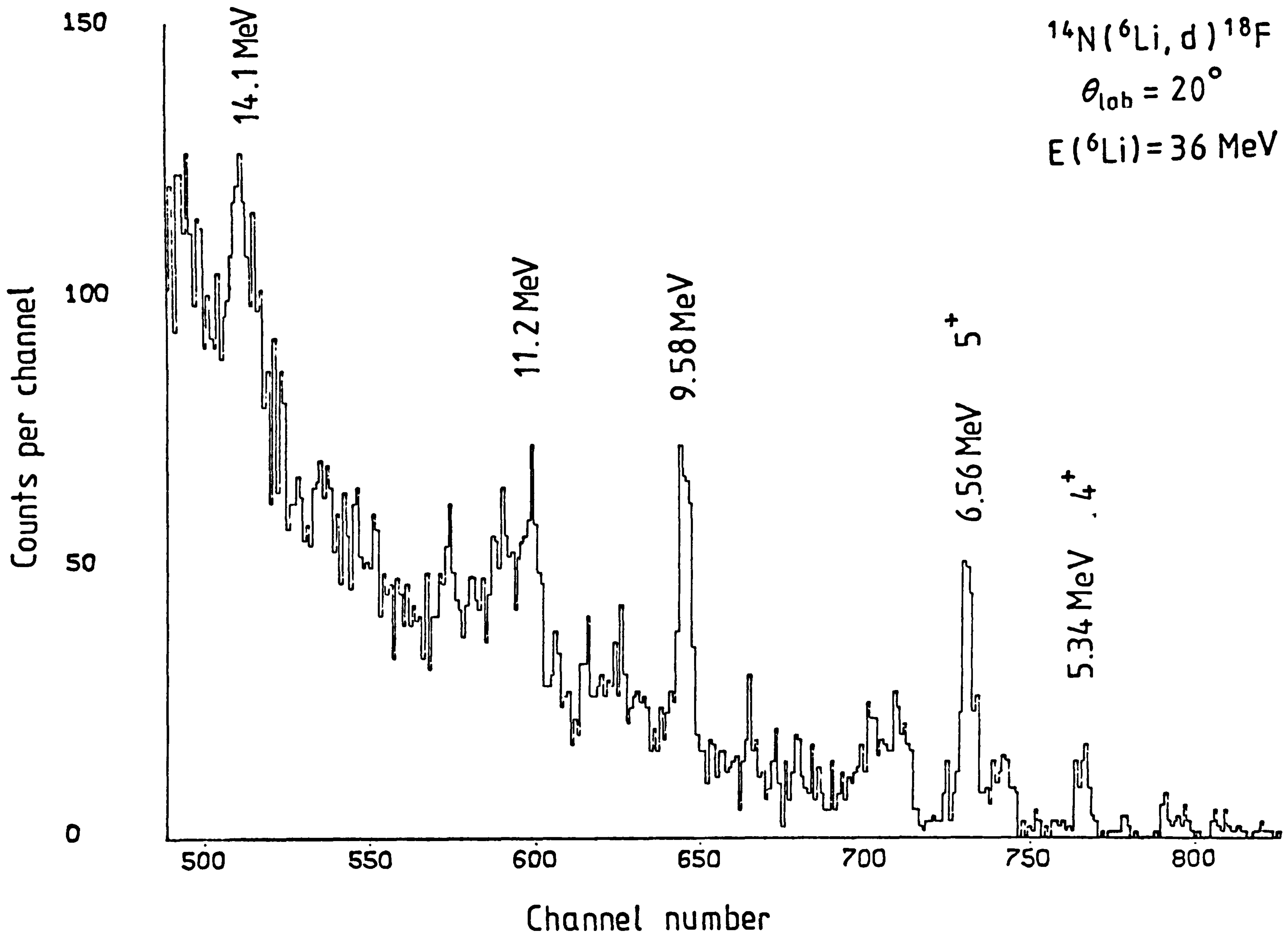

Figure 3.1 α-transfer spectrum on ^{14}N

Compound nucleus and direct α-transfer theoretical cross-sections were calculated and compared to the relevant experimental angular distributions, in an effort to decide on the reaction mechanism. Based on the measured cross sections it was found that the reaction proceeds through a direct α-cluster mode. The theoretical angular correlations for the alpha decay were calculated for all possible spins in the recoil nucleus considering that the main reaction mechanism involved was the direct α-transfer. This studies showed that, when the outgoing ejectile (deuteron) was detected at fairly forward angles, the population of states of natural parity gives characteristic ondulatory angular correlations allowing spin assignments. On the other hand, population of unnatural parity states gives rise to washed out angular correlation functions, making impossible the spin identification. Two out of the three unknown spin states observed in the α-transfer reaction showed strongly oscillating correlations, and subsequently, spin assignments were made.

3.2 Cluster State Description

It is well known that relatively few states of the final nucleus are populated in multiparticle transfer reactions induced by heavy ions. This selectivity is the result of the detailed structure of the final and initial states. Buck Dover and Vary [BUC75] have developed a simple potential model which decribes very successfully different properties of these states, such as energy levels, r.m.s. radii, decay widths, and transition probabilities. Fairly good agreement with the experimental data has been found for ^4He, ^3He, and ^3H cluster description of states in ^{19}F, ^{19}Ne, ^{20}Ne, ^{16}O, ^{18}O, and ^{18}F.

A clear advantage of a model in which the cluster is regarded as a single particle orbiting around a core (only mass, charge and spin of the cluster are considered) is that a small set of states of a particularly simple structure will replace the large basis of a shell-model description. The cluster states can be described then in terms of bound states and single particle resonances, solutions of a single particle potential

$$V(r) = V_o\ f(r) + V_{so}(r) + V_{coul}(r) \tag{3.1}$$

where the central cluster-core potential $V_o\ f(r)$ is obtained by folding the cluster and core mass densities (ρ_C, ρ_A):

$$f(r) = -\frac{2\pi\hbar^2}{\mu} \int d\vec{r}'\ \rho_A(\vec{r}-\vec{r}')\ \rho_c(\vec{r}') \tag{3.2}$$

and μ is the reduced mass. The coulomb potential V_{coul} corresponds to a spherical charge distribution with radius R_c:

$$R_c = r_{oc}(A_A^{1/3}+A_c^{1/3}) \tag{3.3}$$

and the derivative spin-orbit term $V_{so}(r)$ is introduced by the authors for triton and ^{3}He cluster states:

$$V_{so}(r) =- V_{so} \left(\frac{\hbar^2}{m_\pi^2 c^2}\right) \frac{1}{r}\left|\frac{df(r)}{dr}\right| \vec{l}.\vec{\sigma} \tag{3.4}$$

Buck and Pilt suggested lately an alternative parametrization of the nuclear cluster-core potential which gives a very similar shape to that obtained with the folding model and with the advantage of being very convenient for numerical calculation:

$$f(r) = \frac{1 + \cosh(R/a)}{\cosh(r/a) + \cosh(R/a)} \tag{3.5}$$

often called Symmetrized Woods-Saxon potential. There is a feature that clearly adds an advantage to the use of the folded potential over the common Woods-Saxon shape. It has been shown that the folded potential gives rise to L-states of energy spacing very close to those of a rotational (L(L+1)) band [ROW77, BUC77a]. The symmetrized Woods-Saxon potential can then generate a wide variety of spectra with the use of small to large diffuseness parameter values; from mainly degenerate L-states, to rotational bands characteristic of pure Gaussian shapes (as found by Buck and Tomusiak [BUC74]).

In order to include the most obvious requirements of the Pauli principle to the model, we have to consider the structureless cluster in its relative motion around the core; the cluster is viewed as a single particle in an orbit characterized by a certain number of nodes N and an angular momentum L. These N and L values are related to the individual quantum numbers n_i and l_i of the nucleons which conform the cluster, by the relation:

$$2\,N + L = \sum_{i}^{\nu} (2\times n_i + l_i) \qquad (3.6)$$

(where ν is the total number of nucleons in the cluster). Then, in a manner compatible with the simple shell-model, the Pauli exclusion principle which requires the nucleons to fill single particle levels different from those occupied by the core nucleons, is included. The n_i and l_i values are chosen so as not to have two particles in the same state.

3.3 The $^{14}N(^{6}Li,d)^{18}F$ α-Transfer Reaction

In order to have a direct α-transfer mechanism, we expect for both, the light and heavy systems to have a fairly high degree of alpha clustering in their structure.

Cobern and Parker [COB77] studied the $^{14}N(^{7}Li,t)^{18}F$ α-transfer reaction at 36 MeV of ^{7}Li and found a striking selectivity for members of the $K^{\pi}=1^{+}$ band of predominantly 4p-2h description. The 1^{+}, 2^{+}, 3^{+}, 4^{+}, and 5^{+} already identified members of the $K^{\pi}=1^{+}$ rotational band (Rolfs et al.[ROL73]) were observed, and two other states of strong population and unknown spin and parity were formed at 9.58 and 11.22 MeV, which made them think of higher members of the above mentioned band. The reaction $^{14}N(^{6}Li,d)^{18}F$ performed at 36 MeV of ^{6}Li gave a pattern very similar to that found by Cobern and Parker. This suggested that the selectively populated states also found in our $(^{6}Li,d)$ reaction were mainly of a 4p-2h description, which can be translated into characteristic N and L values. In the case of having the four particles transferred to the sd-shell, $2N + L = \sum_{i}^{4}(2 \times n_i + l_i) = 8$, therefore only even values of L are allowed. In order to cover a wider range of possibilities, states arising from the transfer of three particles to the sd-shell and one to the p-shell, as well as three particles to the sd-shell and one to the fp-shell were considered, giving $2N + L = 7$ and 9 respectively (only odd values of L would be allowed). The possible spins, parities, N and L values for each of the three 2 N + L bands included are shown in table 3.1.

Table 3.1

Four Particle Cluster States in ^{18}F

	$J^\pi(^{18}F)$	N	L	J
$2N+L = 7 \equiv ((sd)^3\ p)$				
	0^-	3	1	1
	1^-	3	1	1
	2^-	3	1	1
		2	3	3
	3^-	2	3	3
	4^-	2	3	3
		1	5	5
	5^-	1	5	5
	6^-	1	5	5
		0	7	7
	7^-	0	7	7
	8^-	0	7	7
$2N+L = 8 \equiv (sd)^4$				
	0^+	4	0	0
	1^+	4	0	0
		3	2	2
	2^+	3	2	2
	3^+	3	2	2
		2	4	4
	4^+	2	4	4
	5^+	2	4	4
		1	6	6
	6^+	1	6	6
	7^+	1	6	6
		0	8	8
	8^+	0	8	8
	9^+	0	8	8

Table 3.1

(cont.)

$2N+L = 9 \equiv ((sd)^3\, fp)$

$J^\pi(^{18}F)$	N	L	J
0^-	4	1	1
1^-	4	1	1
2^-	4	1	1
	3	3	3
3^-	3	3	3
4^-	3	3	3
	2	5	5
5^-	2	5	5
6^-	2	5	5
	1	7	7
7^-	1	7	7
8^-	1	7	7
	0	9	9
9^-	0	9	9
10^-	0	9	9

In order to obtain a good theoretical prediction for the angular particle-particle correlation, it is necessary to know the magnetic substate populations in the residual nucleus (Appendix A). The m-populations will depend on the reaction mechanism involved in the transfer process to the residual state, and for that reason, experimental angular distributions were measured and theoretically calculated for the spins of interest within the framework of direct and Hauser and Feshbach formalisms. Obviously, apart from the direct α-transfer, the other contribution which should be taken into account (as studied for (^{6}Li,d) reactions in neighbouring nuclei and at somewhat lower incident energies [MEI68, DaS76]) is the compound nucleus mode.

^{6}Li + ^{14}N elastic scattering was measured at several different angles. Other optical potentials as well as level density parameters for the Hauser Feshbach and DWBA calculations were obtained from references (see Chapter 4). The results obtained for the already known members of the $K^\pi=1^+$ band, as well as for the unknown spin states showed a compound nucleus contribution of less than 10% for all cases. The attention was focused then to the direct process, and computational programs were developed in order to read the transition amplitudes from DWBA codes, to calculate the theoretical angular correlation functions and to evaluate the displacement of the angular correlation symmetry axis. The three unknown spin states at 9.58, 11.2 and 14.1 MeV were studied for all the possible relevant values of spin and parity given in Table 3.1. For some spin assumptions, the theoretical predictions were structureless, while for some others a very strong oscillatory behaviour characteristic of the spin of the recoil nucleus was found. For many of these oscillatory cases, the strong structure vanished as the angle of the detected ejectile increased. This effect gave a limit for the detection angle of the ejectile, in order to have an oscillatory α-angular correlation function which would enable us to make spin assignments.

3.4 The $^{18}F \rightarrow {}^{14}N+\alpha$ decay.

All states in ^{18}F at excitation energies above 4.4159 MeV are alpha unbound. It has been shown [BRA77] that simplified prescriptions for describing those unbound states are not satisfactory for use in DWBA calculations; hence the wave functions for the ^{18}F levels have been represented by Gamow states. Within this formalism, the unbound states are treated as spectroscopically equivalent to bound states (Appendix C). The code "GAMOV" has been used to calculate these wave functions.

The possible orbital angular momenta of the alpha cluster with respect to the core are given by the triangular rule:

$$|I' - I''| \leq L_\alpha \leq I' + I'' \qquad (3.7)$$

where I' stands for the initial spin of the decaying nucleus and I" is the spin of the daughter nucleus formed in the α-decay. When the parity of parent and final states are the same, only even values of L_α are permitted. On the other hand, when the above mentioned parities are opposite, only odd values of L_α are allowed. In the cases studied in this chapter, only the decays to the ground state of the daughter nucleus are considered, since these correspond to the peaks strongly populated in the decay spectra.

Applying the selection rules for the alpha decay of excited states in ^{18}F to the ground state of ^{14}N ($J^\pi=1^+$, T=0) it can be seen that the possible L_α orbital angular momenta allowed for all ^{18}F spins taken into account in 2N+L= 7, 8,and 9 configurations are the ones shown in Table 3.1.

The following step for the α-angular correlation study, will be then to compare the experimental values obtained for the different states with the theoretical ones given by formula A.1.7 of Appendix A. The first noticeable difficulty for this α-decay analysis is that for several final spin values, two possible orbital angular momenta are allowed, and therefore, the spectroscopic coefficients $A_{\ell sj}$ and the decay matrices $S^{I'}_{s'',L_\alpha}$ have to be known in order to perform the theoretical calculation. When parentage amplitudes were available from shell model calculations, these were used in obtaining the spectroscopic coefficients $A_{\ell sj}$. For the rest, a study on the variation of the resultant angular correlation for different relative values of the spectroscopic factors was performed. At the same time, the influence of using different decay $S^{I'}_{s'',L_\alpha}$ matrices in expression (A.1.7) was investigated (as explained in Appendix A part 3) for different matrix value combinations in $|S^{I'}_{s'',L_{\alpha 1}}|^2 + |S^{I'}_{s'',L_{\alpha 2}}|^2=1$ and phases determined by $e^{i\phi}$ with $\phi=0$, $\pi/2$, π and $3\pi/2$. The theoretical angular correlations obtained for the different sets of values $A_{\ell sj}$ and $S^{I'}_{s'',L_\alpha}$ were compared to experimental ones with a χ^2 test in order to find the best fit.

Figure 3.2 shows a typical analysis for fixed spectroscopic amplitudes and different combinations of the decay $S^{I'}_{s'',L_\alpha}$ matrices with an assumed $J^\pi=8^-$ for the 14.1 MeV state in ^{18}F. For every combination of $A_{\ell sj}$ values, a χ^2 plot like the one mentioned was obtained and the minimum value resultant from these systematic analyses was used in the final chi-square comparison for spin assignment. When spin and parity

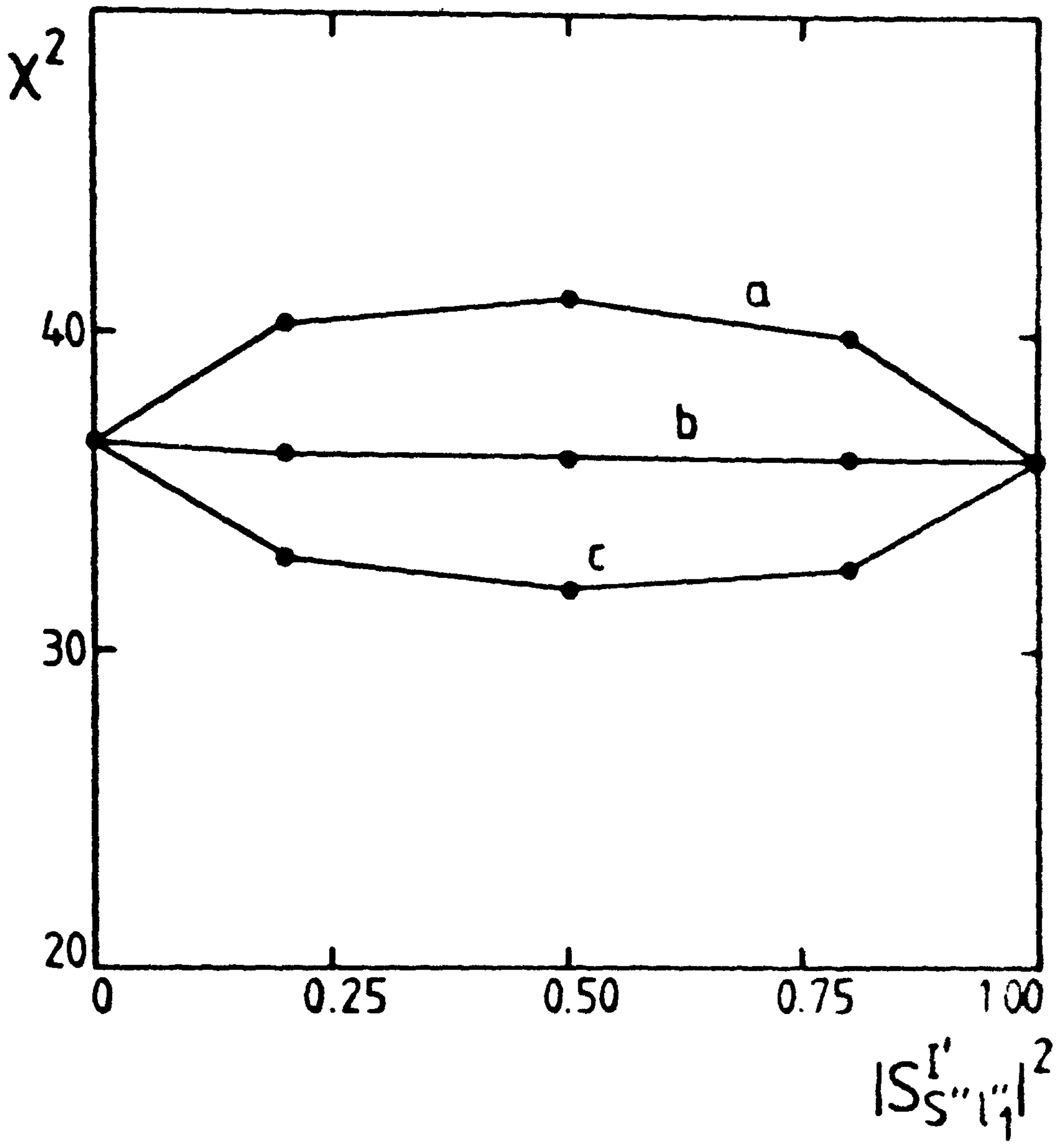

a) $\Phi_1 = 0,\ \Phi_2 = \pi\ ;\ \Phi_1 = \pi,\ \Phi_2 = 0$

b) $\begin{cases} \Phi_1 = \pi/2 \text{ or } 3\pi/2,\ \Phi_2 = 0 \text{ or } \pi \\ \Phi_1 = 0 \text{ or } \pi,\ \Phi_2 = \pi/2 \text{ or } 3\pi/2 \end{cases}$

c) $\Phi_1 = \Phi_2 = 0 \text{ or } \pi$

Figure 3.2 χ^2 comparison between the experimental angular correlation for the 14.1MeV state in ^{18}F and the theoretical estimation for a supposed 8^-. Different combinations of $S^{I'}_{s''l''}$ values have been considered. The solid lines join points for which a similar phase convention has been adopted.

assumptions allowed only one L_α contribution, the analysis was simpler since only one $A_{\ell sj}$ and $S^{I'}_{s'',L_\alpha}$ value intervenes in the theoretical expression for the angular correlation, and both can be taken as constant multiplicative factors which will not affect the angular correlation shape. For all the states with two L_α, the minima of the chi-square values have been used. Each minimum is obtained by calculating the χ^2 value for different combinations of the two S-matrices.

Another feature that has to be considered when comparing theoretical and experimental angular correlations, is the well known displacement of the symmetry axis when detecting the outgoing ejectile (deuteron in our case) at a laboratory angle away from 0 or 180 degrees. In general, reactions of the type $A(a,b)B^* \rightarrow C(c)$ (where B is formed in a state of well defined spin and parity) a symmetry axis for the sequential decay of B is exhibited [LAM71, ART71, LAN72, EIC73, PAN74, AVR75 and ART76]. When calculating a stripping process where the asymptotic interactions in the inital and final channels are neglected (as it is done in the Plane Wave Born Approximation) the direction of the linear momentum transfer, which equals the recoil direction of the residual nucleus, is the symmetry axis for the decay pattern. Distortion of the plane waves in the incident and exit channels has been extensively studied by Satchler [SAT60] and shows the effect of rotating the symmetry axis for the decay away from the recoil direction, and sometimes of even destroying this symmetry.

The advantage of alpha transfer using a ^{6}Li beam is that due to the very weak coupling between the deuteron and the α-particle in this projectile (1.4735 MeV), during the process it is assumed that the deuteron acts as an observer, reducing the problem to that of having a beam of alpha particles impinging on the target along the linear momentum transfer direction.

3.5 The Experiment.

The reaction $^{14}N(^{6}Li,d)^{18}F \rightarrow {}^{14}N(\alpha)$ was studied with a 36 MeV ^{6}Li beam from the Folded Tandem accelerator at Oxford. The target, ^{14}N 99.5% purity was contained in a thin window gas cell of 3 cm radius (see Chapter 2). The deuterons were registered by a (ΔE-E) counter 'telescope' consisting of a thin (200 μm) and a thick (4.1 mm) silicon detectors. The telescope was placed at 10° to the beam direction. For the decay alpha particles, five silicon detectors with thickness ranging between 1500 μm to 2000 μm were used, placed 15° apart from each other. Ten data points were obtained at laboratory angles between 20 and 90 degrees. For each of the final measurements, three day runs at approximately 400 nAmps. of ^{6}Li beam were performed.

According to the electronic circuit described in Chapter 2, coincidences between signals from the deuteron telescope and signals from each of the α-particle counters were recorded. The α-collimation system was arranged in order to look at the same active region of the gas cell as the telescope collimation system was subtending. Thus collimation distances from the gas cell centre were different for each α-detector and carefully considered in further calculations for the number of coincidence counts per sterradian. ^{18}F states analysed in coincidence with decay particles had typical total cross sections of 2-6 microbarns. Ten different data points were obtained for each angular correlation.

Though ^{18}F states with excitation energy above 4.4159 MeV are α-unstable, only those with excitation energy higher than ~ 7 MeV can be studied under our experimental conditions. The alpha particles have to be ejected with high enough energies as to pass the 5 μm thick aluminium windows and yet, at laboratory angles of 60 to 90 degrees, have residual energies on entering the detector sufficiently above noise level. According to this limitation, the first excited state in ^{18}F which can be studied with this particle - particle angular correlation method is (fig 3.1) the one at 9.58 MeV. Typical kinematics for an alpha particle decaying from fictitious 7 to 9 MeV states in ^{18}F to ^{14}N ground state, after the ejected deuteron has been measured at 10° and under the experimental conditions given above, are shown in fig 3.3.

^{18}F excited states above 5.606 and 7.526 MeV are unstable under proton and deuteron emission respectively. For that reason, the proton and deuteron kinematics were also studied and their expected energies identified in the different decay spectra. For the alpha decay of ^{18}F, kinematical behaviour of the emitted ^{4}He was studied for the cases in which the residual nucleus ^{14}N was left either in its ground state ($J^{\pi}=1^{+}$, T=0) or in its second excited state ($J^{\pi}=1^{+}$, T=0, 3.9478 MeV) omitting the isospin forbidden α-decay to the 2.3129 MeV first excited state in ^{14}N ($J^{\pi}=0^{+}$, T=1). For the proton emission of ^{18}F, decays to the ground state of ^{17}O ($5/2^{+}$) and to its first two excited states ($1/2^{+}$ at 0.8708 MeV and $1/2^{-}$ at 3.0552 MeV) were kinematically followed, and for the deuteron emission, only the decay to the ^{16}O ground state was theoretically analysed since its high lying first excited state (6.049 MeV) was already too high in excitation energy for allowing ^{18}F

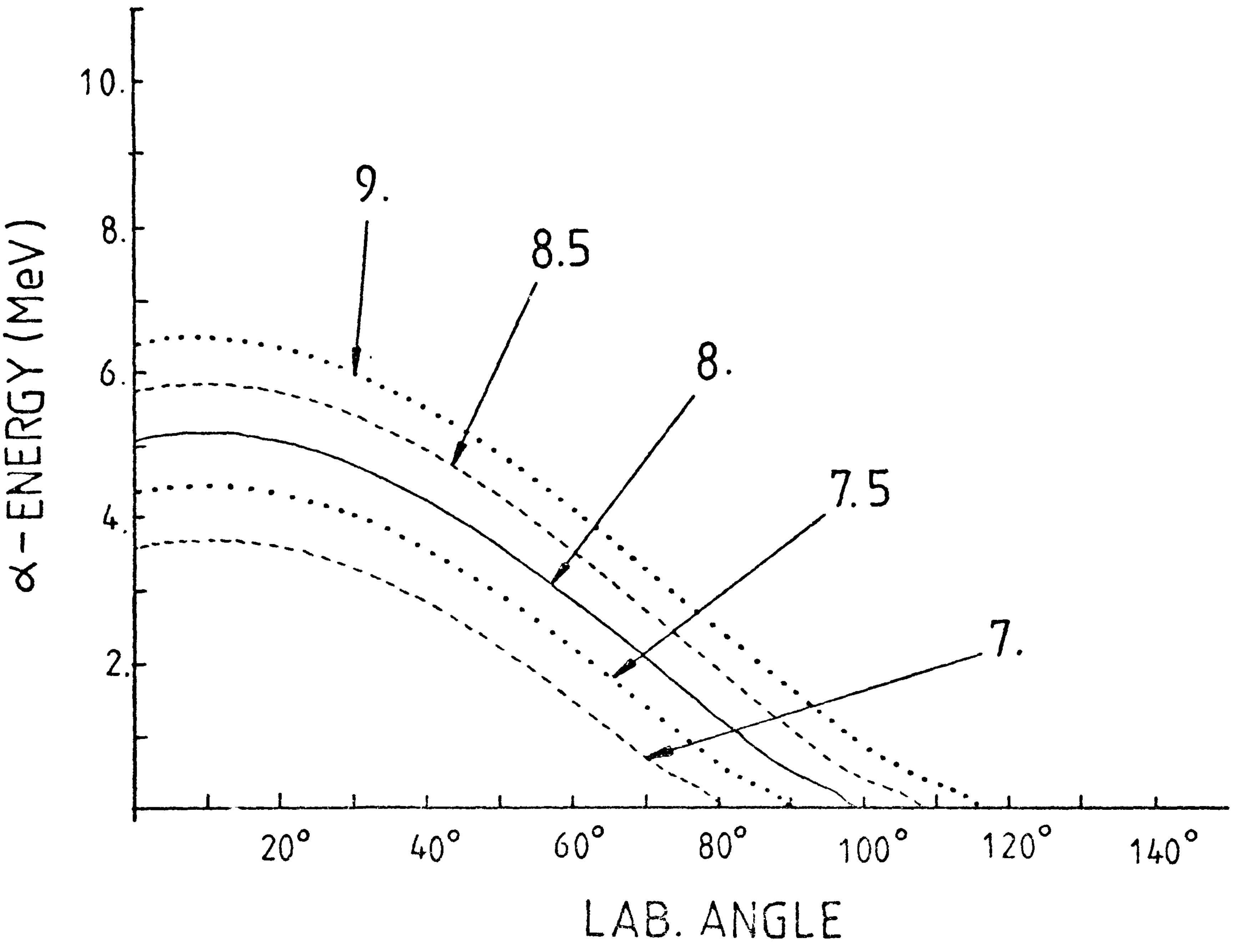

Figure 3.3 α-decay kinematics from fictitious 7MeV to 9MeV states in ^{18}F, when the deuteron from the $^{14}N(^{6}Li,d)^{18}F^{*}$ is detected at 10° in the laboratory system.

deuteron emission.

As a typical example the kinematical behaviour of alpha particles, protons and deuterons resulting from the decay of the 11.2 MeV state in ^{18}F is given in figure 3.4. It can be seen that from 0° to approximately 70° in the laboratory system the alpha emission to the ground state of ^{14}N gives the higher energies, and then, no interference with any other decay is observed. Within the angular range of detection, deuteron and proton emissions are separated by at least 500 KeV, allowing good identification in the decay spectra. For the three high excited states in ^{18}F, the coincidence spectra showed a very strong alpha emission leading to the ground state of ^{14}N, and a light contribution of deuteron and proton decay leading also to zero excitation energy on their correspondent residual nuclei. No particle emission for excited states of the daughter nuclei was observed in any of the decay spectra at the detector positions described in Chapter 2. The kinematical crossings of alpha particles and protons for the three ^{18}F states (9.58, 11.2 and 14.1 MeV) lay at approximately 70 degrees, and this value determined the angular separation for the detectors to be positioned in this region. A typical decay spectrum at 45° laboratory angle recorded for coincidences with the state at 11.2 MeV in ^{18}F is shown in figure 3.5.

Percentages of the different decays are given for each of the analysed states, as a result of integrating the number of coincidence counts/str. for the ten different angles. As can be seen in figure 3.1, there is a large continuous background at higher excitation. This is a very typical feature of the ^{6}Li spectra. It is commonly assumed

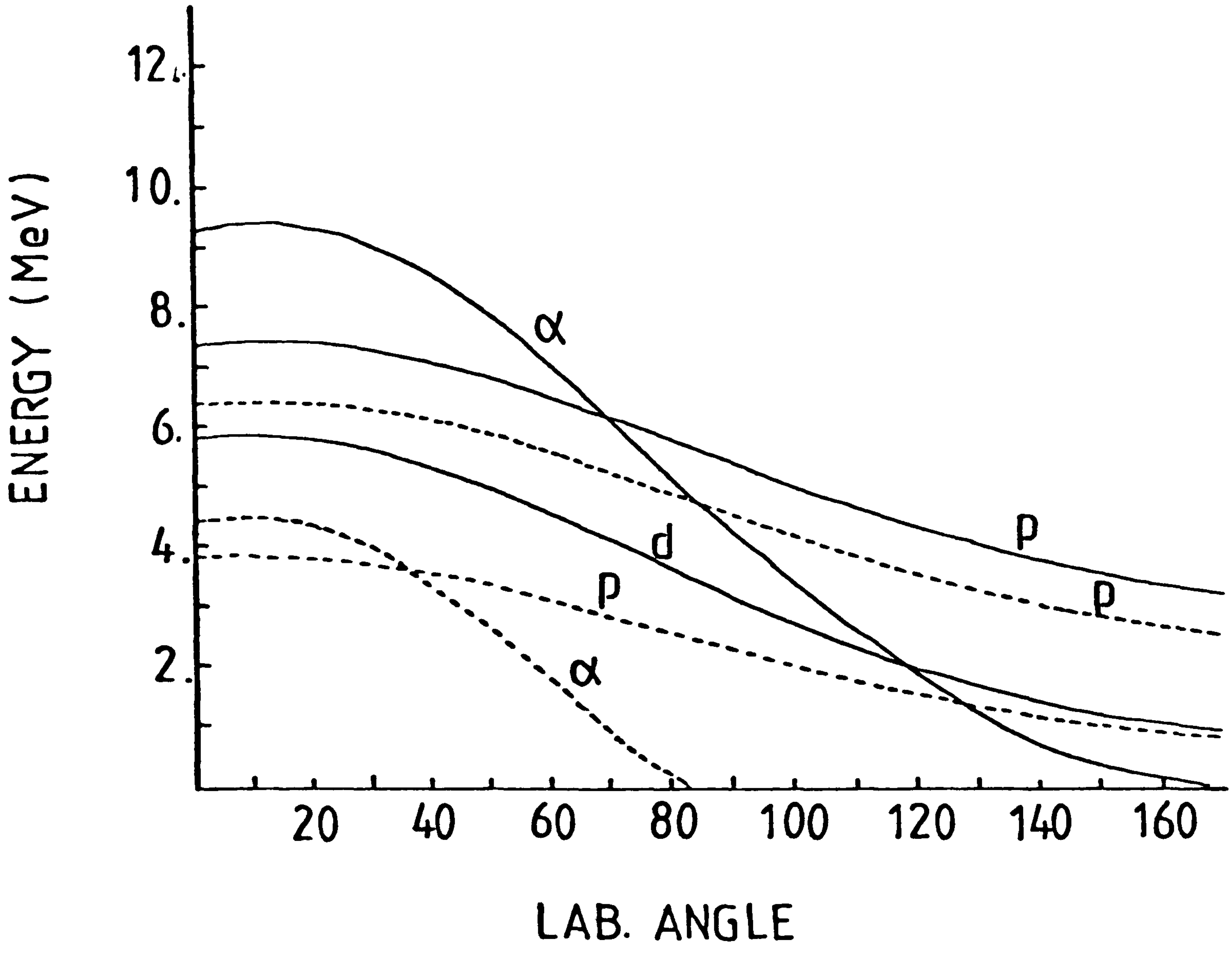

Figure 3.4 Kinematics for different decay particles from the 11.2MeV state in ^{18}F. Decays to the ground state of the daughter nucleus are plotted with solid lines, while decays leading to excited states are shown in dashed lines.

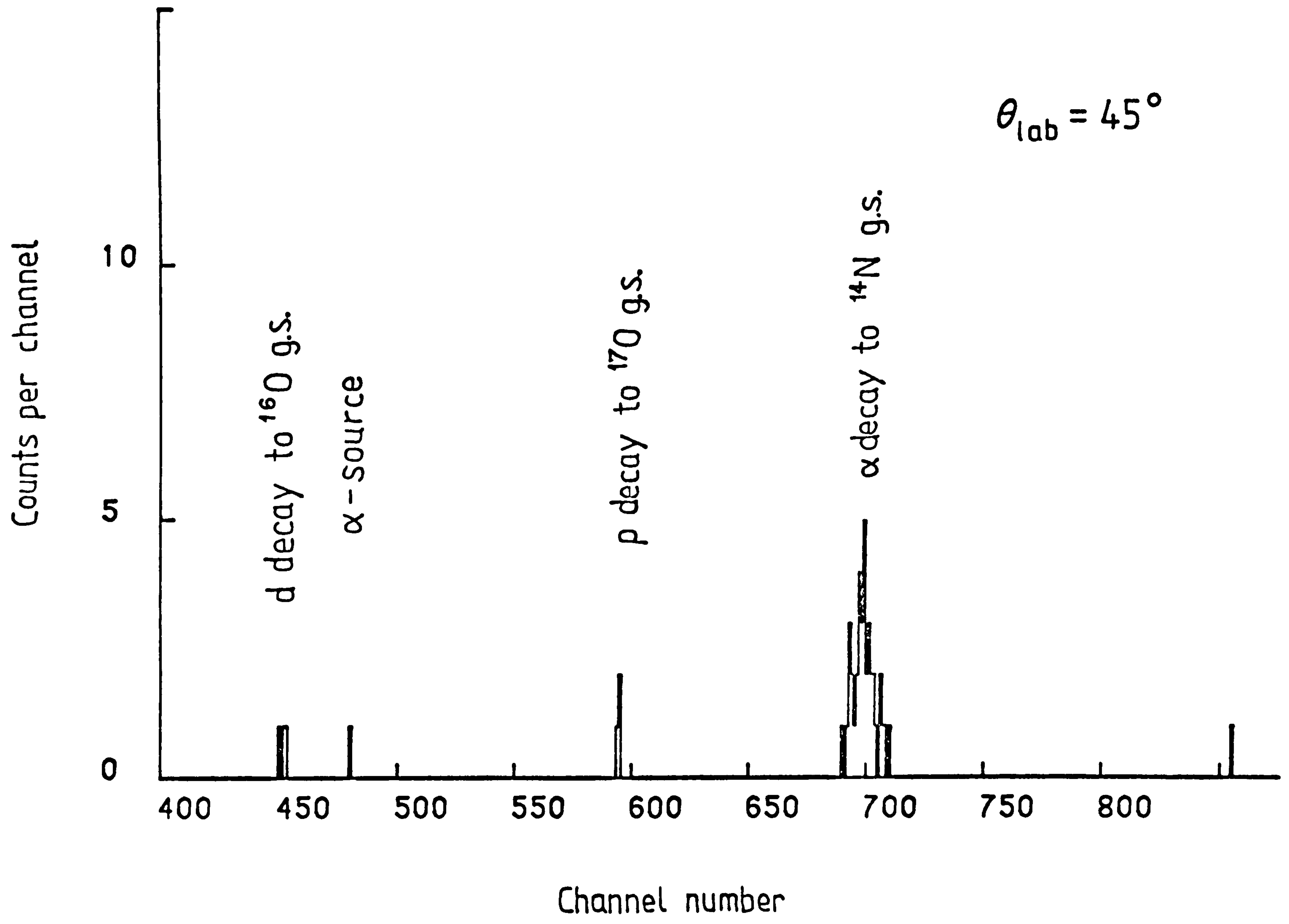

Figure 3.5 Decay spectrum for the 11.2MeV state in ^{18}F

that this background is the result of the break-up of the lithium in the Coulomb field of the target nucleus. It is important then to consider the contribution of that background to the coincidence spectra and to study whether real break-up (d-α) coincidences could add to the total number of counts for any of the decay detectors, jeopardizing the reliability of the experimental angular correlation data for certain angles of measurement. In ^{6}Li ground state, the deuteron and the alpha particle are bound by 1.4735 MeV, from its first excited state (3^+ at 2.185 MeV) onwards, ^{6}Li is then deuteron and alpha unstable. Using this first excited state (Γ=26 KeV) for the kinematical analysis of the break-up under a simple picture, the ^{6}Li nucleus will travel for at most an average distance of 8.2 10^{-10} mm before decaying. This will give no alteration to the trajectories in the collimation system, thus in calculating the reaction kinematics we can safely ignore the distance travelled by the ^{6}Li before its decay.

In the laboratory system, for a definite angle of ^{6}Li emission, the alpha and deuteron dissociations will constrain their movements within a cone whose axis will lay along the ^{6}Li direction of motion, and whose maximum apex angle will be different for deuterons and alpha particles and given by:

$$\Theta_{max}(d) = 2 \sin^{-1}\left(\left(\frac{Q_{eff}\, m_\alpha}{E(^6Li^*)\, m_d}\right)^{\frac{1}{2}}\right)$$

$$\Theta_{max}(\alpha) = 2 \sin^{-1}\left(\left(\frac{Q_{eff}\, m_d}{E(^6Li^*)\, m_\alpha}\right)^{\frac{1}{2}}\right) \tag{3.8}$$

where Q_{eff} =-1.4735 MeV + 2.185 MeV = 0.7115 MeV, and due to the mass factors, the limit angle for the alphas will be smaller than the one for the deuterons. For deuterons detected at a fixed angle, there will be a range of ^{6}Li directions of motion within limit angles, which may contribute to that deuteron angle of detection. Subsequently, the angle range for the dissociated alpha particles can be obtained. Figure 3.6 shows the limit angles in the reaction plane for the α-emission from ^{6}Li break-up, in comparison with the experimental lay out. The ^{6}Li limit angles are shown as well, and as can be noticed, there is no symmetry around the deuteron detection direction for the ^{6}Li and alpha extreme angles, since for larger angles of the ^{6}Li ejectile the kinematical behaviour will give smaller E(^{6}Li*) energies and this value will affect the angle estimation. It can be seen that for the 10° deuteron detection, the limit α-particle break-up angle in the laboratory system (7.8°) is substantially smaller than the one chosen for the first decay detector (20°), eliminating then the possibility of including break-up coincidences for any of the decay detector positions. Carefull analyses of coincidences setting windows on the background around the peaks of interest were carried out, giving no significant contribution, which

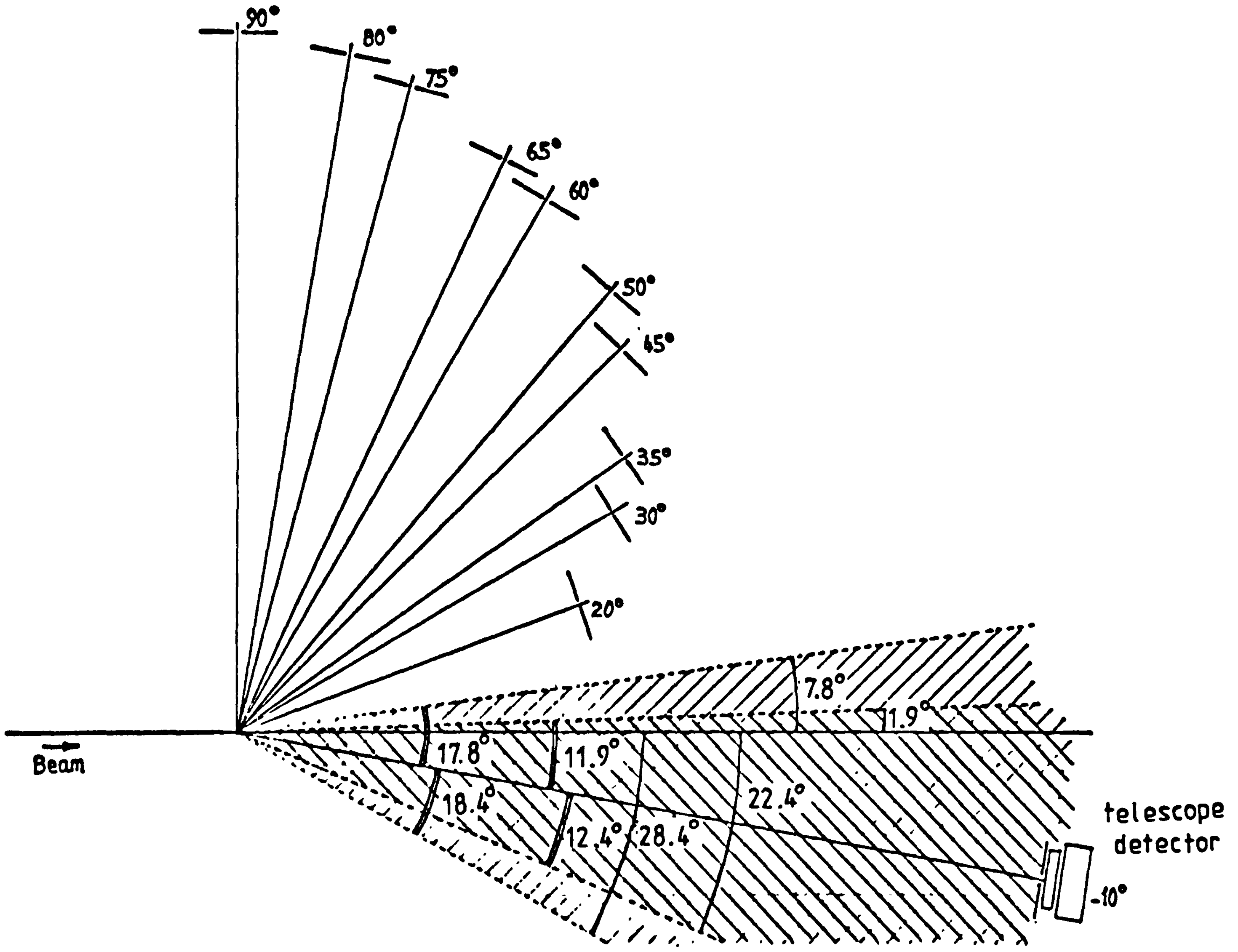

Figure 3.6 ^{6}Li break-up kinematics.

▨ α-particle angular range for deuterons detected at 10°.

▧ Angular range of ^{6}Li from which the detection of a deuteron at 10° is possible.

consisted in very few counts scattered homogeneously along the spectra and some counts from fictitious coincidences with the calibration source α-particles. Fig 3.7 shows a comparison between coincidence and single spectra for the deuterons, which pictures a drastic background reduction for the first one at high excitation energies where the breakup effect of the projectile seems to be most important.

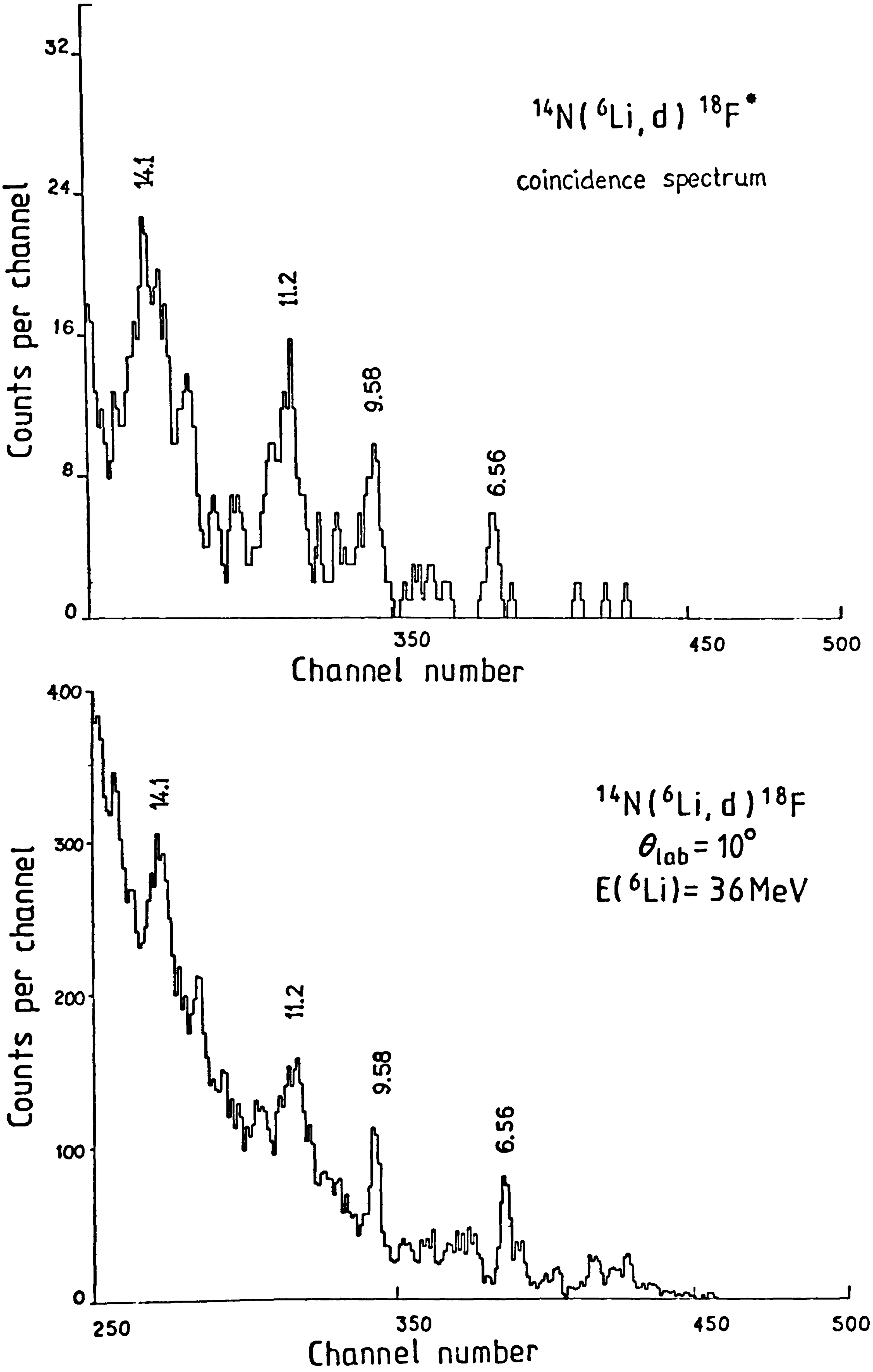

Figure 3.7 Coincidence and single spectra for ^{18}F

3.6 The 9.58 MeV State in ^{18}F

Spectra for particle decay from this state were obtained during on and off-line analyses asking for a coincidence requirement between the 9.58 MeV excited state in the deuteron spectrum and the five alpha counters. As far as different particle emission is concern, out of the ten angles measured, proton and deuteron decays were observed at a lower rate compared to the alpha one. These particle emissions were identified by their kinematical behaviour. Noticeably, all decays observed were leading to the ground state of the daughter nucleus. The corresponding percentages for the different decays are given in Table 3.2 being the alpha the predominant one. The number of α-d coincidences for this state were the lowest of the three levels analysed in ^{18}F. Even so, the correlation observed showed a clear and smooth ondulatory behaviour as can be seen in figure 3.8. The errors pictured in the experimental correlation are statistical only.

Gamow functions were obtained to represent the unbound 9.58 MeV state for each spin examined, and coupled to a DWBA code to describe the heavy system. The calculated reduced amplitudes were then used as input for an angular correlation computing code. The theoretical results were compared to the experimental values obtained (figures 3.8 and 3.9) and the chi-square test was performed. These latter results are shown in figure 3.10. All states with two L_α contributions gave structureless correlation functions. As explained before, for these states, a comparison was carried out in order to obtain the best $A_{\ell sj}$ and S matrix mixing. The displacement of the symmetry axis for the theoretical

Table 3.2

Particle Decay in ^{18}F

	9.58 MeV	11.2 MeV	14.1 MeV
alpha-decay	87 % ± 12	88 % ± 9	90 % ± 7
proton-decay	7 % ± 3	5.5 % ± 2	6 % ± 2
deut.-decay	6 % ± 3	6.5 % ± 2	4 % ± 1

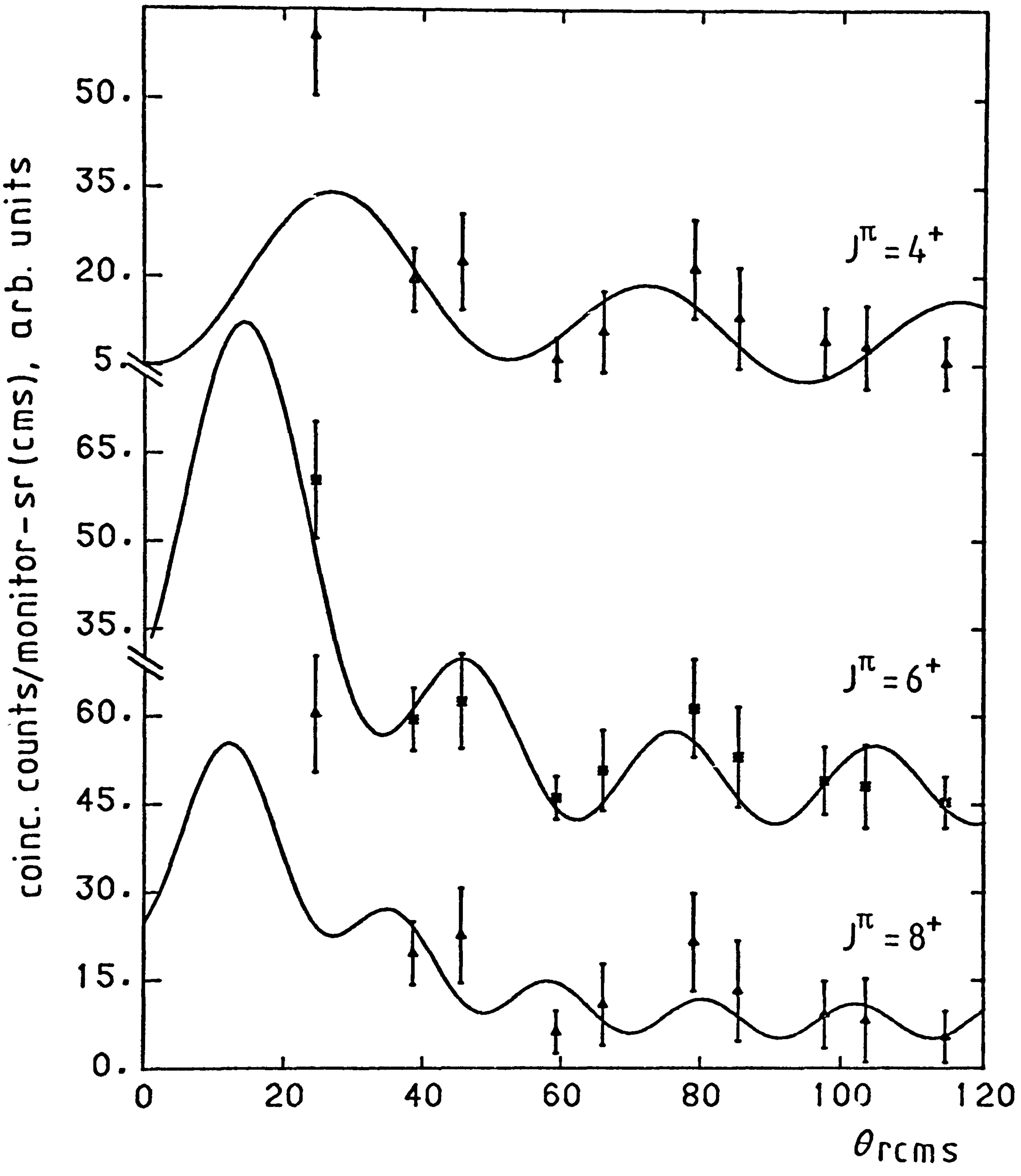

Figure 3.8 (α-d) angular correlation for the 9.58MeV state in ^{18}F. The three different fits are applied to the same data.

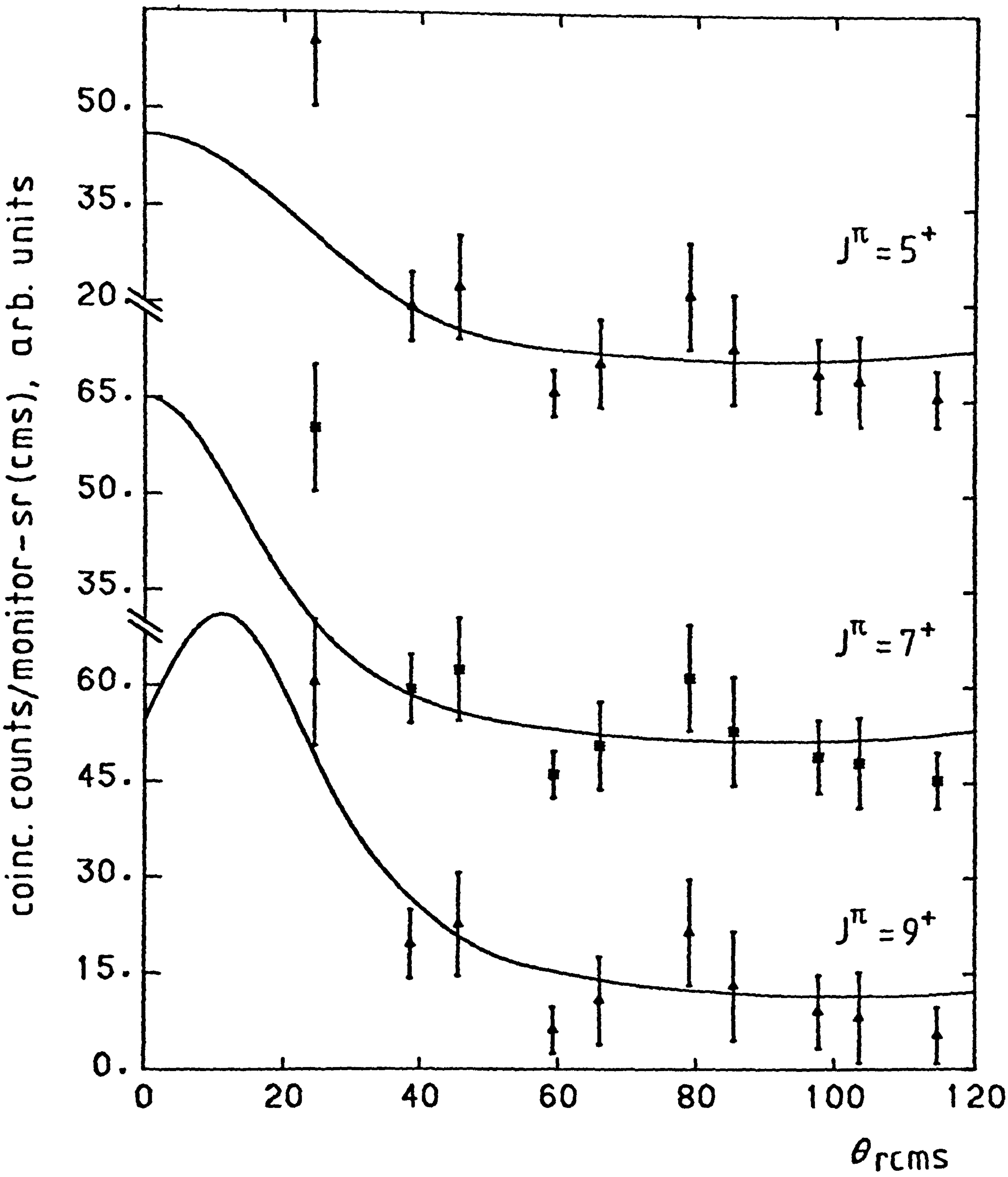

Figure 3.9 (α-d) angular correlation for the 9.58MeV state in ^{18}F. The three different fits are applied to the same data.

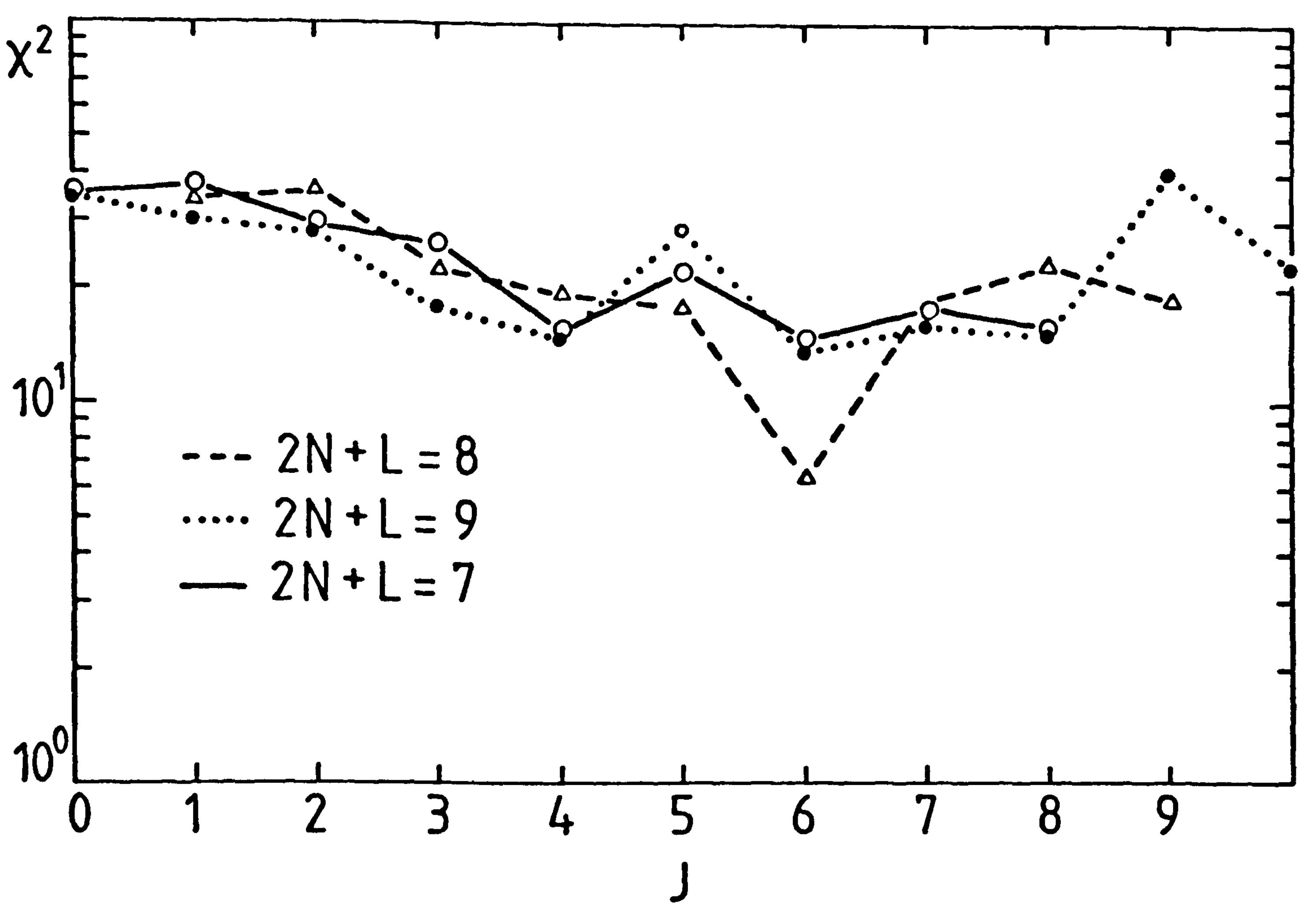

Figure 3.10 χ^2 values obtained in fitting different theoretical predictions to the (α-d) angular correlation data of the 9.58MeV state in ^{18}F. The lines are for guiding the eye in identifying each particular 2N+L band.

angular correlation predictions showed maximum values for low spins and a continuous decrease towards high spin values.

The χ^2 analysis shows a clear preference for 6^+ spin and parity assignment. The χ^2-test gives a probability for the 6^+ assignment of at least a factor of 7 larger than for the other spins, thus stressing the statement given above. In figure 3.8, different fits to correlation functions for even spins in the 2N+L=8 band are exhibited. Figure 3.9 shows similar comparisons with odd spin angular correlations. Further studies on the displacement of the symmetry axis were carried out since $J^\pi=6^+$ had been assigned. In figure 3.11 a plot of angular correlations in one degree steps for the centre of mass angle of the outgoing deuteron, shows a gradual loss of structure, as well as a shift of the maxima towards increasing angle values. The effect of using bound states for describing the heavy system on the displacement of the symmetry axis is displayed in figure 3.12. The measured preferred axis as well as the recoil and unbound state predictions are shown, and as can be seen a better agreement with the experimental value is found by the unbound description. The angular distribution analysis performed for this state is studied in Chapter 4.

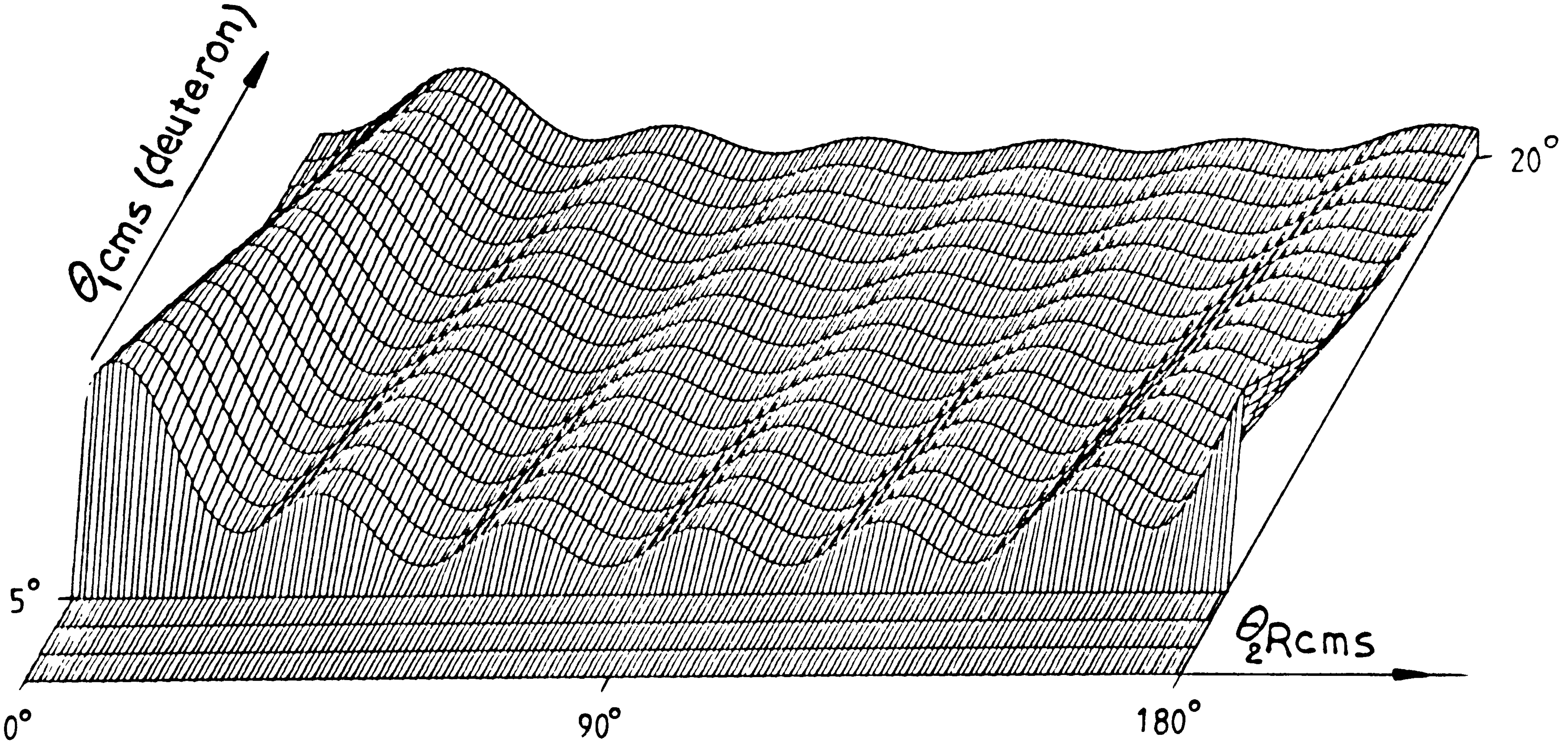

Figure 3.11 Double angular correlation function $W(\theta_{1d},\theta_{2\alpha})$ for the $^{14}N(^{6}Li,d)^{18}F$ (9.58MeV 6^+) --> $(\alpha)^{14}N$ reaction. Steps of one degree are shown for both, the deuteron detection angle in the centre of mass system and the α-detection angle in the recoil nucleus centre of mass system.

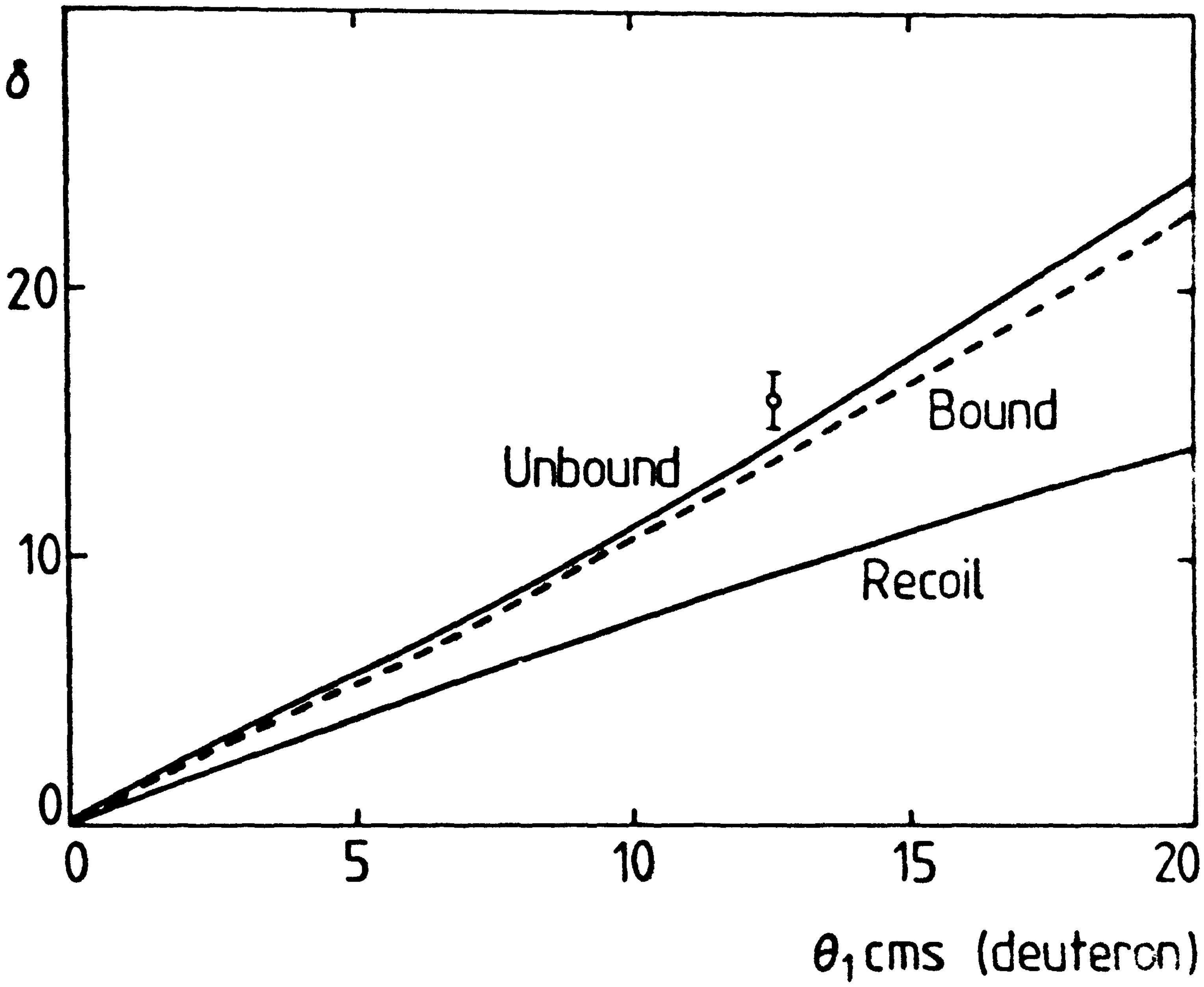

Figure 3.12 Displacement of the preferred axis as a function of the deuteron angle of detection for the 9.58MeV 6^+ state.

3.7 The 11.2 MeV State in ^{18}F.

The number of α-d coincidences registered for this state was higher than the observed for 9.58 MeV by a factor of ~ 2 (fig 3.7). Proton and deuteron decays to the ground state of their corresponding daughter nuclei were also detected, and the relative percentages given in Table 3.2. For the α-emission which was by far the predominant one, the experimental angular correlation shows a typical pattern found for states in which mixing of two L-values takes place (figures 3.13 and 3.14).

Several theoretical correlation functions can be regarded as good fits for the experimental data for different allowed spin values (figures 3.13 and 3.14). The results for these comparisons are shown in figure 3.15. The best chi-square values are obtained alternatively for odd spins with positive parities and even spins with negative parities in a range of angular momenta between 6 and 9. For the 2N+L=8 band, the χ^2 comparison shows a favoured 7^+ over the 9^+ assignment, while 2N+L=7 and 9 bands give almost indistinct preference to 6^- and 8^- spins.

In spite of the suggestive 2N+L=8 band structure which may be expected for alpha transfer reactions on ^{14}N, no spin assignment can be made, due to the lack of characteristic angular momentum shape.

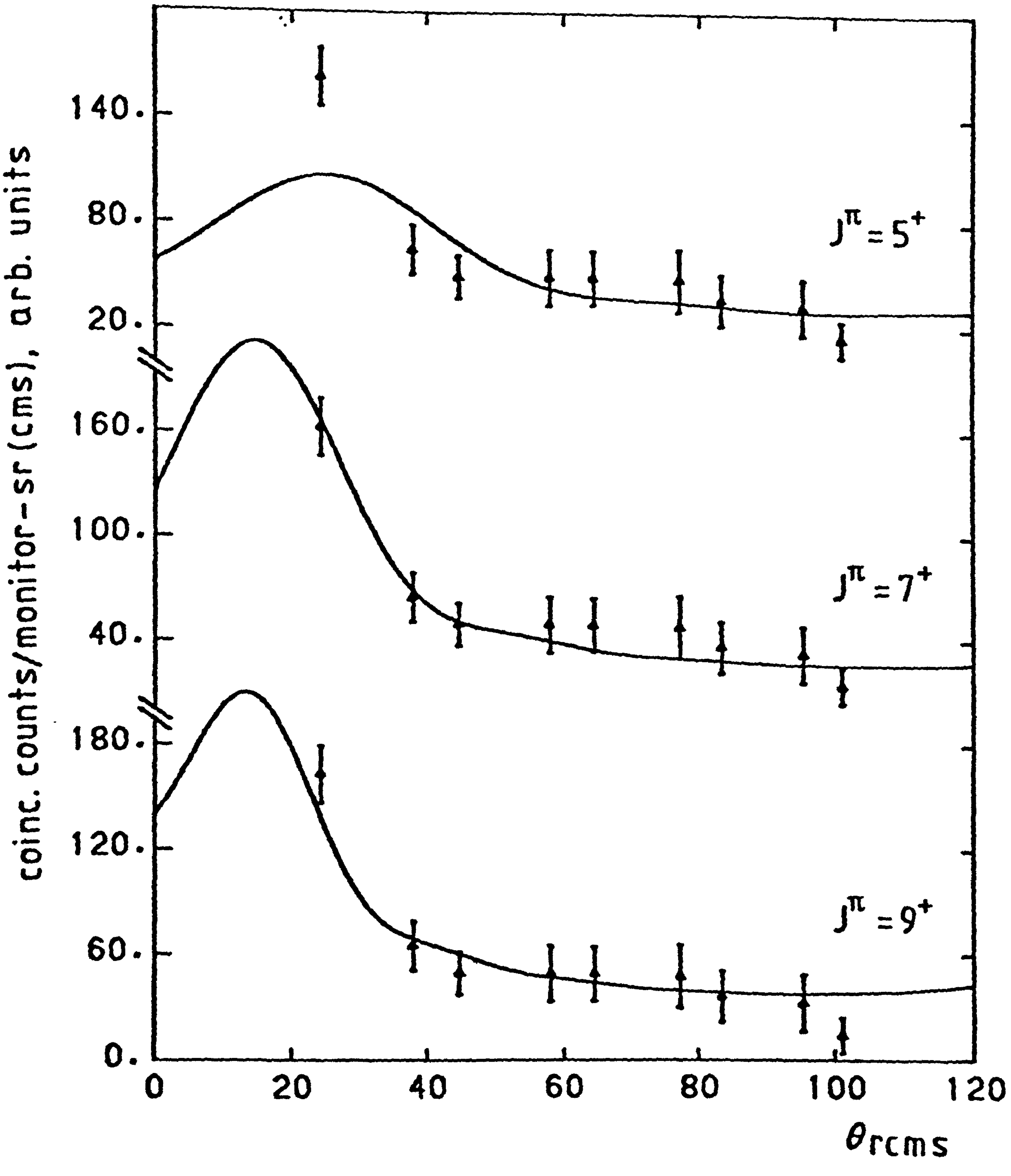

Figure 3.13 (α-d) angular correlation for the 11.2MeV state in 18F. The three different fits are applied to the same data.

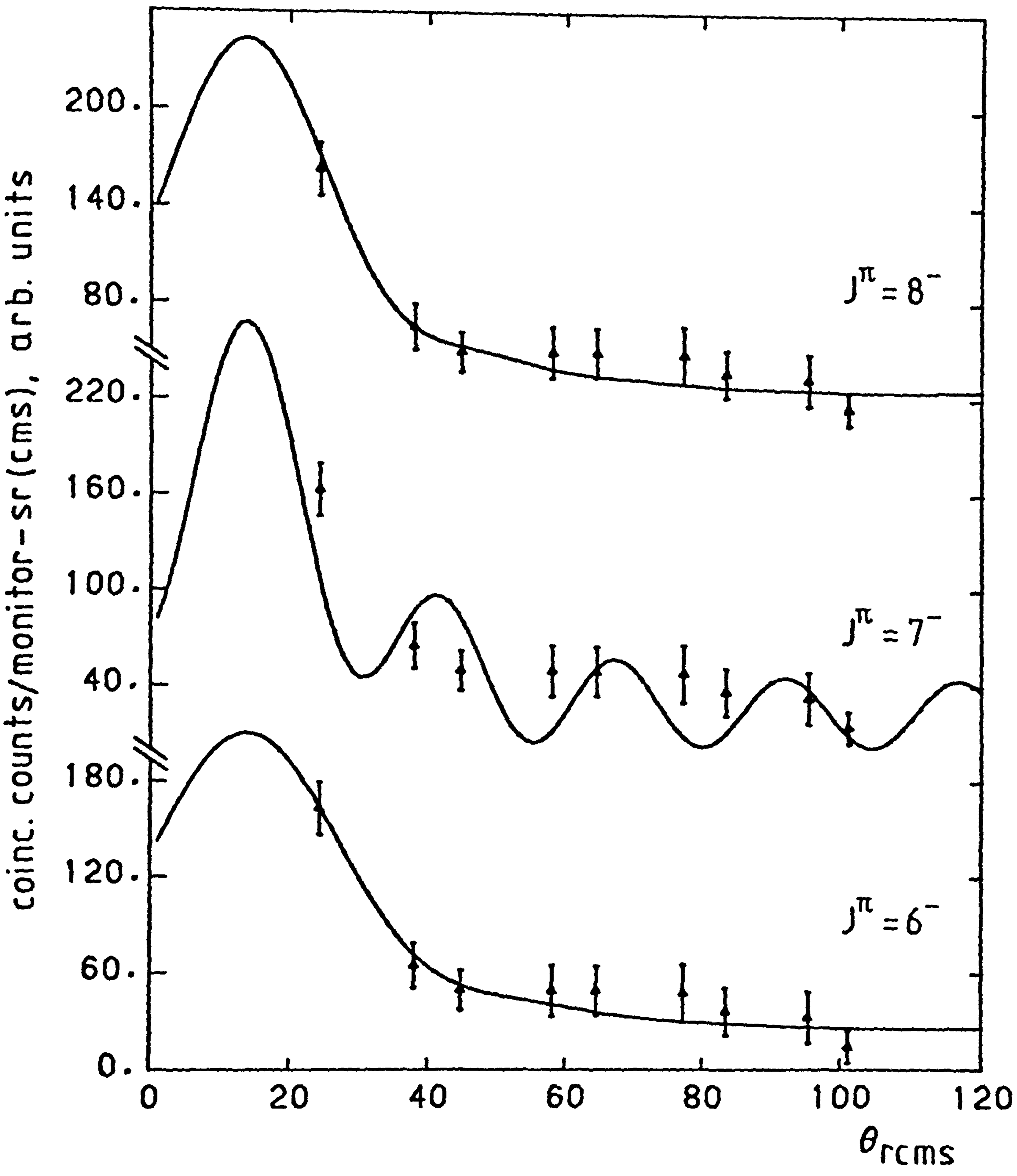

Figure 3.14 (α-d) angular correlation for the 11.2MeV state in ^{18}F. The three different fits are applied to the same data.

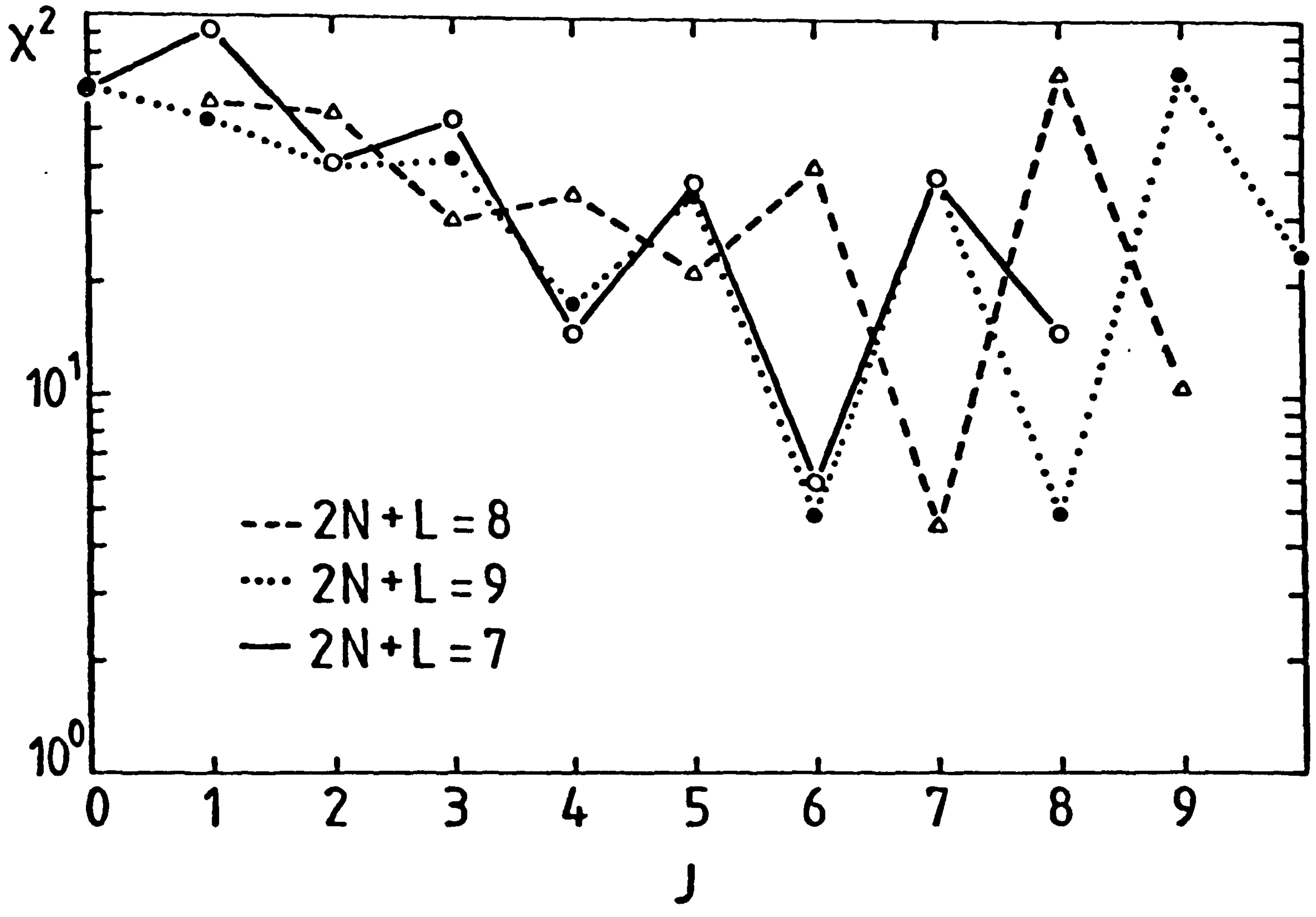

Figure 3.15 χ^2 values obtained in fitting different theoretical predictions to the (α-d) angular correlation data of the 11.2MeV state in ^{18}F. The lines are for guiding the eye in identifying each particular 2N+L band.

3.8 The 14.1 MeV State in ^{18}F.

The number of α-d coincidences for this state was larger than the one observed for 9.58 MeV by a factor of $\sim$ 3. Since the 14.1 MeV state lies on a high part of the continuous deuteron background, a larger random contribution was expected for this level than for the previously mentioned one. Careful studies of coincidences with neighbouring zones to the peak of interest were performed in order to estimate their contribution to the different spectra. Proton, deuteron and alpha decays were recorded, all leading to the ground state of the resultant nucleus. The percentages for the integrated contributions along the ten angles measured are shown in table 3.2

The experimental α-angular correlation obtained is pictured in figures 3.16 and 3.17. It shows a strongly ondulatory behaviour which matches preferably the theoretical correlation for the $J^{\pi}=8^{+}$ (2N+L=8). Again, odd spin with positive parity states, as well as the even spin with negative parity ones gave flat angular correlation predictions, as showed for some cases in figure 3.17. The different values obtained from χ^2 comparisons with all the spin possibilities considered (2N+L=7, 8 and 9) (figure 3.18) indicate clearly that the $J^{\pi}=8^{+}$ assignment is the favoured one. The χ^2-test gives a probability for an 8^{+} assignement of at least a factor of 20 larger than for the other spin assignements. All the procedure for obtaining the different angular correlations is similar to that described for the 9.58 MeV level, starting with a Gamow unbound wave function of the alpha particle. The DWBA parameters used are presented in Chapter 4.

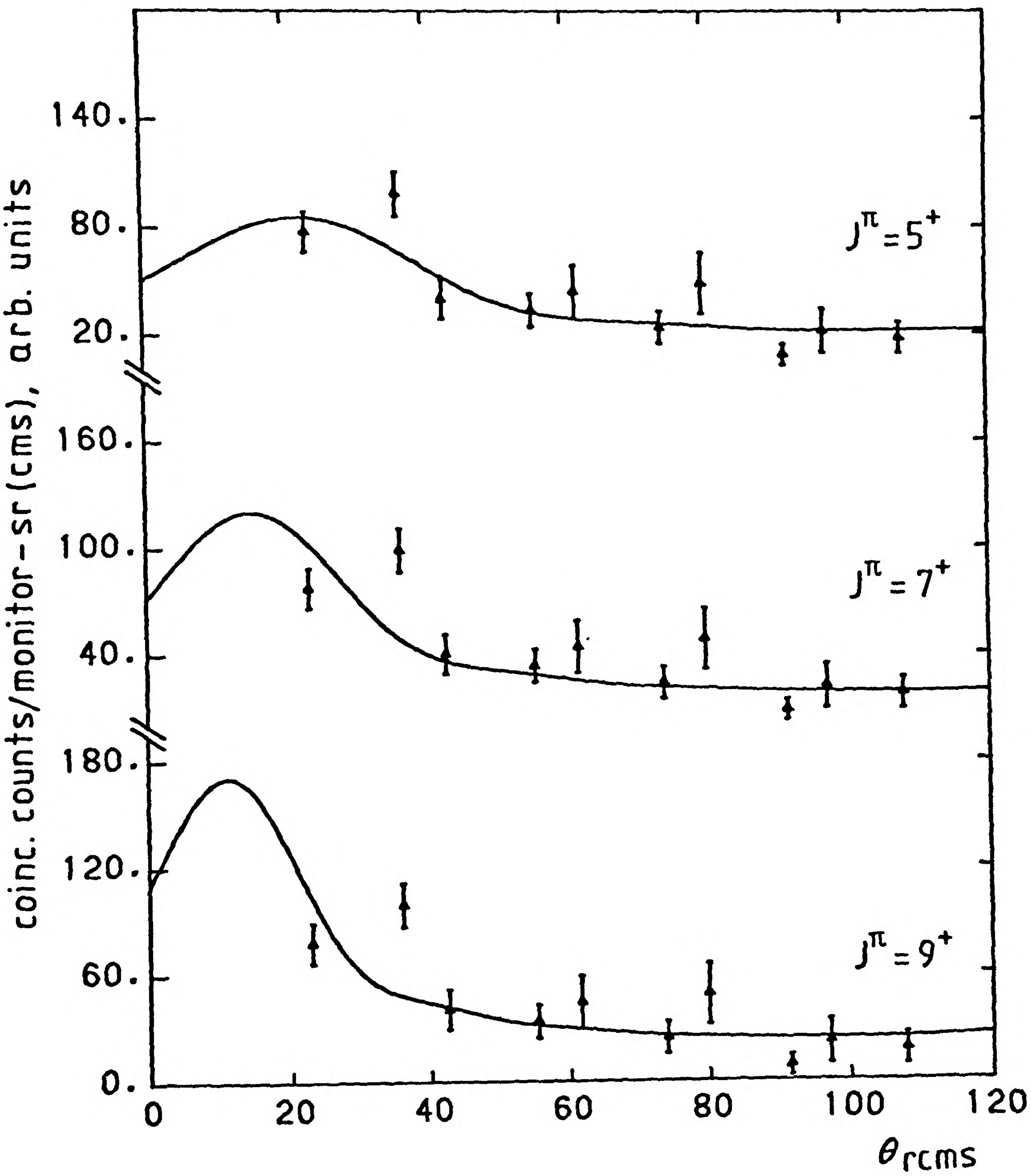

Figure 3.17 (α-d) angular correlation for the 14.1MeV state in ^{18}F. The three different fits are applied to the same data.

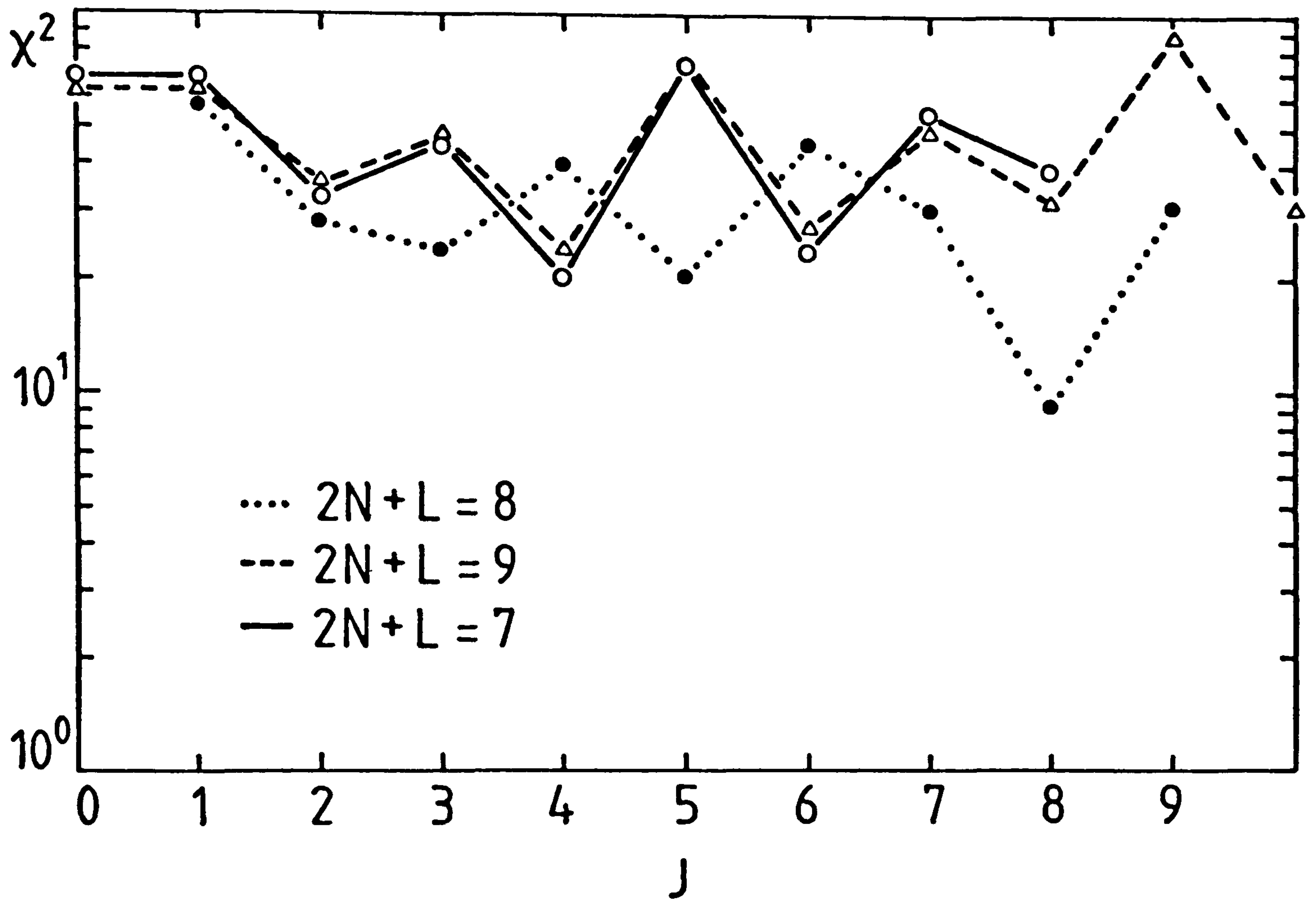

Figure 3.18 χ^2 values obtained in fitting different theoretical predictions to the (α–d) angular correlation data of the 14.1MeV state in ^{18}F. The lines are for guiding the eye in identifying each particular 2N+L band.

With the final spin assignment, a study of the displacement of the symmetry axis was performed. Figure 3.19 shows this effect for ejectile (deuteron) angles varying up to 20 degrees in the centre of mass system. Again, recoil and DWBA predictions can be compared to the actual experimental shift (figure 3.20) and a better agreement with the unbound state description is found.

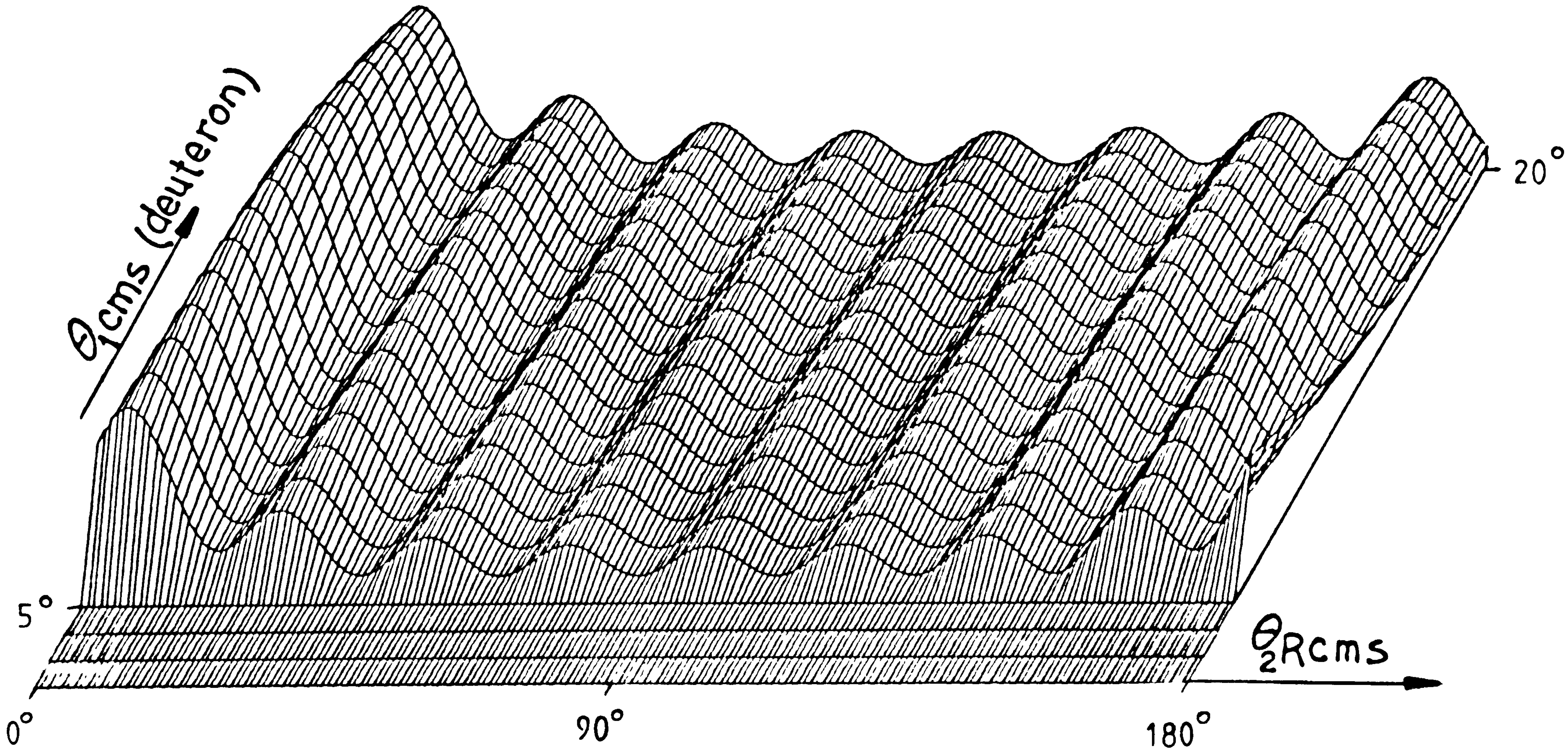

Figure 3.19 Double angular correlation function $W(\theta_{1d}, \theta_{2\alpha})$ for the $^{14}N(^{6}Li,d)^{18}F$ (14.1MeV 8^+) --> $(\alpha)^{14}N$ reaction. Steps of one degree are shown for both, the deuteron detection angle in the centre of mass system and the α-detection angle in the recoil nucleus centre of mass system.

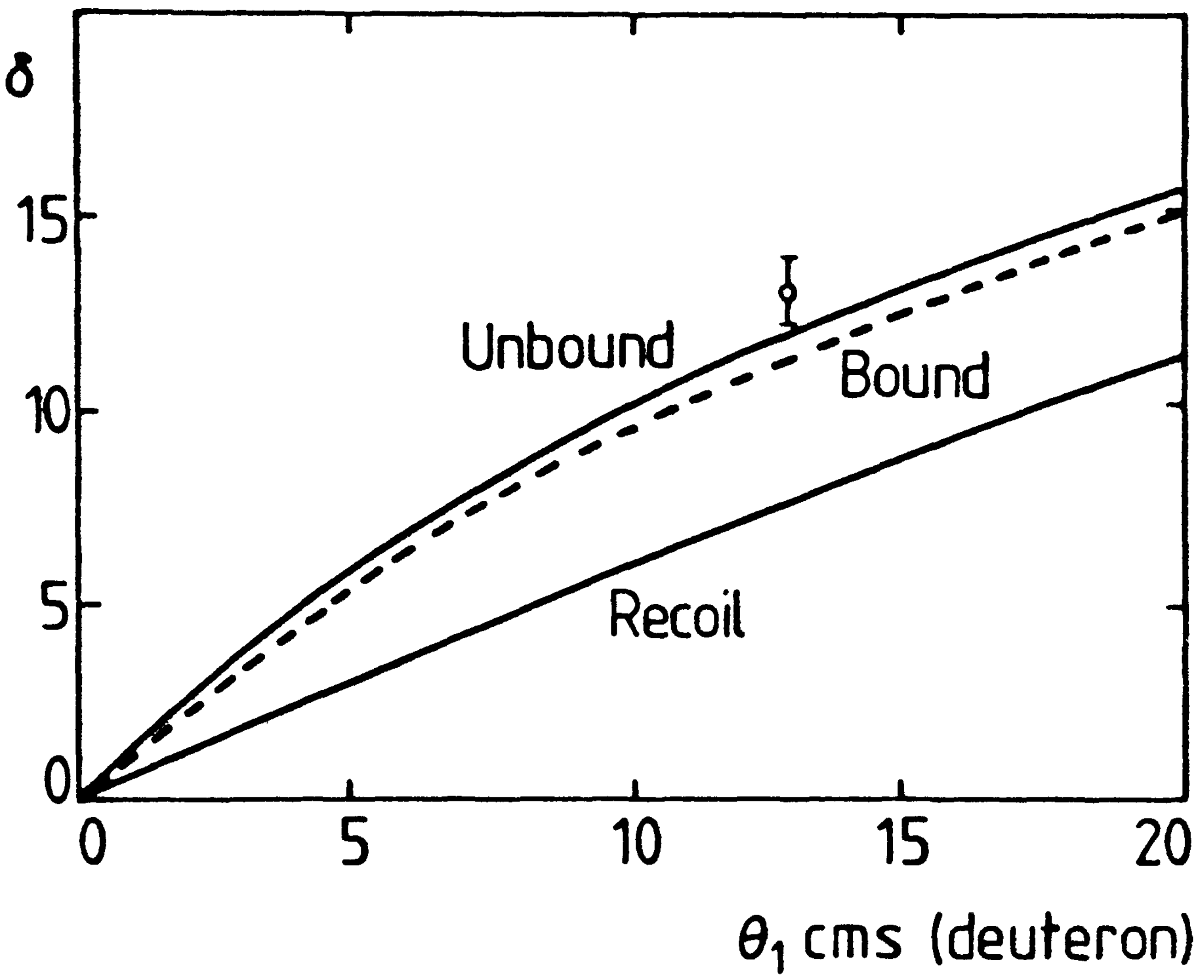

Figure 3.20 Displacement of the preferred axis as a function of the deuteron angle of detection for the 14.1MeV 8^+ state.

3.9 Discussion

The idea of using the α-cluster model to describe certain states in ^{18}F with the structure of an alpha particle coupled to a ^{14}N core has been supported by experimental evidence on the study of four nucleon transfer reactions on ^{14}N. Middleton et al. [MID68] performed the $^{14}N(^{7}Li,t)^{18}F$ reaction at 15 MeV of ^{7}Li and found a particularly strong population of ^{18}F states at 1.7, 2.10, 2.52, 3.36, 5.3, and 6.56 MeV. Cobern and Parker followed with the same experiment at a higher bombarding energy ($E(^{7}Li)=36.0$ MeV) and found that the selective population was taking place also for states between 6.5 and 15 MeV. Bradlow [BRA77] who studied the $^{14}N(^{11}B,^{7}Li)^{18}F$ and $^{14}N(^{13}C,^{9}Be)^{18}F$ alpha transfer reactions at 115 MeV of ^{11}B and 105 MeV of ^{13}C found strong excitations corresponding to levels at 5.3, 6.56, 9.58, 11.2 and 14.18 MeV. Buck, Friedrich and Pilt [BUC77b] applied the cluster model to ^{18}F and predicted the existence of two bands: (i) $K^{\pi}=1^{+}$ with J^{π} running from 1^{+} to 9^{+}, and (ii) $K^{\pi}=0^{+}$ with J^{π} progression 1^{+}, 3^{+}, 5^{+}, 7^{+}.

Experimental evidence for the existence of that $K^{\pi}=1^{+}$ band is found in the literature. Rolfs et al. [ROL73] carried out the identification of the first five members of such band (1^{+} (1.701 MeV), 2^{+} (2.523 MeV), 3^{+} (3.358 MeV), 4^{+} (5.298 MeV), 5^{+} (6.567 MeV)) and predicted the location of the next member $J^{\pi}=6^{+}$ at ~ 9.2 MeV. Out of their experimental measurements, Middleton et al. suggested that the 9.58 and 11.2 MeV states populated could be regarded as candidates for the 6^{+} and 7^{+} members of such a $K^{\pi}=1^{+}$ band.

The results of the angular correlations performed in this thesis work gave definite parity and spin assignments to two of the high lying states (6^+(9.58 MeV) and 8^+ (14.1 MeV)), while due to the structureless correlations of the 11.2 MeV state the parity and spin indetermination remains. An energy scheme for the 1^+ to 8^+ can be drawn (figure 3.21) assuming the 11.2 MeV state to be the 7^+ member of the band. A good agreement between the measured excitation energies and the patterns expected for the highest members of this band is shown here. On the other hand, as it will be seen in chapter 4, theoretical angular distributions for a supposed 7^+ state are found to give a fairly good fit in shape and magnitude to the 11.2 MeV experimental points. Further definite spin and parity identification for this level remains to be done.

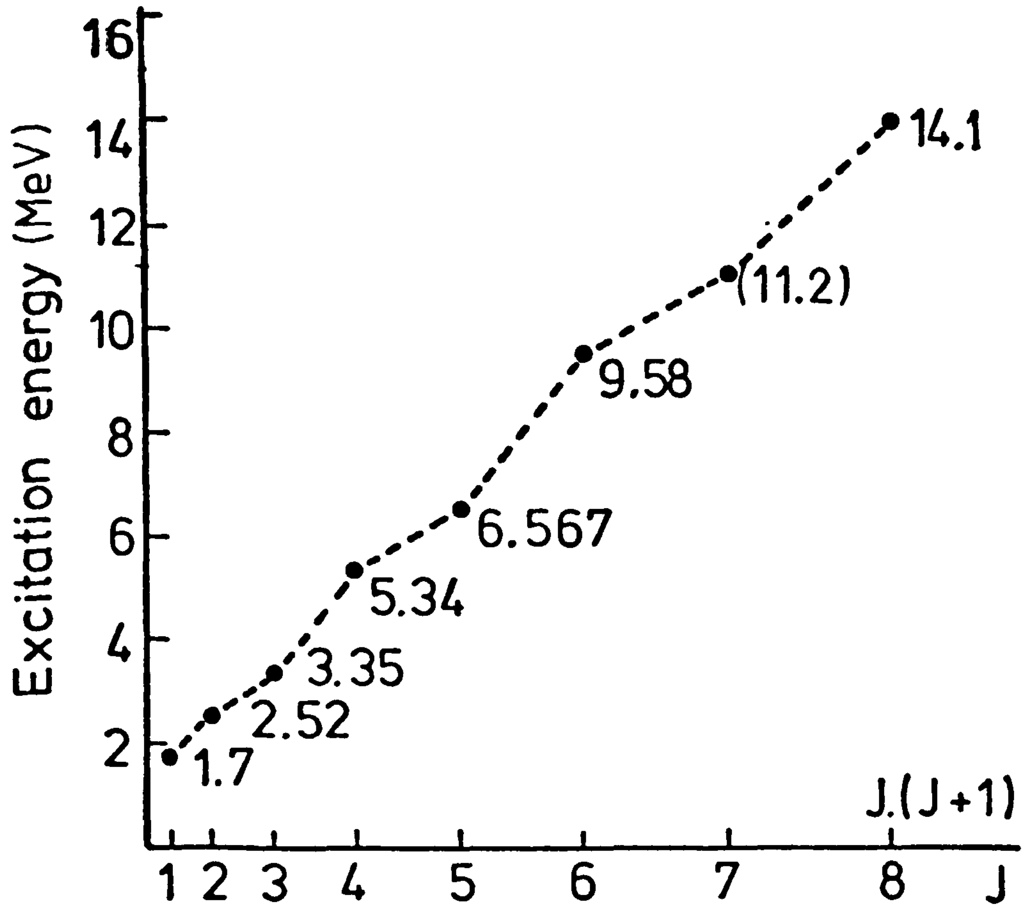

Figure 3.21 Energy scheme of the $K^{\pi}=1^{+}$ rotational band in ^{18}F

CHAPTER 4

$^{14}N(^{6}Li,d)^{18}F$. The Reaction Mechanism.

4.1 Introduction

The reaction $^{14}N(^{6}Li,d)^{18}F$ at bombarding energies high above the Coulomb barrier (E_{coul} = 5.11 MeV) is expected to be predominantly direct. Even so, reaction mechanism studies of (^{6}Li,d) reactions on neighbouring nuclei have shown for some cases (i.e. $^{12}C(^{6}Li,d)^{16}O$ at 20 MeV of ^{6}Li [MEI68]) an important contribution of the compound nucleus mode.

The $^{14}C(^{6}Li,d)^{18}O$ reaction studied by Cunsolo et al. [CUN81] at 34 MeV beam showed that the compound nucleus contribution accounts only for approximately 10% of all the experimental cross sections. Anantaraman et al. in their work on $^{16}O(^{6}Li,d)^{20}Ne$ [ANA78] found an appreciable compound cross section at 20 MeV of ^{6}Li and negligible contributions at 38 MeV of bombarding energies.

To assess the importance of compound nucleus mechanism in our reaction, Hauser Feshbach calculations have been performed. For obtaining direct reaction contributions, distorted wave Born approximation (DWBA) codes are commonly used. In heavy ion induced multinucleon transfer reactions, the zero range and no-recoil approximations are not appropiate for calculating the DWBA transition amplitude, and an exact finite-range DWBA (EFR-DWBA) calculation with inclusion of recoil effects should be performed. In this thesis, all the theoretical estimations for direct transfer contributions have been calculated with a modified [BRA77] version of the exact finite range computer code LOLA [DeV73]. In this version, cluster model wave functions can be obtained to calculate form factors. For the unbound states, Gamow functions can be read externally and extra terms for describing the interaction potential can be included.

4.2 The Experiment

A beam of 36 MeV ^{6}Li ions from the folded Tandem at Oxford was used to bombard ^{14}N gas targets enriched to 99.5%. Typical pressures of 100 Torr. were used in a thin aluminium window gas cell.

Angular distributions for stripping reactions as well as for elastic scattering were taken with slightly different detector arrangements. For the stripping reactions, a ΔE-E telescope semiconductor detector with ΔE component of 200 μm and the E one of 4.1 mm was used. This detector choice was important in order to get considerable ammount of energy for the ΔE signal of light particles to be processed in the PI calculation (Chapter 2), as well as to suppress elastically scattered ^{6}Li from being recorded in coincidence with E signals. The detector system was positioned at 8, 9, 11, 12, 14, 16, 18, 20, 23 and 26 degrees from the beam axis in the laboratory.

Very clear PI spectrum allowed good mass and charge separation. A typical deuteron spectrum taken at 16° is shown in figure 4.1. Overall energy resolution of about 250 kev was obtained.

For the elastic scattering, another ΔE-E telescope semiconductor detector was used; the ΔE component of 73.2 μm and the E one 2.2 mm thick. The laboratory angle was varied from 8 to 35 degrees.

Data were recorded event by event on magnetic tape and analysed on-line with a PDP 11/60 computer system (Chapter 2).

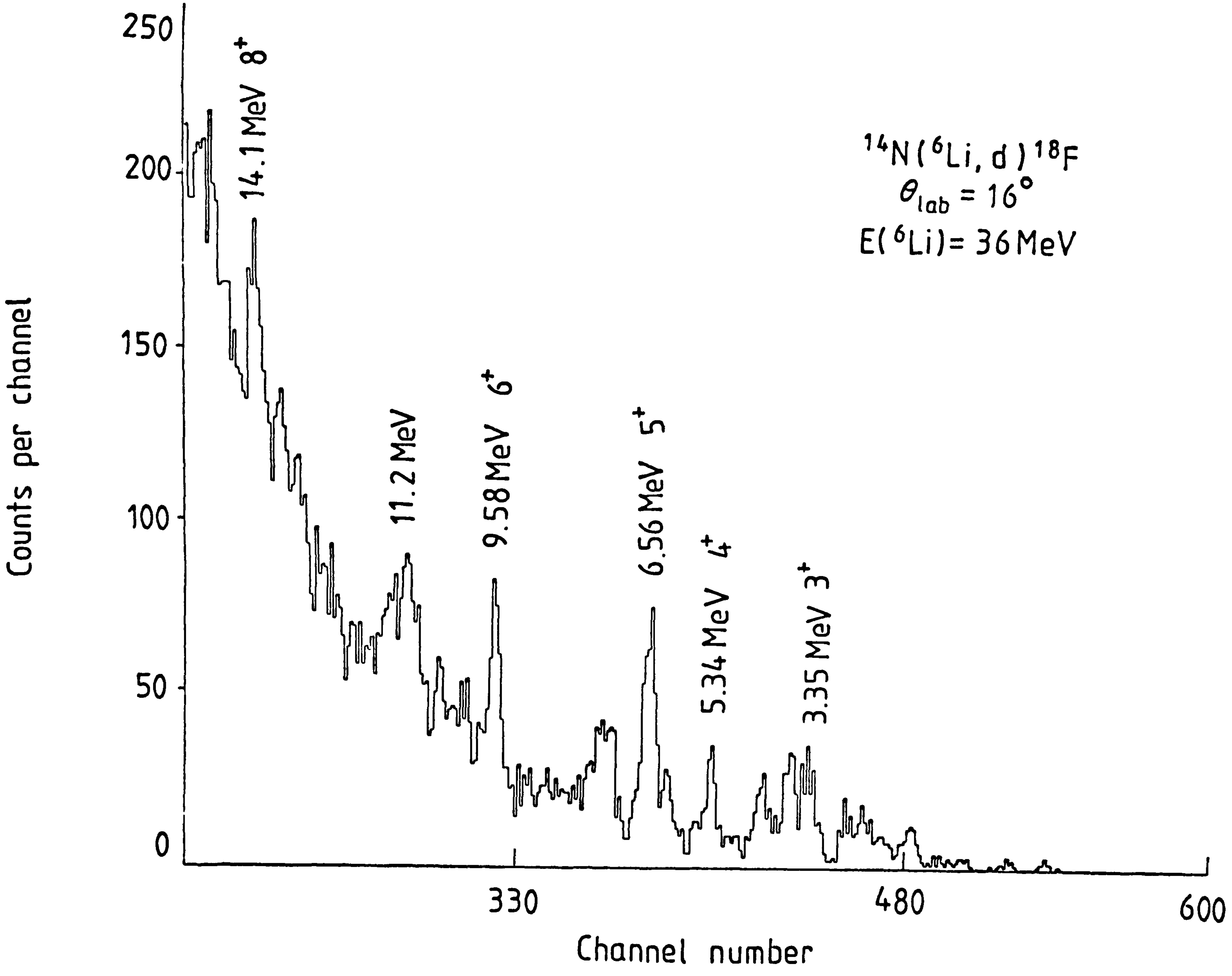

Figure 4.1 Deuteron energy spectrum for the $^{14}N(^{6}Li,d)^{18}F$ reaction at 36MeV and $\theta_{lab}=16°$

4.3 Optical Potentials

Typical optical potentials for the different channels involved are required for both, the compound nucleus and the direct transfer calculations. Optical potentials for the entrance channel have been obtained by fitting optical model predictions to the elastic scattering data collected using the experimental arrangement specified in Chapter 2.

The elastic scattering of a 36 MeV ^{6}Li beam off a ^{14}N gas target between 8 and 35 degrees in the laboratory system was measured. The angular distributions obtained as well as the optical model fits are shown in figure 4.2, with the corresponding parameters given in Table 4.1. The search on the parameters was performed with the code DWAVF which uses a modified version [RAE77] of the distorted wave routine used in the DWBA code MARS [TAM74].

The choice of optical potentials for the exit channels was more complex, since: (i) the optical potential which describes the ground state elastic scattering is not necessarily the appropriate prediction for an excited state in the residual nucleus and (ii) no data is available for elastic scattering of deuterons on the beta unstable ^{18}F. On the other hand, a wide range of optical potentials can be obtained from the literature for elastic scattering of deuterons on neighbouring nuclei [PER76], hence, sets of parameters which describe ^{2}H scattering over similar mass and charge ranges as well as equivalent centre of mass kinetic energies were sought. The final choice of potential parameters

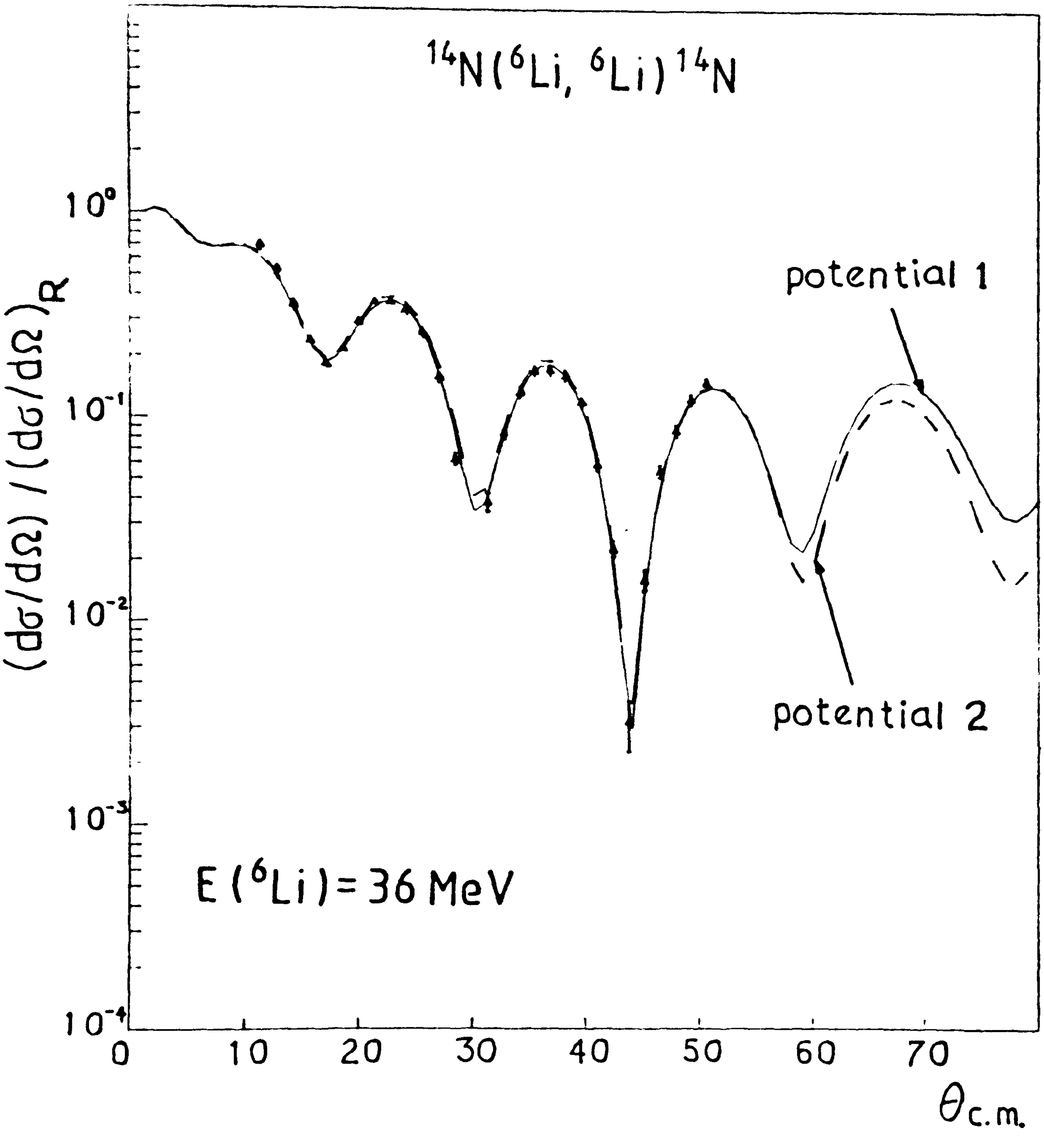

Figure 4.2 Angular distribution measured for ^6Li elastic scattering on ^{14}N at 36MeV bombarding energy. The theoretical curves are the optical model fits using potentials 1 and 2 of Table 4.1

TABLE 4.1

Optical Potentials used in EFR-DWBA calculations

Channel	$^{6}Li+^{14}N$	$^{6}Li+^{14}N$	$d+^{18}F$	$t+^{17}F$	$d+^{14}N$
V_o(MeV)	147.63	195.45	94.30	120.0	128.09
r_{ov}(fm)	0.971	0.782	1.027	1.15	1.00
a_v(fm)	0.543	0.653	0.806	0.70	0.697
W_o(MeV)	39.01	14.09	7.49	44.0	4.995
r_{ow}(fm)	0.504	1.106	2.175	1.15	1.946
a_w(fm)	1.273	0.878	0.560	0.70	0.856
r_{ow}(fm)	0.971	0.782	1.30	1.15	1.30
Reference	this work	this work	[DEH70]	[ROO65]	this work & [FIT67]
Number	1	2	3	4	5
Inc.Energy	36 MeV	36 MeV	15 MeV	6.8 MeV	11.8 MeV

The optical potentials are given by $U(r)=-V_o f_V(r,R_V,a_V)-iW_o f_W(r,R_W,a_W)+V_C(r)$, where $f_V(r,R_V,a_V)=\{1+\exp[(r-R_V)/a_V]\}^{-1}$, and similarly for $f_W(r,R_W,a_W)$;

$$V_C(r) = z_p Z_T \frac{e^2}{r} \qquad \text{for } r > R_C$$

$$= z_p Z_T \frac{e^2}{2R_C} \left(3 - \frac{r^2}{R_C^2}\right) \qquad \text{for } r < R_C$$

and $$R = r_o \left(A_p^{1/3} + A_T^{1/3}\right)$$

and the corresponding references are quoted in Table 4.1. The interaction potentials that have to be considered in the calculation of the transition amplitude are presented as well in Table 4.1, and the choice of the appropriate parameters found in the literature will be discussed later.

The compound nucleus calculation requires also the use of optical potentials for each of the intervenient channels. Their characteristic parameters, as well as the references where they were obtained from are quoted in Table 4.2.

TABLE 4.2

Level Density and Optical Model parameters used in HF calculations

Channel	^{6}Li+^{14}N	n+^{19}Ne	p+^{19}F	d+^{18}F	^{3}He+^{17}O	α+^{16}O
δ(MeV^{-1})	3.3	3.3	3.3	3.3	3.3	3.3
Δ (MeV)	0.0	2.25	2.25	0.0	2.25	4.5
Number of discrete levels	12	19	14	12	20	15
V(MeV) (a)	195.45	48.45	50.6	94.3	146.1	125.0
R_V(fm)	3.3	3.2	2.855	2.69	3.54	4.96
a_V(fm)	0.653	0.71	0.74	0.806	0.638	0.50
W(MeV)	(a) 14.09	(b) 7.06	(b) 7.10	(a) 7.49	(b) 22.08	(b) 5.0
R_W(fm)	4.67	3.2	3.41	5.7	3.499	4.96
a_W(fm)	0.878	1.0	0.7	0.56	0.636	0.50
R_C(fm)	3.3	3.34	3.2	3.47	3.214	3.527
V_{SO}(MeV)	-	5.0	8.0	-	-	-
R_{vso}(fm)	-	3.2	2.908	-	-	-
a_{vso}(fm)	-	0.71	0.74	-	-	-
Reference	this work	[LUT63]	[SWI73]	[DEH70]	[HAN68]	[DAV63]

(a) ——> Woods-Saxon (as in Table 4.1)

(b) ——> Woods-Saxon derivative W

δ ——> Level density parameter

Δ ——> Pairing parameter

The radii follow the definition given in Table 4.1

4.4 Compound Nuclear Calculations

Analyses of (^{6}Li,d) reactions in nearby nuclei at bombarding energies ranging between 20 to 38 MeV have shown considerable compound nucleus contribution for energies around the lower limit, to almost negligible effect at energies close to the upper limit.

Hauser-Feshbach calculations have been performed with the code STATIS [STO72] in order to estimate the importance of compound nucleus mechanism in our reaction. Six open channels including the elastic, protons, neutrons, deuterons, α-particles and ^{3}He channels were considered, following closely the pattern of references [DaS76, ANA79, and CUN81]. The optical parameters used are reported in Table 4.2. The comparison with experimental results are shown in figures 4.3 and 4.4. For the three highest energy levels analysed, several compound nucleus estimations are observed, since in principle these calculations were done for different possible spin values of these three states. As can be clearly seen, even the largest estimations for the compound nucleus mechanism do not seem to play any significant role for the final cross sections, in any of the levels studied here. It is well knwon that the magnitude of the cross section depends strongly on the level density parameter. All compound nucleus calculations shown in this chapter were carried out with level density parameters obtained from the literature for ^{6}Li,d reactions at similar bombarding energies to the one used in our experiments and for neighbouring targets and residual nuclei. Changes to a typical level density parameter suggested by Stokstad [STO72] for the s-d shell (a=2.88 MeV^{-1}) gave variations up to 30% which

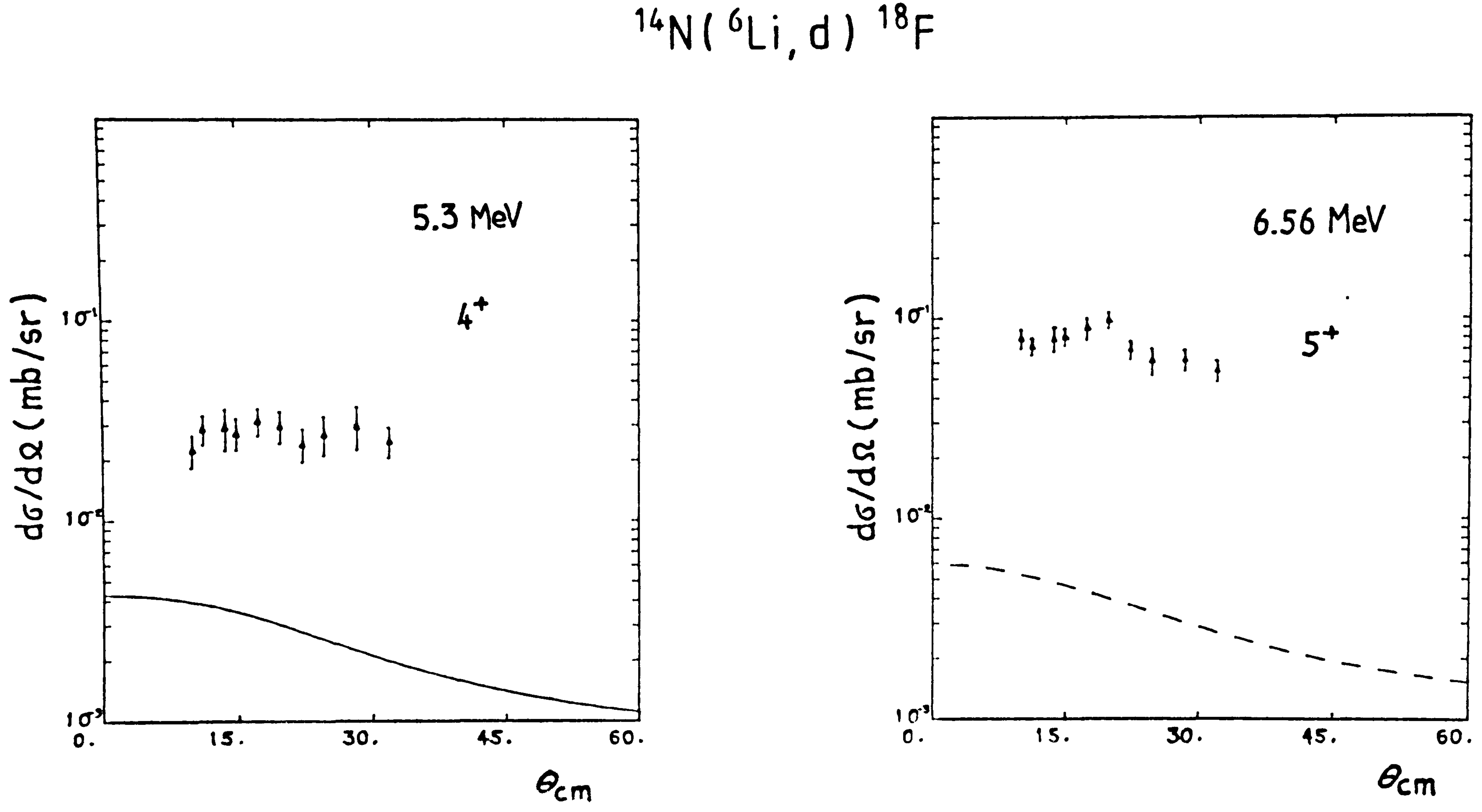

Figure 4.3 Angular distributions of deuterons from the $^{14}N(^{6}Li,d)^{18}F$ reaction at $E(^{6}Li)=36$MeV leading to the 5.3MeV 4^+ and 6.56MeV 5^+. The curves show Hauser Feshbach calculations.

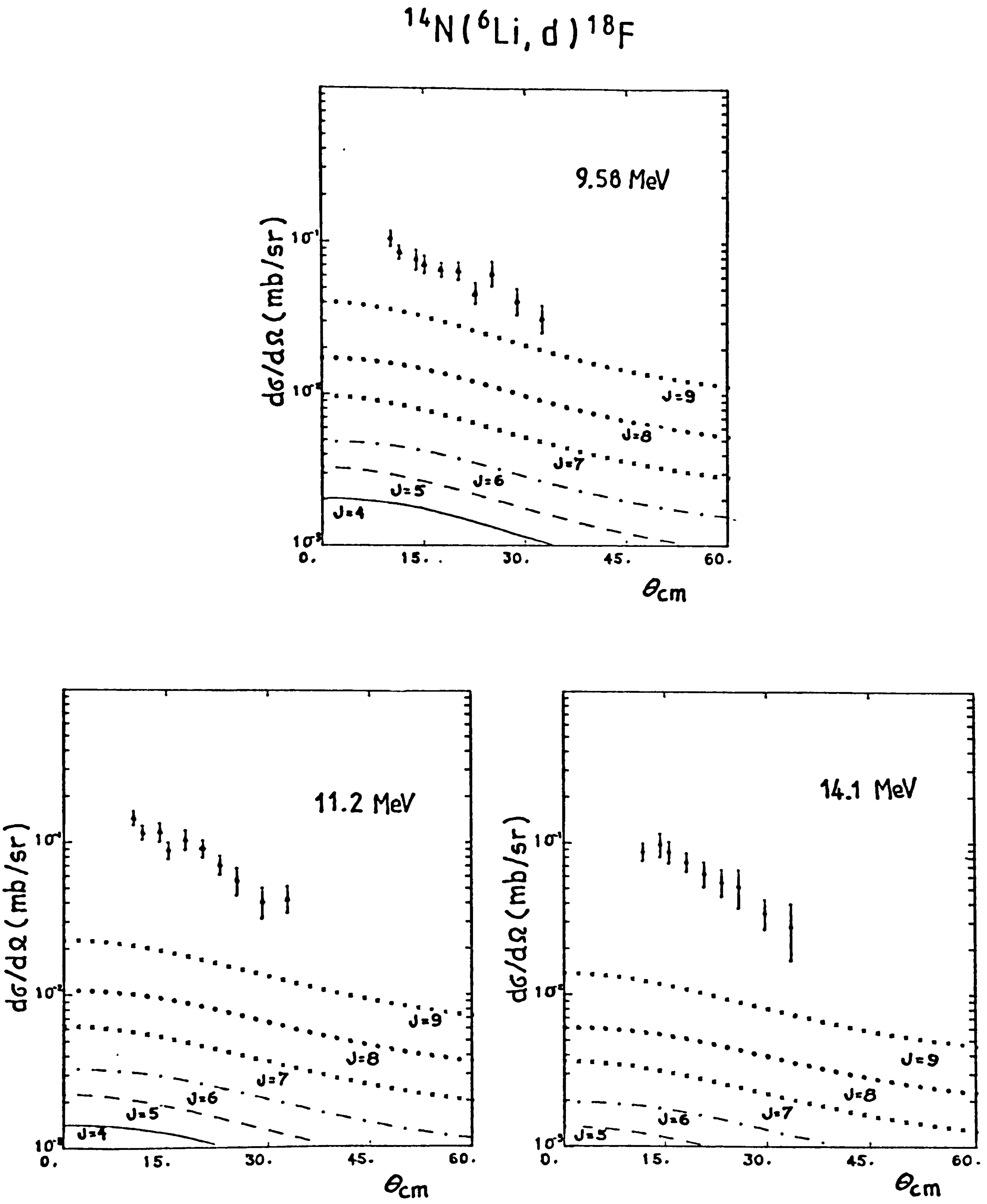

Figure 4.4 Angular distributions of deuterons from the $^{14}N(^{6}Li,d)^{18}F$ reaction at $E(^{6}Li)$=36MeV leading to the 9.58MeV, 11.2MeV, and 14.1MeV states. The curves show Hauser Feshbach calculations for different spin assumptions.

would nevertheless produce a small contribution to the present studies.

4.5 DWBA Calculations

4.5.1 Generalities

Quantitative analyses of the direct process contribution to the reaction dynamics have been performed by using the distorted wave Born approximation (DWBA). The first order DWBA theory has been treated extensively in the literature [AUS64, AUS70]. Two basic assumptions are made in this theory; (i) the transition between different mass partitions is weak compared to the elastic process and then first order treatment is allowed, and (ii) the coupling between inelastic or different mass partition channels is relatively weak, so the transfer from entrance to exit channels is performed by only one step. Highlights of the DWBA theory for cluster transfer reactions are shown in Appendix B. Briefly, the transition amplitude for the reaction A(a,b)B is written as [AUS64]:

$$T_{\alpha\beta} = \langle \Psi_B \Psi_b \chi_\beta^{(-)} (\vec{k}_\beta, \vec{r}_\beta) \; |\Delta V| \; \Psi_A \Psi_a \chi_\alpha^{(+)} (\vec{k}_\alpha, \vec{r}_\alpha) \rangle \tag{4.1}$$

where Ψ_B, Ψ_b, Ψ_A, Ψ_a are the internal wave functions for nuclei B, b, A and a respectively. $\chi_\beta^{(-)}$ and $\chi_\alpha^{(+)}$ are the distorted waves for the exit and entrance channels and ΔV is the interaction responsible for the transition.

The interaction ΔV can either be written in the post or in the prior representation as:

$$(\text{Post}) \qquad \Delta V = V_{bA}+V_{bx}-U_{bB} \tag{4.2}$$

$$(\text{Prior}) \qquad \Delta V = V_{bA}+V_{Ax}-U_{aA} \tag{4.3}$$

where V_{bA} represents the interaction between b and A, V_{bx} and V_{Ax} are the potentials used to bind the cluster x to b and A respectively, and U_{bB} (U_{aA}) is the distorting potential for the exit (entrance) channel. Post prior equivalence should be obtained if all the (correct) interaction potentials are used in order to calculate the form-factor.

Zero range and no-recoil approximations commonly used in light ion works for estimating the DWBA transition amplitude are not appropriate for the quantitative analysis of heavy ion transfer reactions. For that reason, recoil and exact finite range DWBA calculations have to be performed. Even more, all interaction potentials which are usually supposed to cancel, should be included in the transition amplitude in order to achieve post-prior agreement (this will be discussed in section 5.2).

An extension of the BDV model for the α-cluster unbound states in ^{18}F is used to calculate the wave functions in terms of Gamow states. Here, the parameterised form of the folding potential has been used to generate the radial wave functions of the relative cluster core motion. For the projectile description, the work of Kubo and Hirata [KUB71] for the $^{6}Li = d+\alpha$ was followed.

As already mentioned the EFR-DWBA calculations were performed with the compute code GAMOV and a modified version [BRA77] of the computing code LOLA. These DWBA calculations are very time consuming, mainly for large orbital angular momentum considered. Some typical values of the parameters involved in the time dependence of the code are shown below. For these figures, the accuracy of the calculations remains 5%.

lower and upper cut-off radius = 0.0 and 18.0 fm
lowest and highest partial waves = 0 and 40 ħ
mesh size for the form factor integration = 0.2 fm
mesh size for the distorted wave calculation = 0.1 fm and the average running times on a VAX/11 system are:

L-transfer	run time
4	43m
6	1h24m
8	2h12m

4.5.2 Post-Prior Equivalence

In the expression of the transition amplitude for the reaction A(a,b)B where a cluster x is transferred,

$$T_{\alpha\beta} = \langle \chi_\beta^{(-)}(\vec{r}_\beta)\Psi_\beta|\Delta V|\chi_\alpha^{(+)}(\vec{r}_\alpha)\Psi_\alpha\rangle \tag{4.4}$$

the potential responsible for the interaction (ΔV) can be expressed in either the post or the prior form.

$$\begin{aligned} &(\text{post}) \quad T_{\alpha\beta} = \langle \chi_\beta^{(-)}(\vec{r}_\beta)\Psi_\beta|V_\beta - U_\beta|\chi_\alpha^{(+)}(\vec{r}_\alpha)\Psi_\alpha\rangle \\ &(\text{prior}) \quad T_{\alpha\beta} = \langle \chi_\beta^{(-)}(\vec{r}_\beta)\Psi_\beta|V_\alpha - U_\alpha|\chi_\alpha^{(+)}(\vec{r}_\alpha)\Psi_\alpha\rangle \end{aligned} \tag{4.5}$$

where U_α (U_β) is the optical model distorting potential in the entrance (exit) a+A (b+B) channel; and $\chi_\alpha^{(+)}$ and $\chi_\beta^{(-)}$ the solutions of the optical potential equations:

$$\begin{aligned} \{T_\beta + U_\beta - E_\beta\}\chi_\beta^{(-)} &= 0 \\ \{T_\alpha + U_\alpha - E_\alpha\}\chi_\alpha^{(+)} &= 0 \end{aligned} \tag{4.6}$$

It has been shown [COT76] that ignoring non-orthogonality contributions between entrance and exit mass partitions, the post-prior equivalence in the calculation of $T_{\alpha\beta}$ is only dependent on the correct choice of the interaction potentials. If all interaction terms are included, similar cross sections should be obtained from the calculations. In general, for stripping reactions, it is customary to use the post form and the interaction potential is approximated by V_{bx},

$$\Delta V(\text{post}) = V_{bx} \tag{4.7}$$

the real potential which describes the cluster x bound to the core b, under the assumption that V_{bA} and U_{bB} of equation (4.2) cancel each other. In this Chapter, stripping reactions to unbound states of ^{18}F are studied, and as it is shown in Appendix C, these cases need the use of prior form in the calculation of the transition amplitudes. It is very important then to obtain post-prior agreement.

It has been shown by De Vries [DeV75] that in multinucleon heavy ion transfer reactions, post-prior discrepancies indicate that the interaction terms $V_{bA}-U_{bB}$ or $V_{bA}-U_{aA}$ usually neglected should be considered in the calculations. Coulomb parts for each of them have to be included as well, and he suggests for that the usual form of a uniform spherical charge.

V_{bx} and V_{Ax} are the real potentials used to calculate the cluster-core wave functions for a and B respectively, and U_{bB} and U_{aA} are the optical potentials used for the exit and entrance channels. For the potential V_{bA}, a model has to be given; De Vries suggests that since in heavy ion reactions the two cores never get too close, an optical potential description is an appropriate one, following the ideas of Tobocman [TOB73] and Smith [SMI71].

We have included in this work, all the interaction terms. Potential $V_{d,^{14}N}$ was approximated by a potential that fits the elastic scattering of deuterons off ^{14}N at a bombarding energy ~ E(^{6}Li) × (mass deut./mass ^{6}Li) ~ 12 MeV. Data were found in the literature for d+^{14}N at 11.8 MeV [FIT67]. The potentials obtained by Fitz et al. included spin-orbit terms, and as in the present code at Oxford there is no such possibility, a new optical potential was searched in order to fit their data. The results are shown in figure 4.5 and the parameters given in Table 4.1.

For testing the post-prior equivalence and the influence of including all the interaction terms, a bound state in ^{18}F (2^+ at 2.524 MeV) was used. The results obtained using post and prior forms with only the V_{bx} and V_{Ax} potentials respectively, the inclusion of the Coulomb terms and the V_{bA}, U_{aA} and U_{bB} potentials are shown in figure 4.6. As expected, there was a strong discrepancy in the resultant cross sections for the post and prior forms with the omission of V_{bA}-U. The Coulomb potentials do not appreciably change the calculated cross sections, but when considering the two terms V_{bA} and U a noticeable decreasing effect was observed for the prior form, reducing the discrepancies in the total cross sections to a 5.8%. This is a very encouraging and important result. The total cross sections for the six cases mentioned are shown in Table 4.3. The normalisation factors for all the cross sections shown in figure 4.6, were taken equal to one.

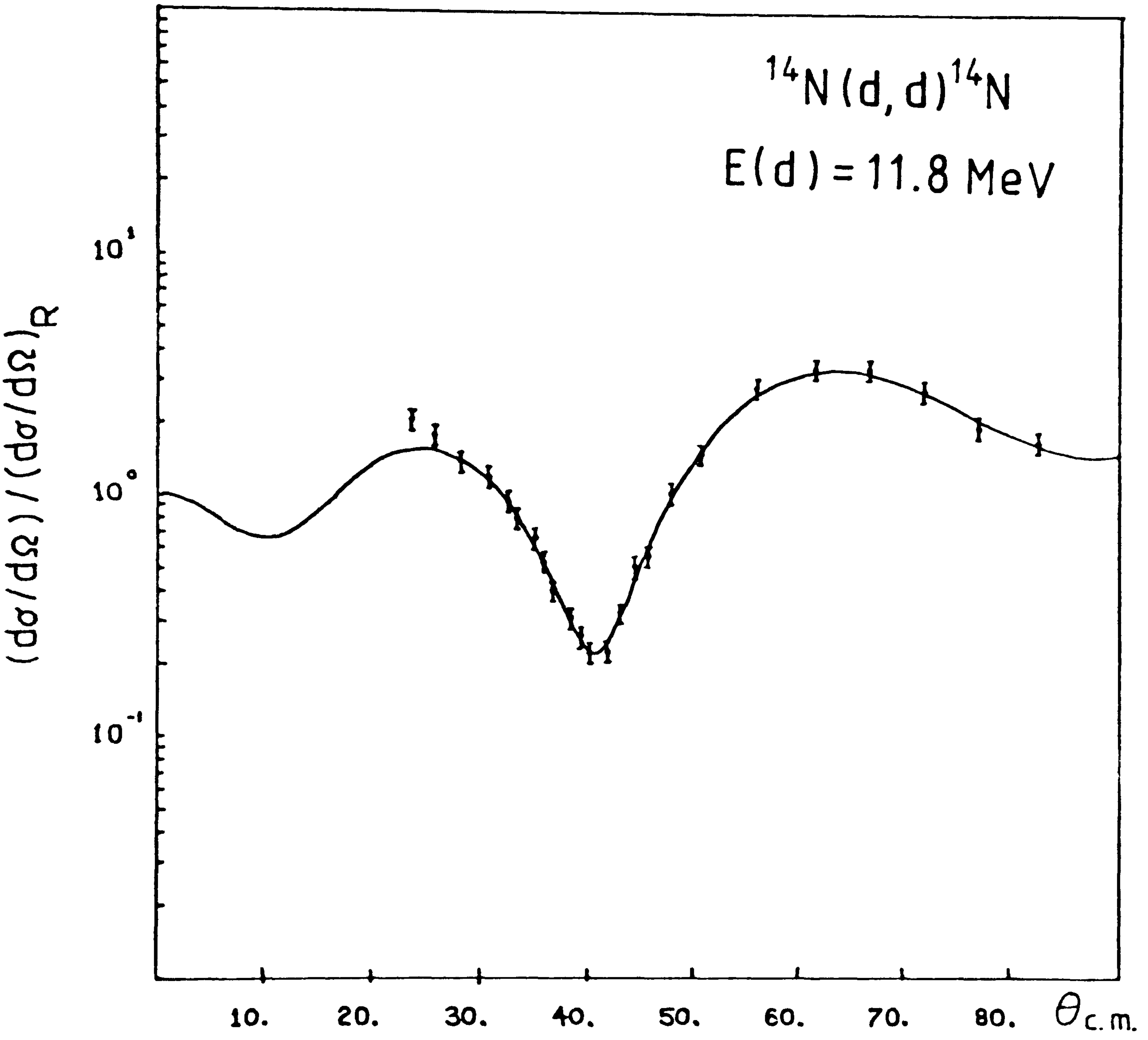

Figure 4.5 Angular distribution for ^2H elastic scattering on ^{14}N at 11.8MeV bombarding energy (data taken from [FIT67]). The theoretical curve is the optical model fit using potential 5 of Table 4.1.

TABLE 4.3

Effect of Extra Interaction Terms in the Cross Section

Case	$d\sigma/d\Omega(\theta_{cm}=20^o)$ (arb.units)	σ total (arb.units)
PR	0.953 E+00	0.246 E+00
PRC	0.941 E+00	0.243 E+00
PRT	0.388 E-01	0.573 E-02
PO	0.422 E-01	0.590 E-02
POC	0.395 E-01	0.561 E-02
POT	0.442 E-01	0.608 E-02

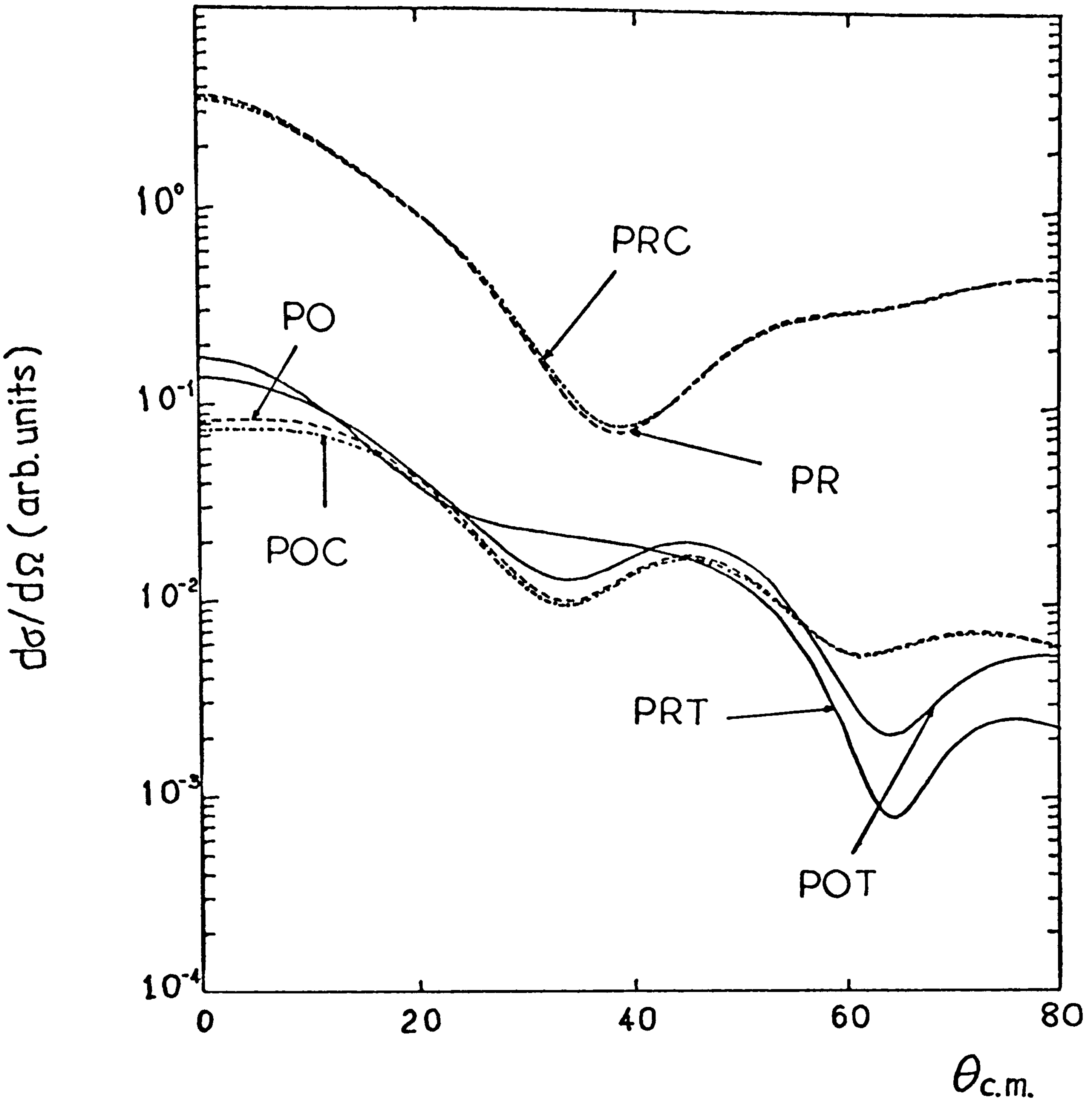

Form	$V_{cor-clu}$	$V_{cor-clu}+V_{coul}$	$V_{cor-clu}+V_{coul}+V_{bA}-U$
Prior	PR	PRC	PRT
Post	PO	POC	POT

Figure 4.6 Effect of interaction terms in DWBA calculations for $^{14}N(^{6}Li,d)^{18}F$ (2^+ at 2.524MeV). All calculations have normalization factor 1.

4.5.3 Form Factors

It has been seen in Chapter 3 that the simple BDV cluster model gives a fairly good description of α-cluster states, and therefore this formalism has been used in the calculation of the unbound Gamow wave functions to describe the states populated in ^{18}F. The alternative form of the cluster core potential given in Chapter 3 has been used throughout. Typical radius and diffuseness parameters have been taken from reference [BUC77]. The depths of the potentials were adjusted to fit the 'binding' energy of each state in the numerical calculations and are shown in Table 4.4 where also the single particle widths extracted from the complex part of the energy eigenvalue of the unbound states are shown.

The Gamow wave functions obtained were used in the DWBA code for the calculation of the transition amplitudes. The square of the absolute values for the real and imaginary parts of these Gamow state wave functions are plotted in figures 4.7, 4.8 and 4.9. For comparison the bound state solutions obtained with the DWBA code for the same parameterized cluster-core potential and using a fictitious binding energy of -0.1 MeV are also displayed. They show different asymptotic behaviour since for the unbound description the probability of finding the α-cluster at larger radii will be higher than for the bound model.

The potential obtained by Kubo and Hirata was chosen for the lighter system (α+d) potential. They postulated a very simple form of the $V_{\alpha d}$ interaction which gives a very good agreement in the shape of

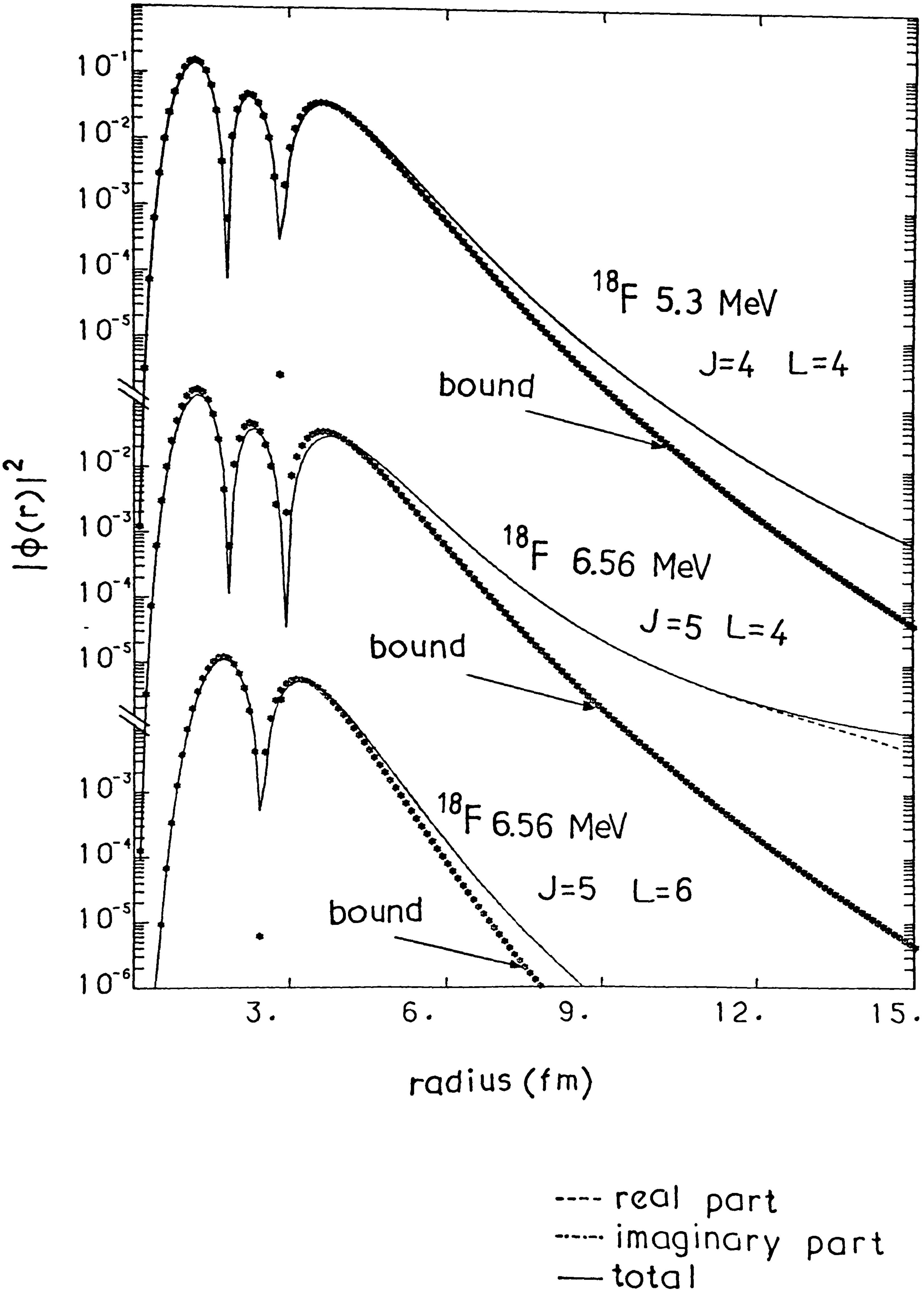

Figure 4.7 Gamow state wave functions for unbound states in ^{18}F. For odd spin states, where two different relative L values are involved, the relevant wave functions are shown. The slightly bound wave functions (-0.1MeV binding energy) are also plotted.

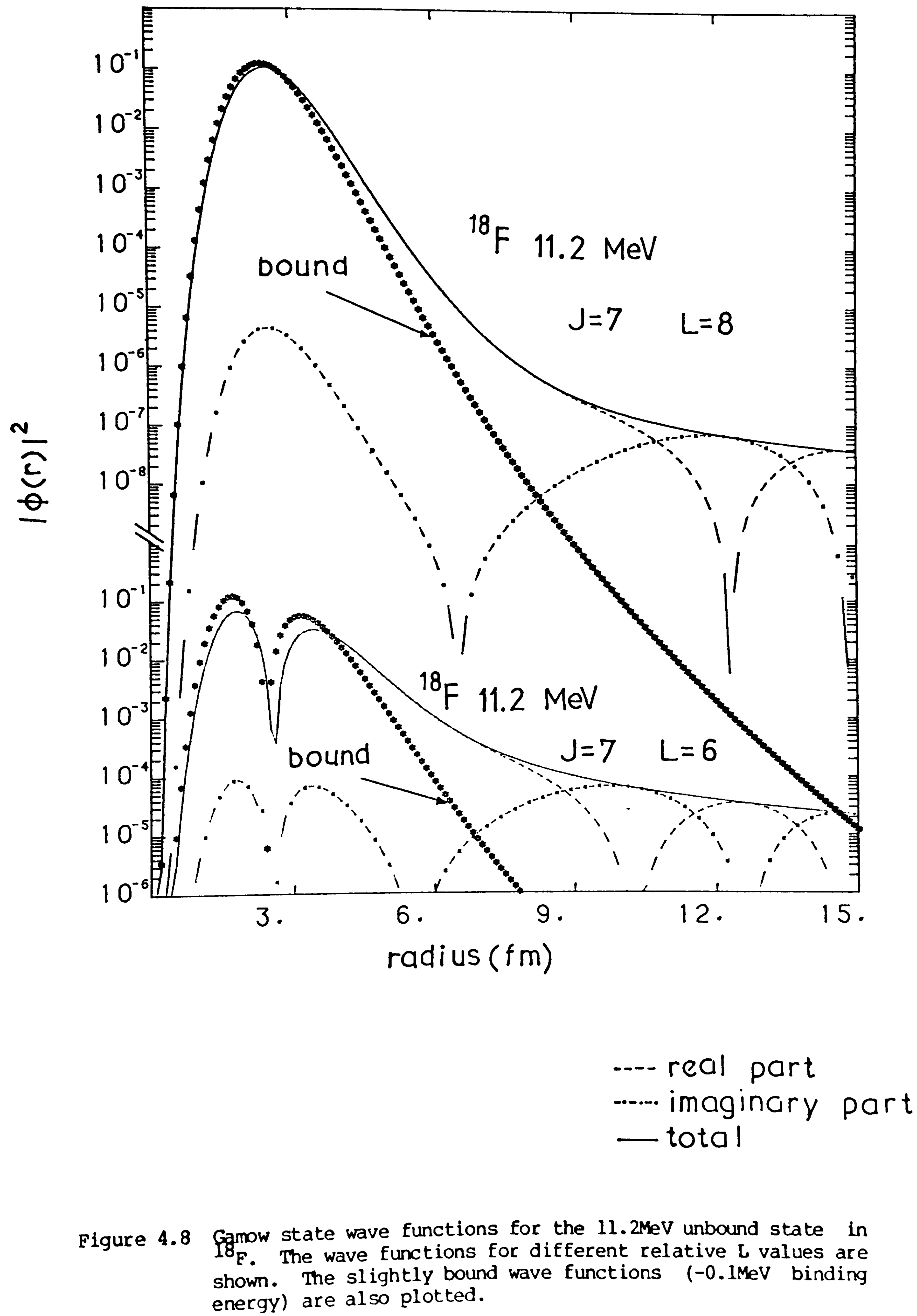

Figure 4.8 Gamow state wave functions for the 11.2MeV unbound state in ^{18}F. The wave functions for different relative L values are shown. The slightly bound wave functions (-0.1MeV binding energy) are also plotted.

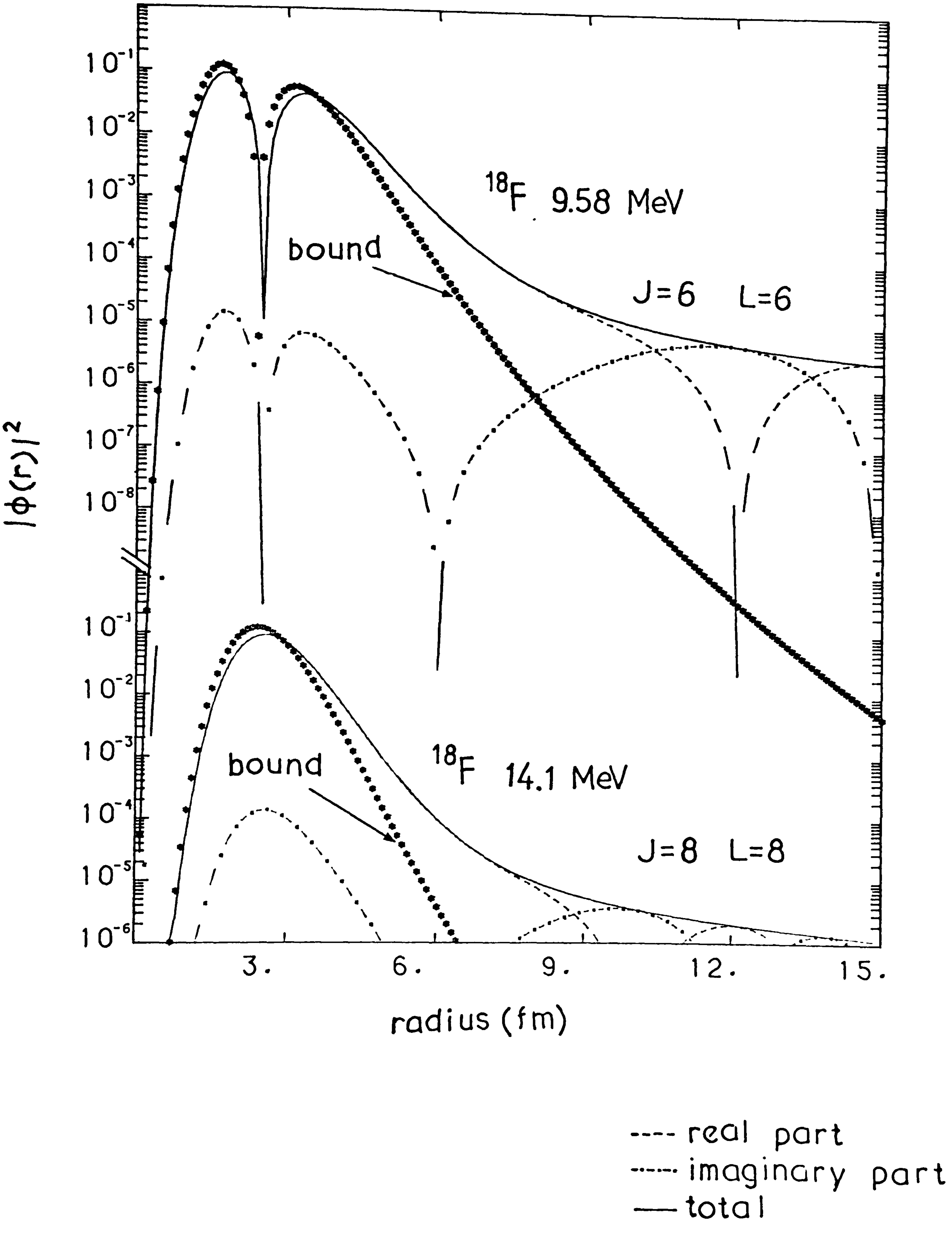

Figure 4.9 Gamow state wave functions for the 9.58MeV and 14.1MeV unbound states in ^{18}F. The slightly bound wave functions (-0.1MeV bindind energy) are also plotted.

TABLE 4.4

States in ^{18}F

Ex.E (MeV)	J^{π}	L	N	2N+L	Vdepth(-Vo) (MeV)	$\Gamma^{\alpha}sp$(MeV) calculated	Γ (MeV)* experiment.	Pot.Type
5.3	4^+	4	2	8	175.5	0.372 E-07	0.212 E-07	cosh
6.5	5^+	4	2	8	170.5	0.580 E-03	0.800 E-03	cosh
		6	1	8	188.8	0.636 E-06		cosh
9.58	6^+	6	1	8	178.7	0.527 E-02	0.550 E-01	cosh
11.2	(7^+)	6	1	8	172.6	0.503 E-01	-	cosh
		8	0	8	196.8	0.707 E-04		cosh
14.1	8^+	8	0	8	188.9	0.321 E-02	-	cosh

(*) from [AJZ78]

The potential for the α-cluster is given by :

$$V(r) = V_o\ f(r) + V_c(r)$$

with $$f(r) = \frac{1 + \cosh(R/a)}{\cosh(r/a) + \cosh(R/a)} \qquad \text{(cosh type)}$$

$$a = 0.8 \text{ fm} \qquad r_o = 0.555 \text{ fm}$$

and $V_c(r)$ the potential due to a charged sphere of radius R_c

$$r_{oc} = 0.764 \text{ fm}$$

for $$R = r_o\ (A_{\alpha}^{1/3} + A_{14_N}^{1/3}) = 2.25 \text{ fm}$$

and $$Rc = r_{oc}\ (A_{\alpha}^{1/3} + A_{14_N}^{1/3}) = 3.1 \text{ fm}$$

the potential as well as in the wave function, with the predictions of Hasegawa and Nagata [HAS67] for the two clusters in the ^{6}Li ground state, with exchange effects exactly treated. Kubo and Hirata assume a Woods-Saxon shape for the effective interaction, with radius parameter R = 1.9 fm and diffuseness a = 0.65 fm. With these parameters and the requirements of one node and L=0 for the relative motion of the clusters, the potential depth was adjusted by the program in order to give a separation energy of 1.473 MeV.

4.5.4 Spectroscopic Factors

In the expression for the differential cross section of a cluster transfer reaction A(a,b)B, the spectroscopic amplitudes for the dissociation of nucleus B into A and the cluster x, as well as of a into b and x, have to be explicitly taken into account. If we consider the cluster as formed by x particles in their lowest state of internal motion (relative S-state), and with its centre of mass carrying all the orbital angular momentum, the spectroscopic amplitude for the breakup of nucleus B into A and the cluster is given by the definition:

$$\Theta(L,S_x,T_x,J) = \binom{B}{x}^{\frac{1}{2}} \langle \Phi_B^{J_B T_B} | [\Phi_A^{J_A T_A} \{\Phi_x^{S_x T_x} \; \Phi_{NL}\}^{J T_x}]^{J_B T_B} \rangle \qquad (4.8)$$

presented by Anyas-Weiss et al. [ANY74] as a generalization of the one given by Ichimura et al. [ICH73] for α-particle clusters. Φ_A, Φ_B and Φ_x are the antisymmetrised internal wave functions of the nuclei A, B and x, and Φ_{NL} describes the motion of the cluster x around A. The nuclear states of A and B are commonly described by the shell model in terms of harmonic oscillator radial wave functions Ψ_A, Ψ_B. The x nucleons of the transferred cluster will occupy single particle orbits characterised by the quantum numbers $\tilde{n}_i=2n_i+l_i$, and the wave function which describes the x particles of the cluster in the nucleus B will be identified by Ψ_c. With these conventions, and making use of the Talmi-Moshinsky transformation, the spectroscopic amplitude is written:

$$\Theta(L,S_x,T_x,J) = \left(\frac{B}{A}\right)^{Q/2} \sum_c \{ \binom{B}{x}^{\frac{1}{2}} \langle \Psi_B | \Psi_A \Psi_c \rangle \} \; \langle \Phi_x \Phi_{NL} | \Phi_c \rangle \qquad (4.9)$$

where $Q=\sum_{i}^{x} n_i=2N+L$.

It is convenient to label the Ψ_c wave functions with Elliot's SU(3) scheme quantum numbers for calculating the second overlap in equation (4.9), since this representation has close connections with the cluster model [BAY58]. Ψ_c has SU(3) quantum numbers (Q,0)L; Φ_x and Φ_{NL} have SU(3) labels (0,0)0 and (Q,0)L respectively. Our cluster picture assumed the nucleons of the cluster to be in an internal S-state and its centre of mass carrying all the quanta.

Including coefficients for symmetrisation of Φ_x, the second overlap in (4.9) becomes:

$$\left(\frac{x!}{x_1!x_2!\ldots x_n!}\right)^{\frac{1}{2}} \frac{Q!^{\frac{1}{2}}}{x^{Q/2}} \prod_{i=1}^{x} \frac{1}{n_i!^{\frac{1}{2}}} \tag{4.10}$$

where x_1, $x_2,\ldots x_n$ correspond to the number of cluster nucleons transferred to different orbits.

For a direct four-nucleon transfer where a cluster with T=0, is considered, the description of its internal structure as an α-particle is the most likely one. In the $^{14}N(^{6}Li,d)^{18}F$ reaction, where states of a 4p-2h rotational band in ^{18}F are strongly populated, the cluster picture gives total quantum number $Q=8\equiv(sd)^4$. The function Ψ_c of equation (4.9) will carry SU(3) labels (8,0)L with L=8,6,4,2,0, and this description gives for equation (4.10) the value 0.196.

The quantity in curly brackets (equation (4.9)) was calculated for all the cases considered in this chapter (light as well as heavy system) by the Oxford shell model code [GOD79]. As predominantly 4p-2h structure was expected for the resultant ^{18}F states, and dominated by the $(sd)^4$ configuration, shell model calculations were performed for a ^{12}C core and six particles allowed in the 0p1/2, 0d5/2 and 1s1/2 orbits, and with the Reehal and Wildenthal [REE73] interaction. The members of the $K^{\pi}=1^{+}$ band strongly populated in this transfer reaction were searched. The resultant energies, percentage of 4p-2h and 2p-0h configurations for the different spins are shown in Table 4.5. The energies of several experimental states are very well matched, although the basis used is obviously largely truncated. The overlaps between the states obtained with this shell model description, and the $(sd)^4$ cluster states were calculated (expression in curly brackets in equation (4.9)) and the values obtained also shown in Table 4.5. It can be seen that the highest amplitudes are the ones predicted for the states strongly populated in the reaction, and these were then used for the theoretical spectroscopic factors.

A similar analysis was performed for the lighter system, ^{6}Li gs $=\alpha+d$, and values for the contribution of different relative L values were obtained. They showed 91.78% of L=0, 0.58% of L=1 and 7.64 % of L=2, with values for the overlaps of 0.958, 0.076 and -0.276 respectively.

The study performed for both, heavier and lighter system would in principle allow estimations for the absolute theoretical spectroscopic factors, but some considerations on this respect have to

TABLE 4.5

Four nucleon parentage amplitudes for $\lambda\ \mu(8,0)$ transfer on ^{14}N

^{18}F states	Ex.E(MeV) (theoretical)	Ex.E(MeV) experimental	% of 4p-2h	% of 2p-0h	L	REWIL Inter. overlap
1^+_1	0.0	0.0	31.2	64.4	0	-0.078
					2	0.0002
1^+_2	1.879	1.7	95.0	0.20	0	-0.528
					2	0.041
2^+_1	3.03	2.52	64.1	27.6	2	0.455
2^+_2	3.65	3.06	73.1	24.6	2	0.651
3^+_1	0.314	0.937	27.0	69.4	2	-0.023
					4	-0.036
3^+_2	3.12	3.35	94.9	1.40	2	0.651
					4	-0.018
3^+_3	4.07	4.119	47.5	31.0	2	0.166
					4	0.257
4^+_1	5.56	4.65	46.8	-	4	-0.340
4^+_2	6.07	5.298	78.5	-	4	0.726
5^+_1	0.77	1.12	29.0	67.1	4	-0.010
					6	0.072
5^+_2	5.69	6.56	96.1	0.60	4	-0.826
					6	-0.014
6^+_1	8.54		35.6	-	6	-0.009
6^+_2	9.71	9.58	89.8	-	6	-0.844
7^+_1	9.22	(11.22)	96.3	-	6	0.912
					8	0.031
8^+_1	13.84	14.18	93.6	-	8	0.967

be pointed out.

In theory, the radial wave function Φ_{NL} which describes the relative motion between B and x has to be the same as that used in the description for the cluster state in the form factor, where a fairly realistic wave function is generated by the cluster-core potential of the BDV model . For the direct transfer reactions, the wave function that describes the cluster core system must have a realistic shape at the nuclear surface, since most of the transfer takes place at this region and therefore, the use of harmonic oscillator wave functions is not recomendeed On the contrary, when calculating the second overlap in equation (4.9), harmonic oscillator wave functions were assumed for simplicity and this introduces errors in the spectroscopic amplitude. It will be more realistic then, when comparing theoretical calculations with the experimental data for the angular distributions, to consider relative theoretical to experimental spectroscopic factors, rather than their absolute values.

4.6 Comparison of the DWBA Predictions with the Experiment

The experimental cross sections obtained in the $^{14}N(^{6}Li,d)^{18}F$ reaction and the best normalisations for the DWBA calculations are shown in figures 4.10 and 4.11. The coefficients used for normalising the theoretical DWBA predictions and the spectroscopic factors calculated as studied in the previous section, are shown in Table 4.6. Fairly good agreement in shape and magnitude is observed for the five states. Even the attempted 7^+ calculation for the 11.2 MeV state seems to reproduce the experimental shape.

It has been pointed out that due to the use of harmonic oscillator wave functions for the theoretical spectroscopic factor calculation, attention should be focused to their relative values rather than to the absolute ones. Other ambiguities strengthen this view: possible errors in the two body interaction, ambiguities in the optical and bound state parameters, and approximations performed by the DWBA theory.

Very good agreement between experimental and relative spectroscopic factors is found for the 4^+ at 5.3 MeV and the identified 6^+ and 8^+ states (at 9.58 and 14.1 MeV). Fairly good agreement is found for the 6.5 and 11.2 MeV states which show normalisation values that differ by approximately 35% from the relative spectroscopic factors. As explained in previous sections, for the odd spin states, two L contributions have to be considered L=J-1 and J+1. The 5^+ and 7^+ cross sections will arise from an incoherent sum of L=4 and 6 and L=6 and 8 DWBA calculations respectively. For those cases, the theoretical parentage amplitude

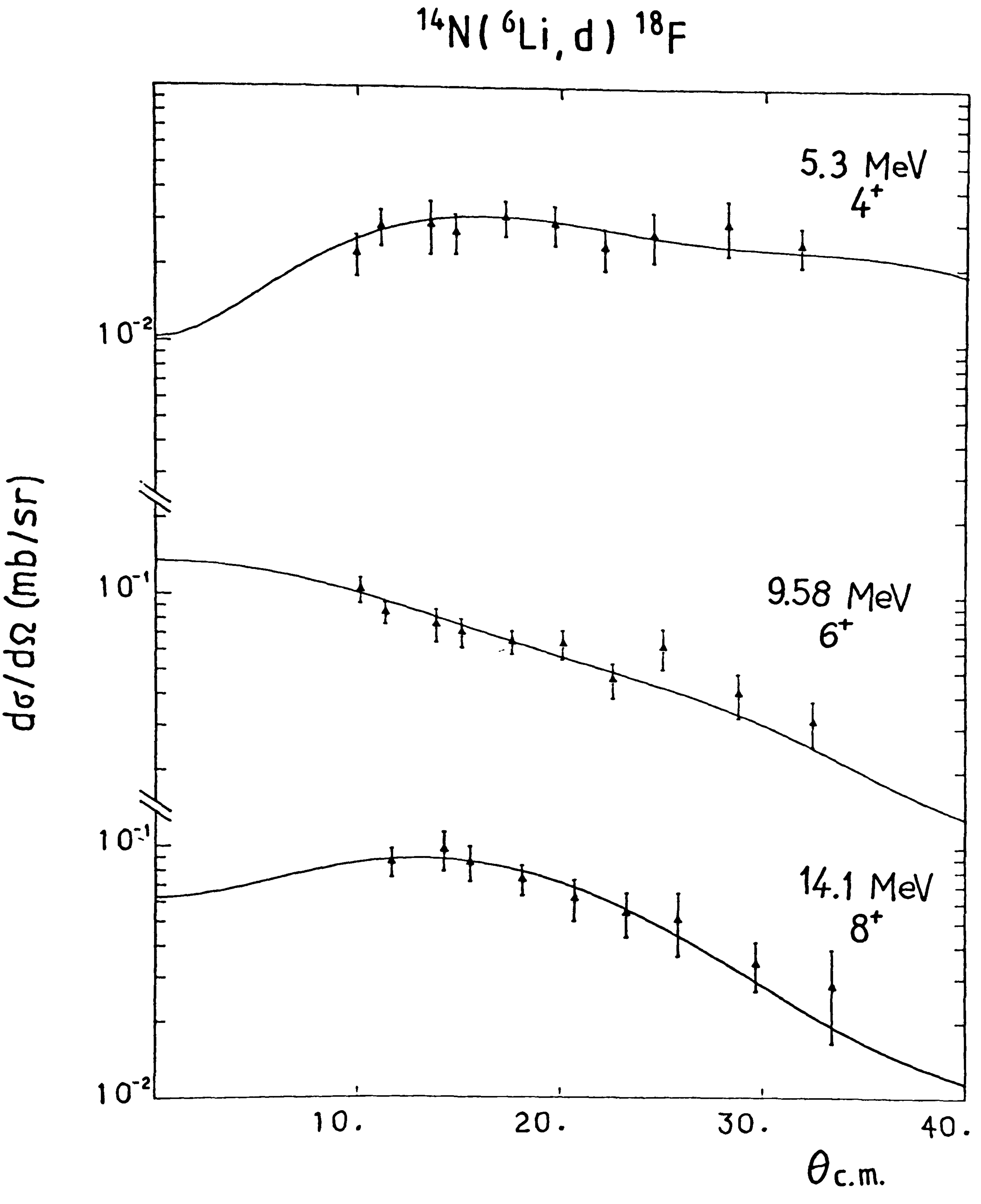

Figure 4.10 $^{14}N(^{6}Li,d)^{18}F$ at 36MeV. Angular distributions for the 5.3MeV 4^+, 9.58MeV 6^+ and 14.1MeV 8^+ states. The solid curves are normalized DWBA predictions.

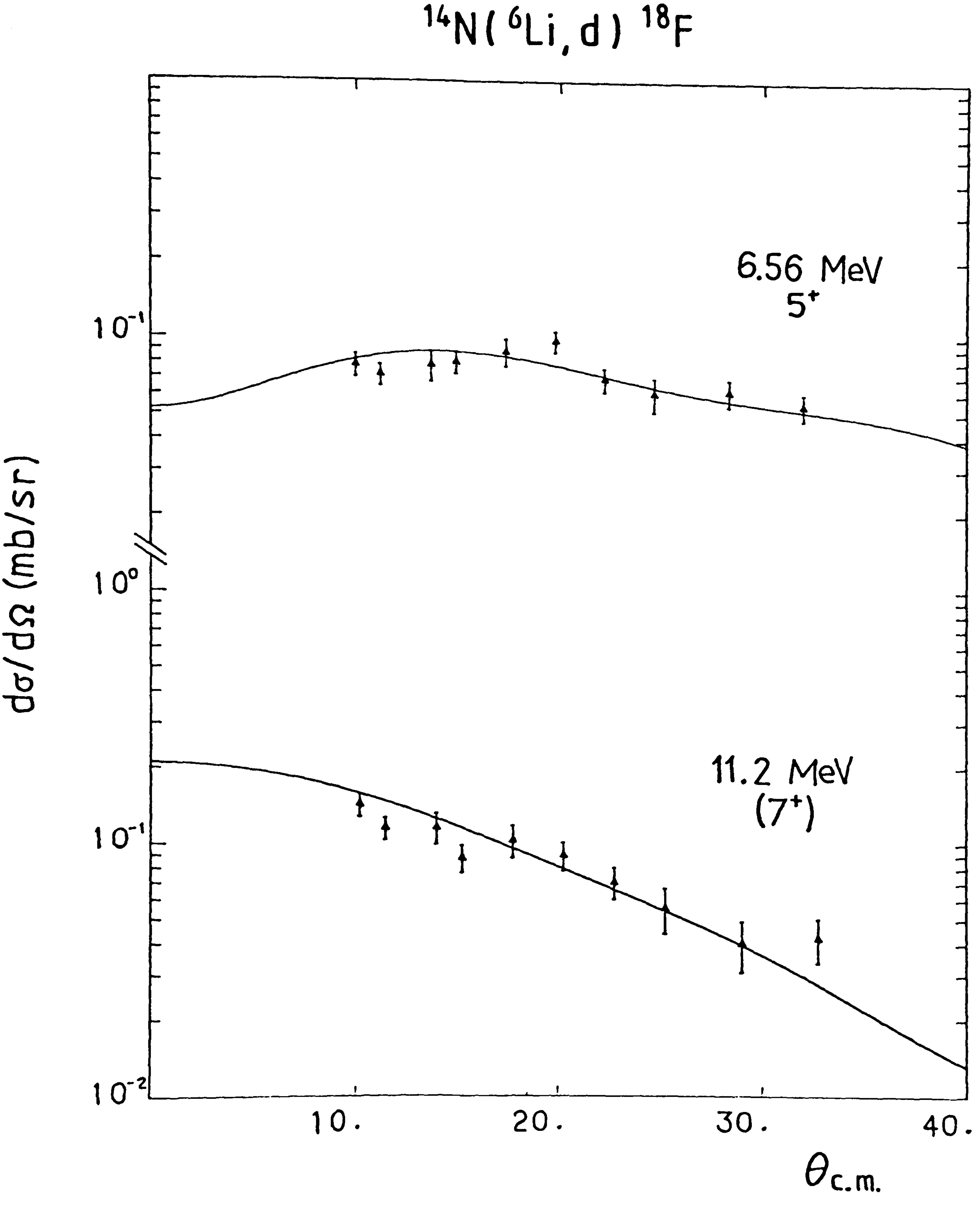

Figure 4.11 $^{14}N(^{6}Li,d)^{18}F$ at 36MeV. Angular distributions for the 6.56MeV 5^+ and 11.2MeV states. The solid curves are normalized DWBA predictions for the final spins shown in the plot.

TABLE 4.6

Normalisation factors and spectroscopic factors for the $^{14}N(^{6}Li,d)^{18}F$ reaction

Ex.E(MeV)	J^{π}	N	L	2N+L	$\mathcal{N}$	S_{DWBA}	S_{theor}	S_{rel}
5.3	4^+	2	4	8	0.164	0.159	0.152	0.147
6.5	5^+	2	4	8	0.272	0.263	0.196	0.190
		1	6	8			0.54E-4	
9.58	6^+	1	6	8	0.190	0.184	0.204	0.198
11.2	(7^+)	1	6	8	0.172	0.167	0.232	0.225
		0	8	8			0.28E-3	
14.1	8^+	0	8	8	0.268	0.260	0.268	0.260

$\mathcal{N}$ is the ratio of the experimental cross section to the DWBA calculations

$S_{DWBA} = \mathcal{N}/(C_p^2\ S_p\ C_R^2)$

where S_p is the calculated spectroscopic factor for $^{6}Li = 1.032$

and C_p and C_R are the isospin Clebsch-Gordan coefficients for the projectile and residual nucleus respectively.

S_{rel} = relative theoretical spectroscopic factor normalised to the 8^+ state.

estimation showed particular strength for the low L values (Table 4.5) and as far as agreement in shape and normalisation, our data seems to confirm the predictions. Figure 4.12 shows the theoretical calculations for the different intervening L values, superimposed on the experimental data, as well as the normalisation coefficients required for the best fit, out of a χ^2 test.

The relative agreement found between spectroscopic strengths for the analysed states, is consistent with identifying them as members of the same rotational band. Despite of the small discrepancies found in the comparison of the spectroscopic factors for the odd spin states, it is believed that they are not inconsistent with a direct alpha transfer mechanism and with their identification as members of the 1^+ band.

Considering the light system, for the ^{6}Li projectile the angular momentum coupling allows relative L values 0, 1 and 2; only the L=0 state will have importance as shown in previous sections, and no appreciable contribution to incoherent addition of cross sections will be introduced by the projectile system.

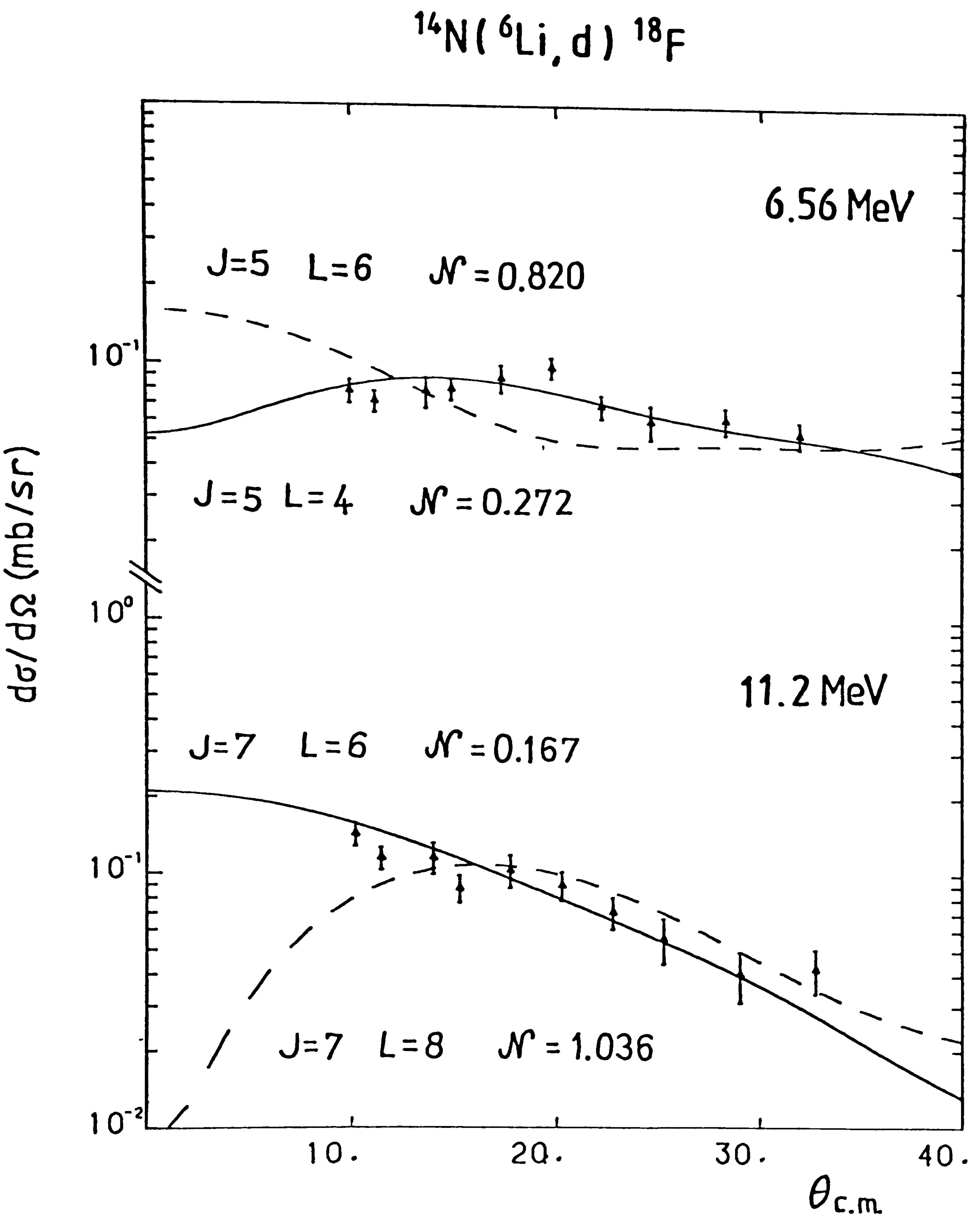

Figure 4.12 $^{14}N(^{6}Li,d)^{18}F$ at 36MeV. Angular distributions for the 6.56MeV 5^+ and 11.2MeV states. Solid and dashed curves show the theoretical DWBA predictions for different L value contributions.

4.7 Conclusions

From the comparison between the DWBA calculations and the experimental data, the states strongly populated in the four nucleon transfer reaction on ^{14}N may be seen as resulting from a direct cluster transfer mechanism. Prior and post agreement was obtained. The even spin states showed to be in accordance with theoretical predictions in both magnitude and shape, and, as a result of the analysis of relative spectroscopic factors, should be regarded as members of the same rotational band. The DWBA study for the 9.58 and 14.1 MeV states complements the spin assignments performed in Chapter 3. Cross section for the odd spin states seems to be fairly well described by DWBA calculations as far as shape is concern, and despite some small discrepancies in the spectroscopic factors, the direct transfer analysis appears to be successful. Despite the fact that no spin assignment has been made for the 11.2 MeV state, the data are consistent with the $J^{\pi}=7^{+}$ assignment .

It can be concluded that a fairly good description of the structure of the analysed states, as well as the reaction mechanism involved has been completed.

CHAPTER 5

Three Particle Transfer Reactions on ^{14}N

5.1 Introduction

The highly selective behaviour of (^{6}Li,^{3}He) and (^{6}Li,t) has been observed by different authors [BIN71, MAR78, CUN81a] since studies showing substantial ^{3}He + t clustering in the ^{6}Li ground state [YOU70] attracted interest on three nucleon transfer reactions induced by ^{6}Li ions. Ignoring Coulomb and binding energy effects, (^{6}Li,^{3}He) and (^{6}Li,t) are expected to be similar, and consequently mirror states in the final nuclei are supposed to be populated in a rather similar way. Bingham et al. [BIN71] found this feature clearly in the ^{14}N(^{6}Li,t)^{17}F and ^{14}N(^{6}Li,^{3}He)^{17}O reactions with an 18 MeV ^{6}Li beam. Large cross sections were observed for the 3.85 MeV and the 5.22 MeV levels in both residual nuclei, and these strong transitions seemed to proceed via a direct three-nucleon transfer mechanism. The same reaction performed at a higher bombarding energy of 46 MeV [MAR78] showed a predominant excitation of three mirror states in mass 17: 8.4 MeV, 10.7 MeV and 14.8 MeV. By analogy with the pattern of the strong three particle transfers observed in mass 19 (^{19}Ne and ^{19}F), the author suggested spin and parity assigments of $11/2^+$ and $15/2^+$ for the 10.7 MeV and 14.8 MeV states, which with the already known $7/2^+$ at 8.4 MeV would probably be the L=2, 4 and 6 members of the 3 particles-2 holes (3p-2h) cluster rotational band in ^{17}O and ^{17}F. In this thesis work the same reaction on ^{14}N but at 36 MeV of ^{6}Li beam showed very similar triton and ^{3}He spectra and a high degree of selectivity. The 10.7 MeV and 14.8 MeV peaks predominate by far and some excitation is found on levels at 7.47 MeV, 8.4 MeV, 12.0 MeV and 13.5 MeV. Theoretical angular correlations for α-decay were obtained for the different plausible final spins showing a fairly structureless result. In accord with the theoretical expectation, the experimental angular correlations showed no strong structure and therefore no spin assignment was possible in this fashion. Nevertheless, the study of the displacement of the symmetry axis of the decay pattern allowed to establish some preferences for final spin assignment.

Shell model spectroscopic factors were obtained and several DWBA analyses were performed for some suggested spin assignment. Relative normalization factors have been compared.

5.2 The $^{14}N(^{6}Li,t)^{17}F$ and $^{14}N(^{6}Li,^{3}He)^{17}O$ Reactions

Several three particle transfer reactions into mass 17 induced by ^{6}Li beams at bombarding energies ranging from 18 MeV to 46 MeV have been performed recently [BIN73 ,MAR78 ,CUN81a]. The strong selectivity observed even at 18 MeV of incident ^{6}Li suggests a predominantly direct reaction mechanism. In $^{14}C(^{6}Li,t)^{17}O$ at 34 MeV of ^{6}Li, Cunsolo et al. [CUN81a] performed very complete Hauser and Feshbach calculations, based in the very weakly populated 5.22 MeV state, assuming its spin and parity to be $9/2^{-}$. The theoretical prediction for this state showed good agreement with the measured angular distributions. Further tests on the goodness of the parameters chosen were performed with the $^{14}C(^{6}Li,^{6}He)^{14}N$ reaction at the same incident energy. The final Hauser Feshbach calculations showed, that the strongly populated states in $^{14}C(^{6}Li,t)^{17}O$ have not a significant contribution (at most 10%) of the compound nucleus mechanism. Therefore, our study of mass 17 was carried out within the framework of the DWBA formalism.

The reaction studied, leading to states in ^{17}F and ^{17}O, showed significant excitation of states between 8.4 MeV and 14.86 MeV. Within this range of excitation energies, both nuclei can either proton or alpha decay. Table 5.1 shows binding energies and Q-values for the relevant particle decays in ^{17}F and ^{17}O. Although the higher excited state (14.86 MeV) could decay by deuteron emission (the deuteron binding energy being approximately 14 MeV) no such a process is expected to be recorded because of the low energy of the ejected deuterons.

TABLE 5.1

Q-values for the three particle transfer reactions.

Binding energies in mass 17 nuclei

Reaction	^{14}N(^{6}Li,t)^{17}F	^{14}N(^{6}Li,^{3}He)^{17}O
Q-value	0.0491 MeV	2.8293 MeV

Nucleus	^{17}F	^{17}O
p-binding energy	-0.6004 MeV	-13.7805 MeV
α-binding energy	-5.8189 MeV	-6.3599 MeV
t-binding energy	-21.0066 MeV	-18.6233 MeV
^{3}He-binding energy	-15.8431 MeV	-18.7611 MeV
d-binding energy	-14.0396 MeV	-14.0473 MeV
n-binding energy	-16.8123 MeV	-4.1420 MeV

A three particle cluster orbiting around a ^{14}N, 1^+ core to form states in mass 17, can have a maximum of three total angular momentum values resulting from the coupling of the three nucleon cluster to the 1^+ spin of the core. These values as well as the cluster orbital angular momentum values are displayed in Table 5.2 for several final spins in mass 17. All the latter states will have positive parity consistently with a s-d cluster wave function. It is seen that for most of the recoil nucleus spins, three cluster total angular momenta have to be included in order to either predict the angular distribution or the angular correlation. On the other hand, the α particle from the decay of the recoil nucleus will only have one posible angular momentum. These latter values are tabulated in Table 5.2 for α decay processes to either ^{13}N or ^{13}C, ground states. This is a very important feature for the angular correlation calculation, because there is going to be only one decay matrix $S^{I'}_{s'',l''}$ (Appendix A) which can therefore be treated as an overall normalization.

The decay from ^{17}O can take place through an alpha emission (ground state binding energy of -6.35 MeV), a neutron emission (-4.142 MeV) or through a proton emission (-13.78 MeV). Alpha decays to excited states in ^{13}C can also occur. As mentioned in chapter two, the decay particles are identified by their kinematical behaviour. Fig. 5.1a) shows the kinematical behaviour of α-particle and proton decays from the 14.88 MeV state leading to ^{13}C ground state, excited 3.089 MeV, 3.684 MeV and 3.854 MeV levels and to ^{16}N ground state, respectively. The α-decay to ^{13}C ground state has very distinct energies from the other possible candidates and its corresponding peak can be clearly identified. The

TABLE 5.2

Three particle cluster states in mass 17 nuclei

Recoil nucleus spin & parity	J_c	L_c	L_α
$1/2^+$	1/2	0	1
	3/2	2	
	1/2	0	
$3/2^+$	3/2	2	1
	5/2	2	
	3/2	2	
$5/2^+$	5/2	2	3
	7/2	4	
	5/2	2	
$7/2^+$	7/2	4	3
	9/2	4	
	7/2	4	
$9/2^+$	9/2	4	5
	11/2	6	
	9/2	4	
$11/2^+$	11/2	6	5
	13/2	6	
$13/2^+$	11/2	6	7
	13/2	6	
$15/2^+$	13/2	6	7

J_c = total angular momentum of the cluster.

L_c = relative orbital momentum of the cluster.

L_α = relative orbital momentum of the alpha particle.

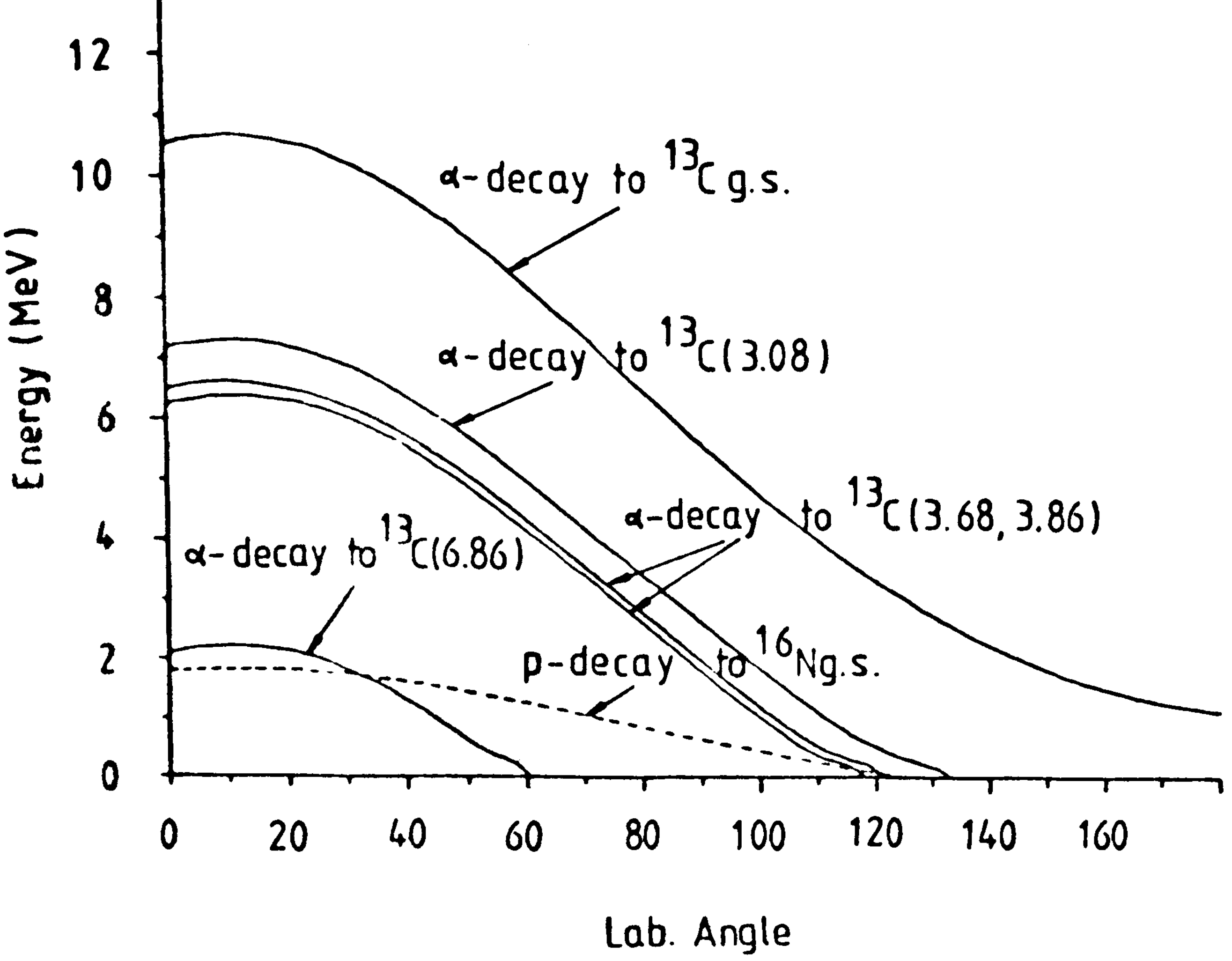

Figure 5.1a) Kinematics for different decay particles from the 14.88MeV state in ^{17}O when the ^{3}He from the ^{14}N(^{6}Li,^{3}He)^{17}F* reaction is detected at 10° in the laboratory system.

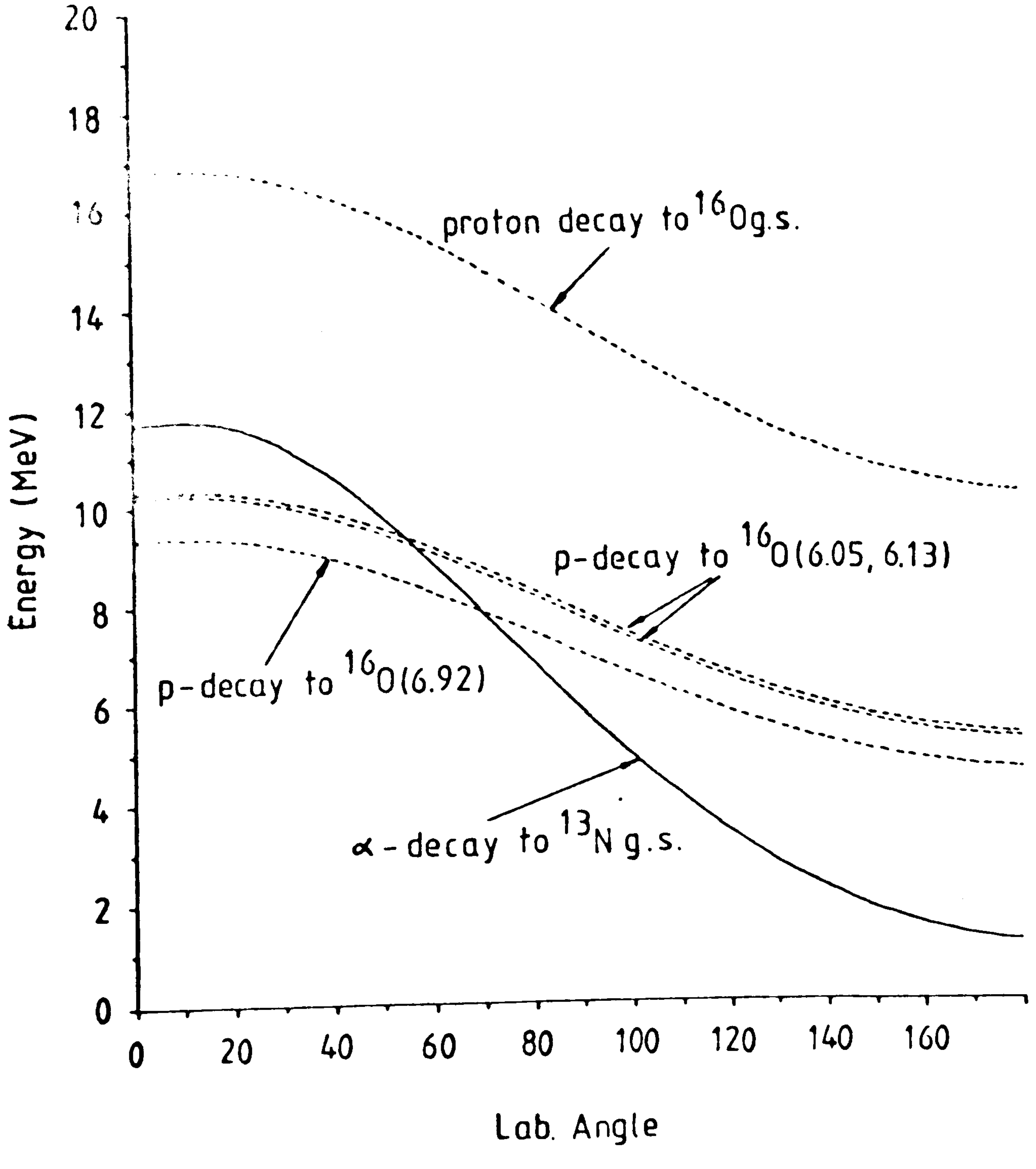

Figure 5.1b) Kinematics for different decay particles from the 14.88MeV state in ^{17}F when the triton from the ^{14}N(^{6}Li,t)^{17}F* reaction is detected at 10° in the laboratory system.

proton decay, on the other hand, presents a crossing point with the α-decay leading to the 6.86 MeV excited state in ^{13}C, and this has to be carefully considered. The other mass 17 nucleus of interest, ^{17}F, has a proton binding energy of -0.60 MeV and an alpha binding energy of -5.82MeV (for all residual nuclei in their ground state) and again possible excited states in ^{16}O and ^{13}N have to be taken into account for kinematical identification. Fig. 5.1b) shows α and proton kinematical behaviours for the decay fo the 14.84 MeV state in ^{17}F. Particle emissions leading to ^{13}N ground state and ^{16}O ground state and 6.05 MeV, 6.13 MeV and 6.92 MeV excited levels have to be considered under the actual experimental conditions. Obviously proton decays to the 6.05 MeV and 6.13 MeV states in ^{16}O would not be resolved by the experiment. No interference between the proton decay to ^{16}O ground state and the alpha decay is present. The crossing point at ~ 55° and ~ 70° will not hinder the particle identification because of the laboratory angles at which we measured.

5.3 The Experiment: Angular Distributions and Angular Correlations

The experimental set up and working conditions, the data processing technique and analysis were described in chapters 2, 3 and 4. The particle identification spectrum (PI) allowed us to obtain triton and ^{3}He spectra by setting up windows in the ^{3}H and ^{3}He groups respectively. Typical spectra for these two particle groups are shown in figs. 5.2 and 5.3. Two states show a striking strength in both cases, the 10.7 and 14.8 MeV excited states. Four other states follow in importance at 7.4, 8.4, 12.0 and 13.5 MeV. The 7.47 MeV state which is clearly seen in the triton spectrum, is found to be a broad peak in the ^{14}N(^{6}Li,^{3}He)^{17}O reaction, probably due to an admixture of unresolved states. The reactions have an overall energy resolution of approximately 220 KeV. The data obtained for the already mentioned states at different angles of detection are shown and compared to theoretical DWBA calculations in following sections. In addition to the window in the PI spectrum, coincidence requirements with the side detectors were imposed for the angular correlation analyses. The coincidence counting rate was lower than that observed for ^{18}F. Typical single and coincidence spectra for triton and ^{3}He are shown in figs. 5.4 and 5.5. The most highly populated states can be clearly observed in the coincidence spectra, where the 10.7 MeV and 14.8 MeV levels predominate. Proton and α decays were observed from ^{17}O and ^{17}F excited states which showed as for ^{18}F a predominance for the α emission. Decay to the first excited states of some of the resultant residual nuclei (^{13}C, ^{16}O) were also recorded. Percentages for the different decays are shown in tables 5.3a) and 5.3b)

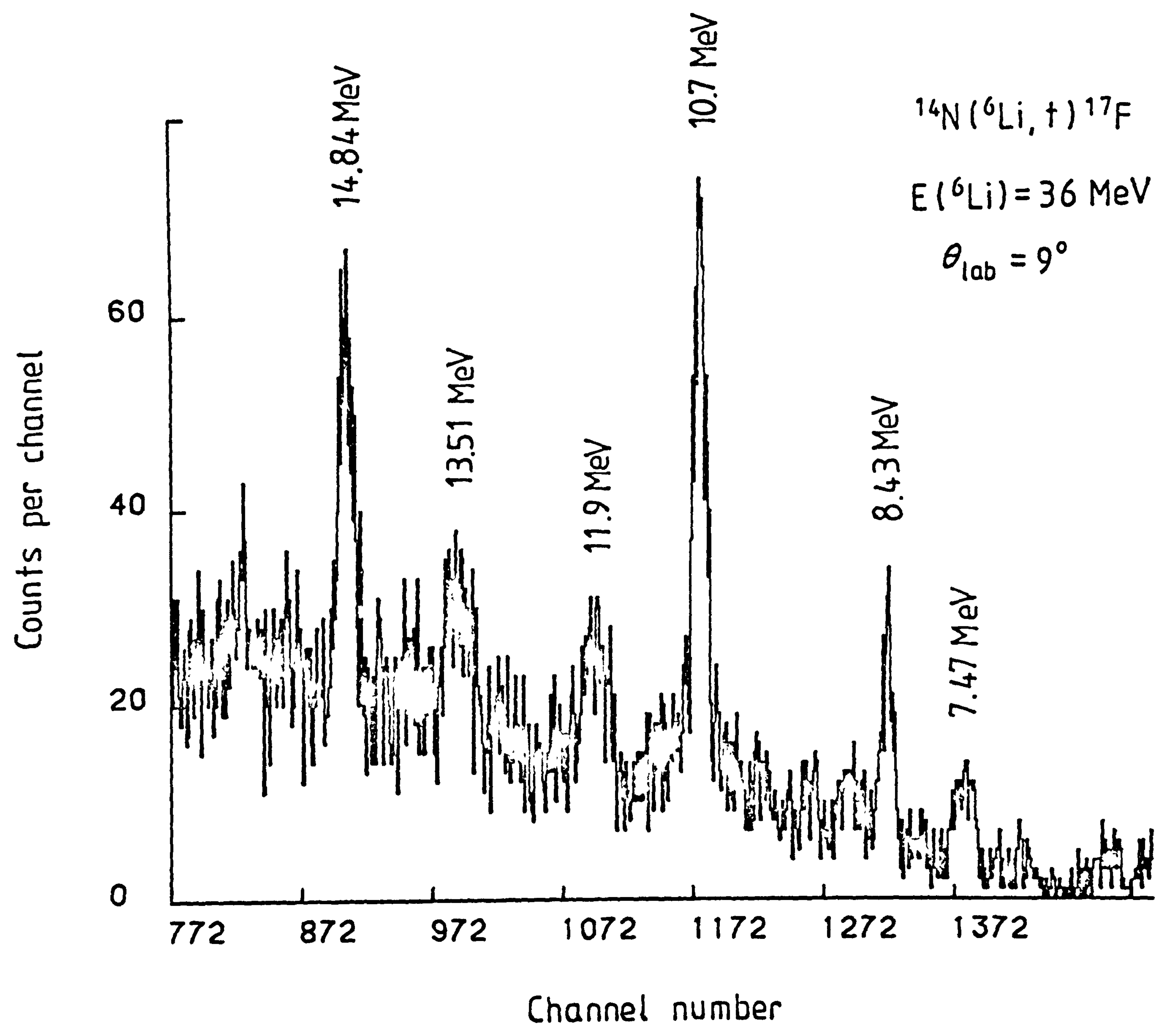

Figure 5.2 Triton energy spectrum for the $^{14}N(^6Li,t)^{17}F$ reaction at 36MeV and $\theta_{lab}=9^{\circ}$

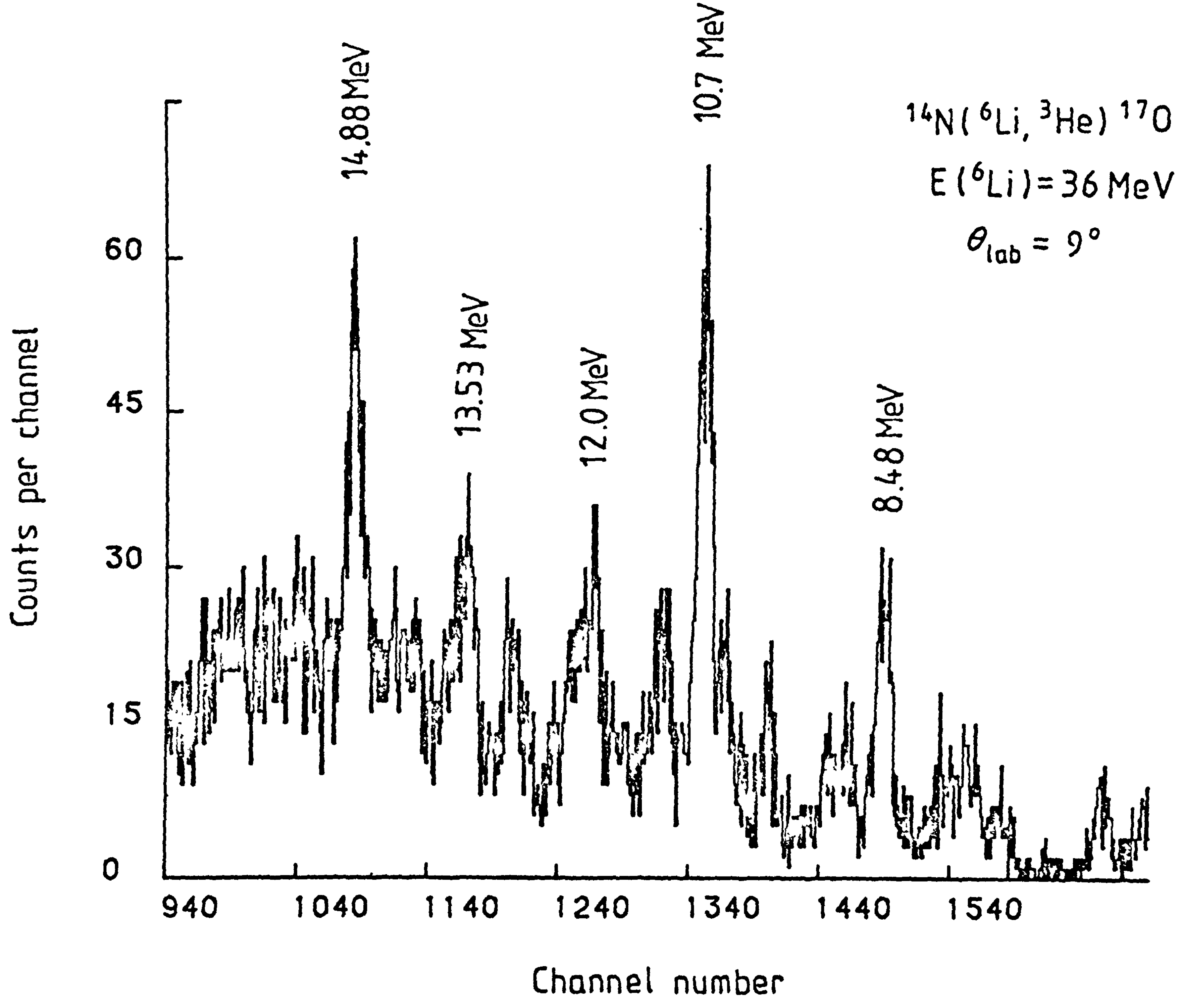

Figure 5.3 ^{3}He energy spectrum for the $^{14}N(^{6}Li, ^{3}He)^{17}O$ reaction at 36MeV and $\theta_{lab}=9^{o}$

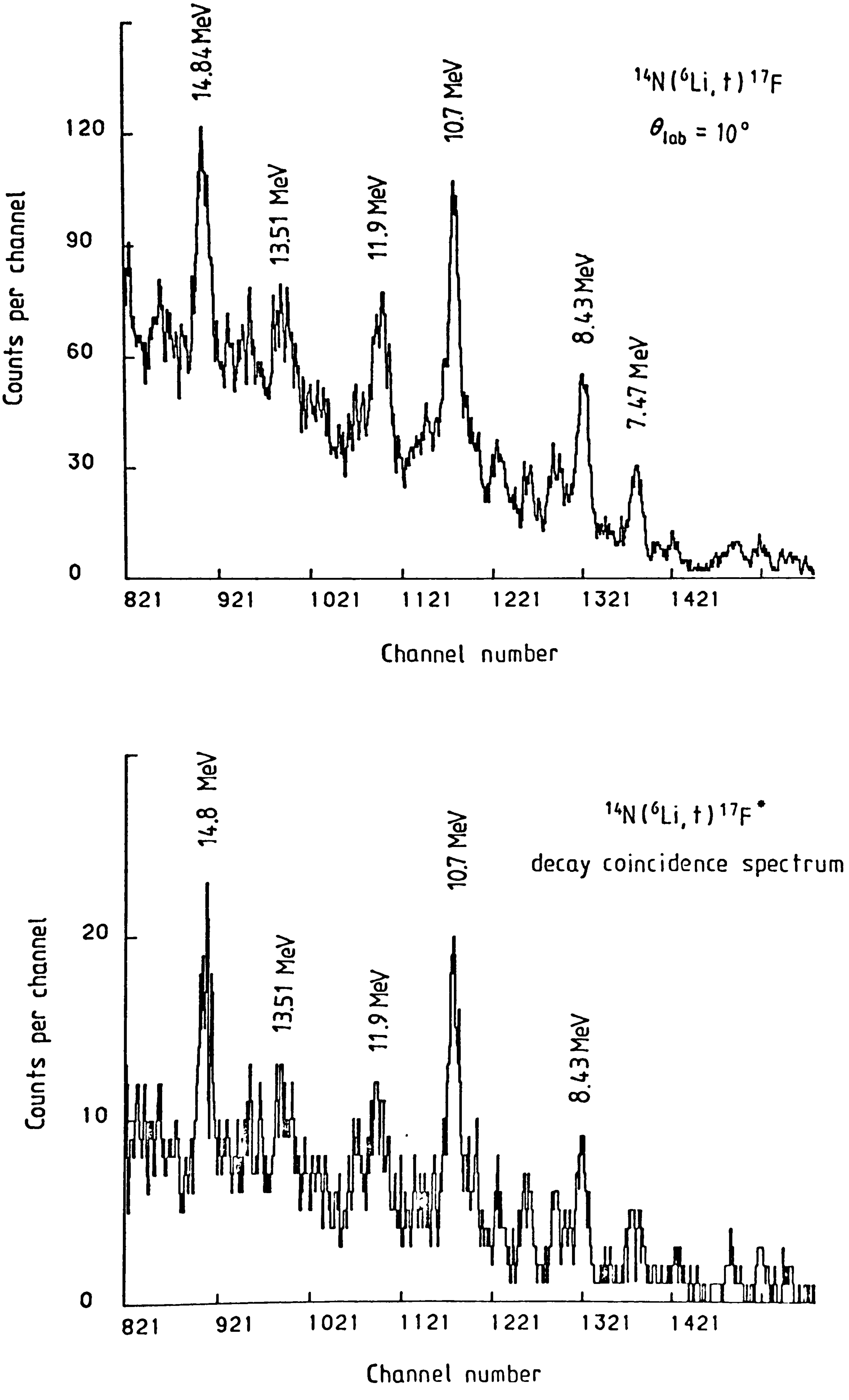

Figure 5.4 Single and coincidence spectra for ^{17}F

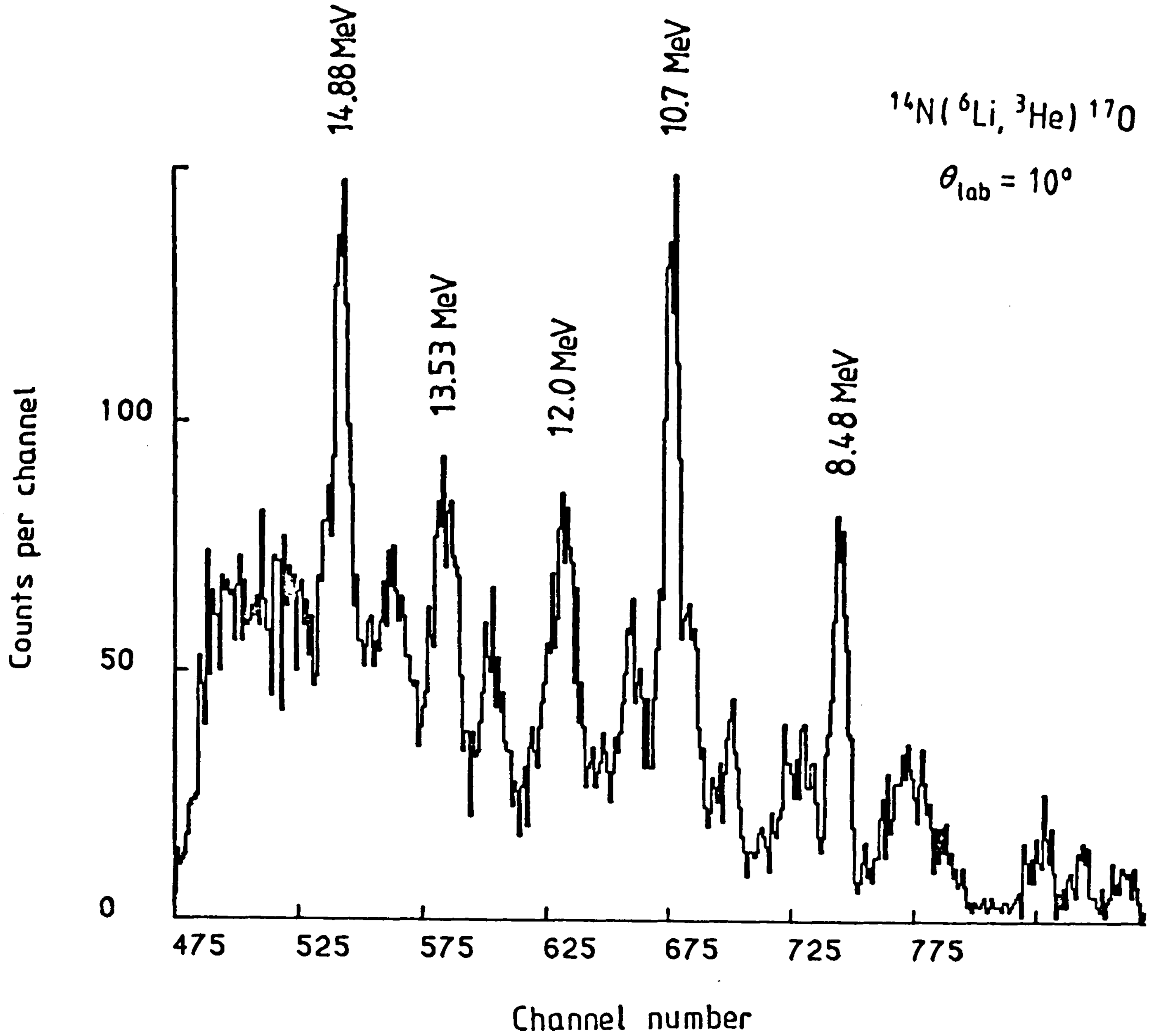

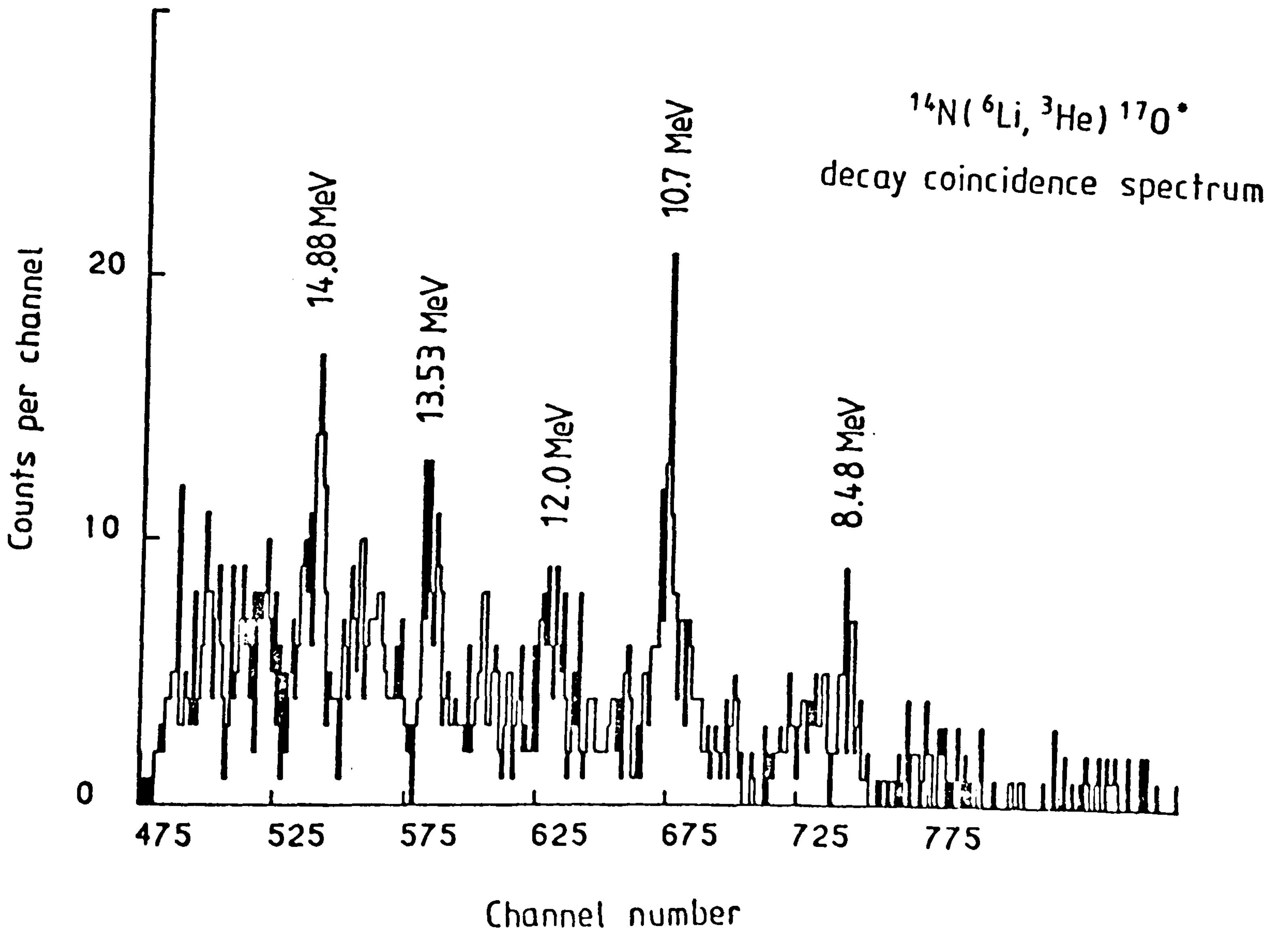

Figure 5.5 Single and coincidence spectra for ^{17}O

TABLE 5.3 a)

Particle decay in ^{17}F

Nucleus	State	α-decay	p-decay	% p-decay to g.s.	% p-decay to 6.05
^{17}F	10.7	69% ± 9	31% ± 7	67 %	33 %
	11.9	66% ± 10	34% ± 7	83 %	17 %
	13.51	70% ± 10	30% ± 7	85 %	15 %
	14.84	65% ± 9	35% ± 7	88 %	12 %

TABLE 5.3 b)

Particle decay in ^{17}O

Nucleus	State	p-decay	α-decay	% α-decay to g.s.	% α-decay to 3.08	% α-decay to 3.6,3.8
^{17}O	10.7	-	100 %	98 %	2 %	-
	12.0	-	100 %	92 %	6 %	2 %
	13.53	-	100 %	91 %	6 %	3 %
	14.88	6% ± 2	94% ± 8	66 %	18 %	16 %

where, as done for the ^{18}F decay in chapter 3, the decays are averaged over the ten angles measured. It can be seen that for ^{17}F, the intensity of the proton decay leading to the 6.05 MeV excited state in ^{16}O decreases as the excitation energies in ^{17}F increase, and that no α-decay leading to excited states in ^{13}N is observed. Alpha decay to ^{13}N, ground state predominates over proton decay although the latter shows a much favourable binding energy (-0.60 MeV) than the former (-5.82 MeV). Kinematical effects for the decays from ^{17}O have to be considered. Alpha decays to excited states in ^{13}C (3.08, 3.68, 3.85 and 3.86 MeV) will lead at some detection angles to emerging α-particles of very low kinetic energy after leaving the gas cell, preventing them to pass the electronic circuit lower level discriminators. Proton decay is only observed for the 14.85 MeV state in ^{17}O (proton binding energy of -13.78 MeV) and its detection at backward angles is hindered by the electronics. Typical decay spectra in coincidence with the 14.8 MeV state in ^{17}F and ^{17}O are shown in figs. 5.6a) and 5.6b) respectively, where peaks corresponding to α-particles and protons leading to ground and excited states in the residual nuclei have been identified.

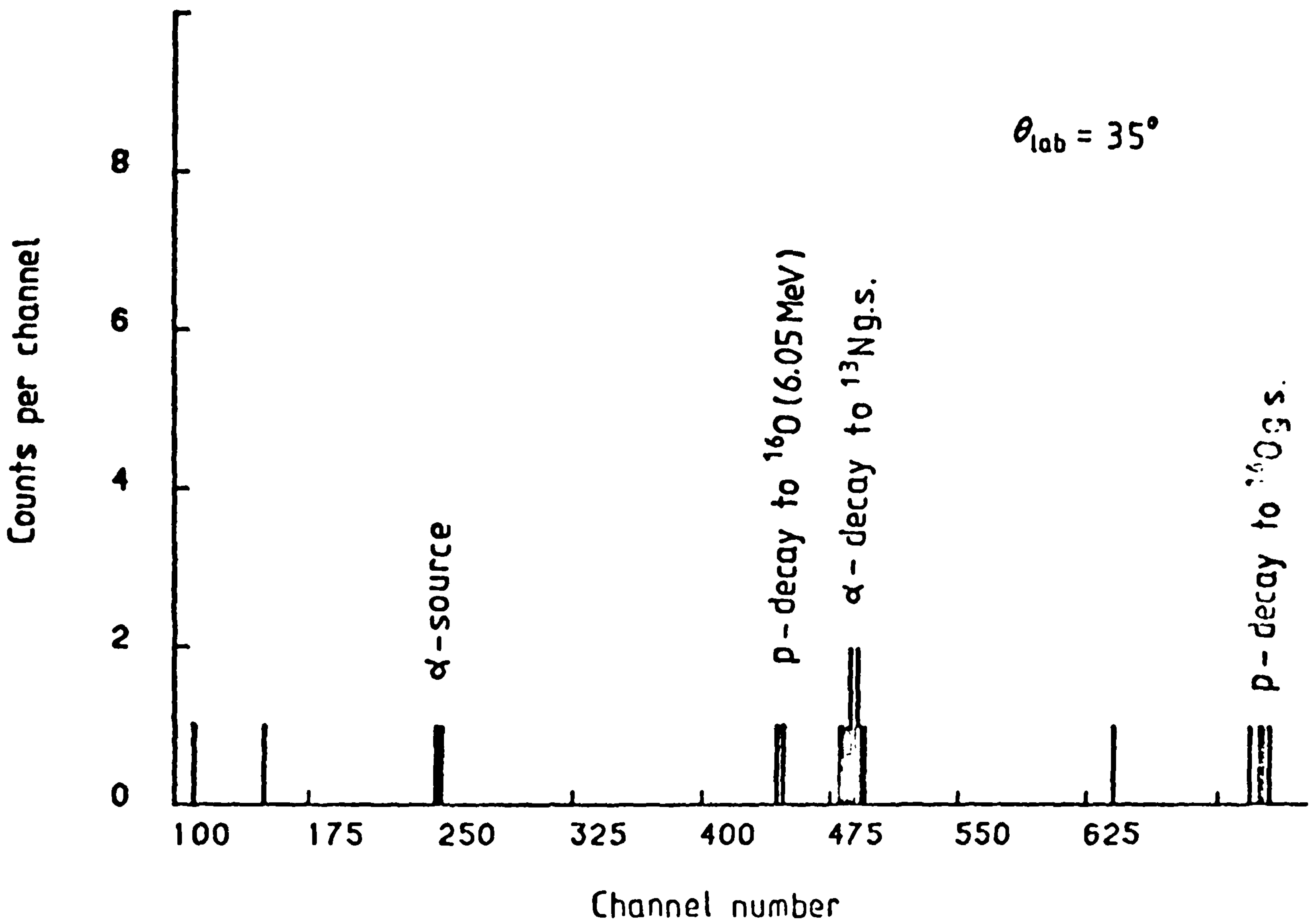

Figure 5.6a) Decay spectrum for the 14.84MeV state in ^{17}F

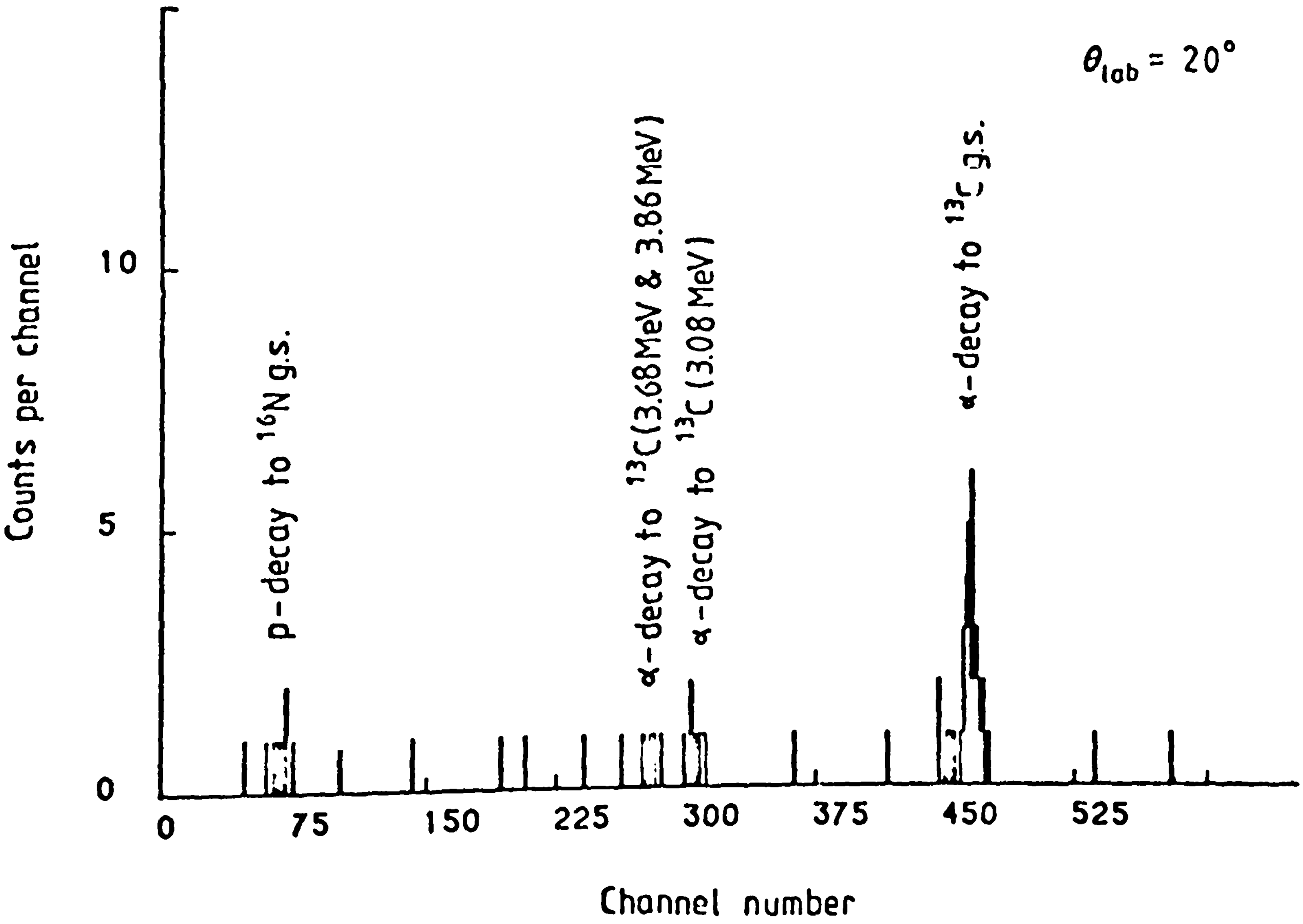

Figure 5.6b) Decay spectrum for the 14.88MeV state in ^{17}O

5.4 DWBA Analysis

As the angular correlation analysis for ^{17}F and ^{17}O decays did not show an oscillatory shape characteristic of the spin of the parent nuclei, shell model calculations were performed in an effort to find some guidance in assigning spins to some states. DWBA cross section would then be predicted in order to compare them with the experimental cross sections as a further test of the spins suggested. Mass 17 positive parity states shell model wave functions, ranging from $1/2^+$ to $15/2^+$, were computed with a model space consisting in the p1/2, d5/2 and s1/2 orbits around a ^{12}C inert core and using the Reehal-Wildenthal two body interaction [REE73]. The SU3 interaction was used to generate three-particle cluster spectroscopic amplitudes. Clear preference (i.e, large spectroscopic factors) was found for some $7/2^+$, $9/2^+$, $11/2^+$, $13/2^+$ and $15/2^+$ levels. Comparisons with the highly selective spectra (see fig.5.7) allowed preliminary spin assignments. It is also noted that our spins suggestions are in agreement with those proposed by Martz [MAR78]. Table 5.4 shows the parentage amplitudes found and the contribution of 3p-2h configurations for each state.

DWBA analyses were performed on the basis of these spin assignments. The optical potentials used are displayed in table 4.1. For the entrance channel (pot. 2) the optical potential was obtained by fitting elastic scattering data obtained during the runs. For the exit channel (pot. 4) an optical potential from the literature [ROO65] was employed. The theoretical predictions obtained with the above mentioned potentials and those obtained with the optical potential parameters

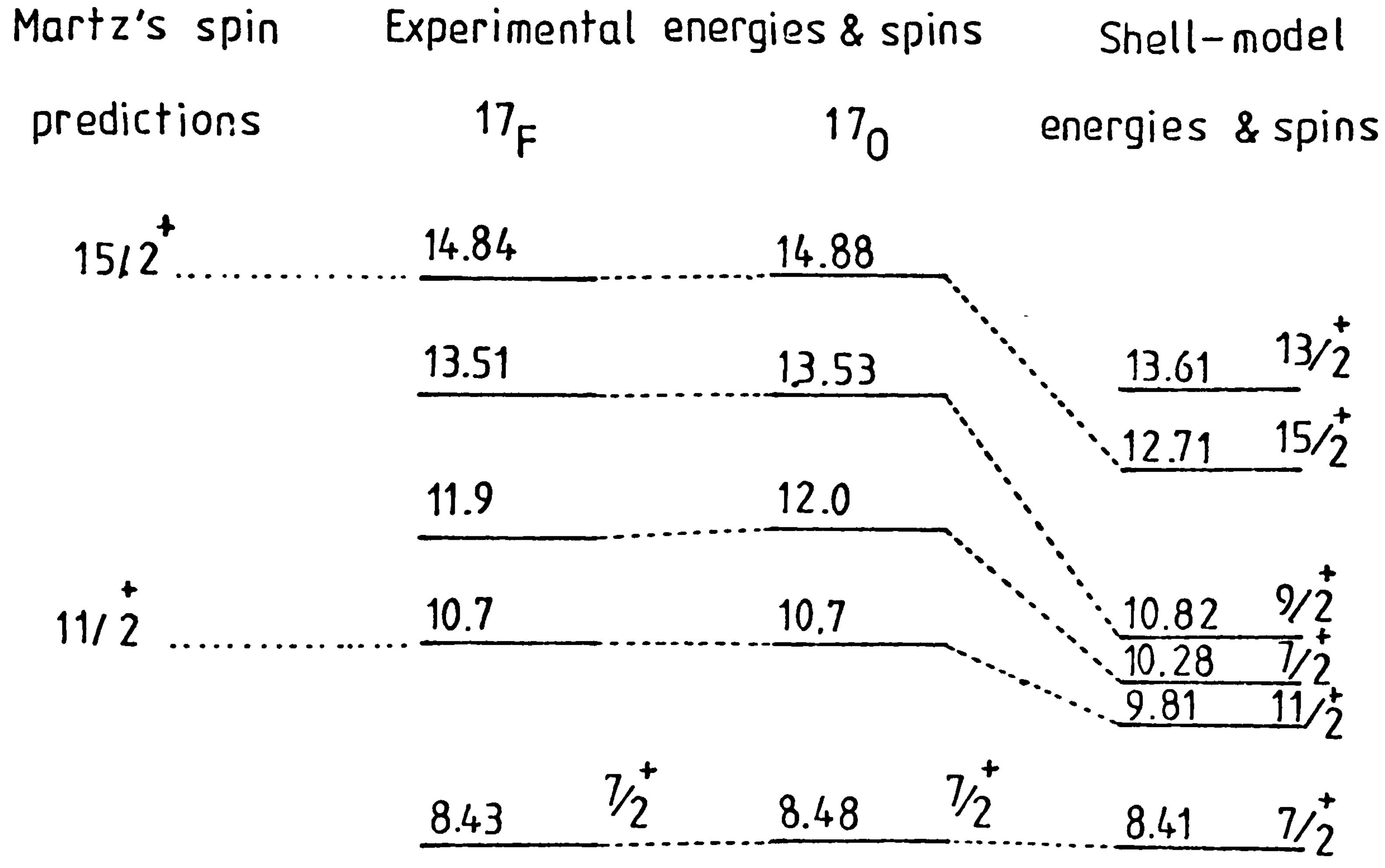

Figure 5.7 Experimental energy levels and theoretical predictions for positive parity states in ^{17}F and ^{17}O.

TABLE 5.4

Three nucleon parentage amplitudes for $\lambda\ \mu(6,0)$ transfer on mass 17 nuclei

Mass 17 state	Ex.E(MeV) (theoretical)	Ex.E(MeV) (exp)		% of 3p-2h	J_c	REWIL Inter. overlap
		^{17}F	^{17}O			
$7/2^+$	8.409	8.48	8.43	90.6	5/2	-0.7526
					7/2	-0.0032
					9/2	0.0239
$11/2^+$	9.815	10.7	10.7	96.4	9/2	0.8901
					11/2	0.0230
					13/2	-0.0162
$7/2^+$	10.279	11.9	12.0	87.3	5/2	-0.0187
					7/2	-0.0283
					9/2	0.7544
$9/2^+$	10.822	13.51	13.53	80.7	7/2	0.1339
					9/2	0.6938
					11/2	-0.0092
$15/2^+$	12.713	14.84	14.88	97.3	13/2	0.9864

proposed by Glover and Jones for elastic scattering of tritons off ^{16}O [GLO65 ,CUN81a] were compared. Both gave almost identical normalization factors and shapes. Nevertheless, a slightly better fit to the 8.4 MeV state was obtained with potential 4 and therefore, this potential was chosen for the final analyses. The radial bound state wave function in ^{17}F and ^{17}O were generated from a BDV model potential. The parameters R, a and V_{so} were obtained from reference [BUC77]: $r_o = r_{co} = 0.505$ fm, a = 1.3 fm, $V_{so} = 2.5$ MeV and the potential depth was adjusted for each state so as to bind the ^3He (or triton) to the experimental binding energy.

The radial wave functions in the projectile ^6Li were obtained assuming that the ^3He-t relative motion was a pure s-wave, as suggested by Bachelier et al. [BAC68], and the wave function having 1 node. The potential that binds the ^3He and triton together was taken to have a Woods-Saxon shape with the following parameters: $r_{co} = r_o = 1.73$ fm and diffuseness a = 0.45 fm. As usual, the separation energy prescription was used to obtain this radial wave function, the separation energy for the ^3He-t system being -15.79 MeV. These potential parameters are from the literature [THO67] and were obtained from elastic scattering of ^3He-^3He. For most of the states in mass 17, there can be three possible contributions as seen in table 5.2. These three cross section were added incoherently, weighted by the corresponding spectroscopic factors and then compared with the experimental angular distribution, as seen in figs. 5.8 and 5.9. The normalization factors are displayed in table 5.5. Fairly good agreement in shape is found for all the mass 17 states. The analysis of relative normalization factors, on the other

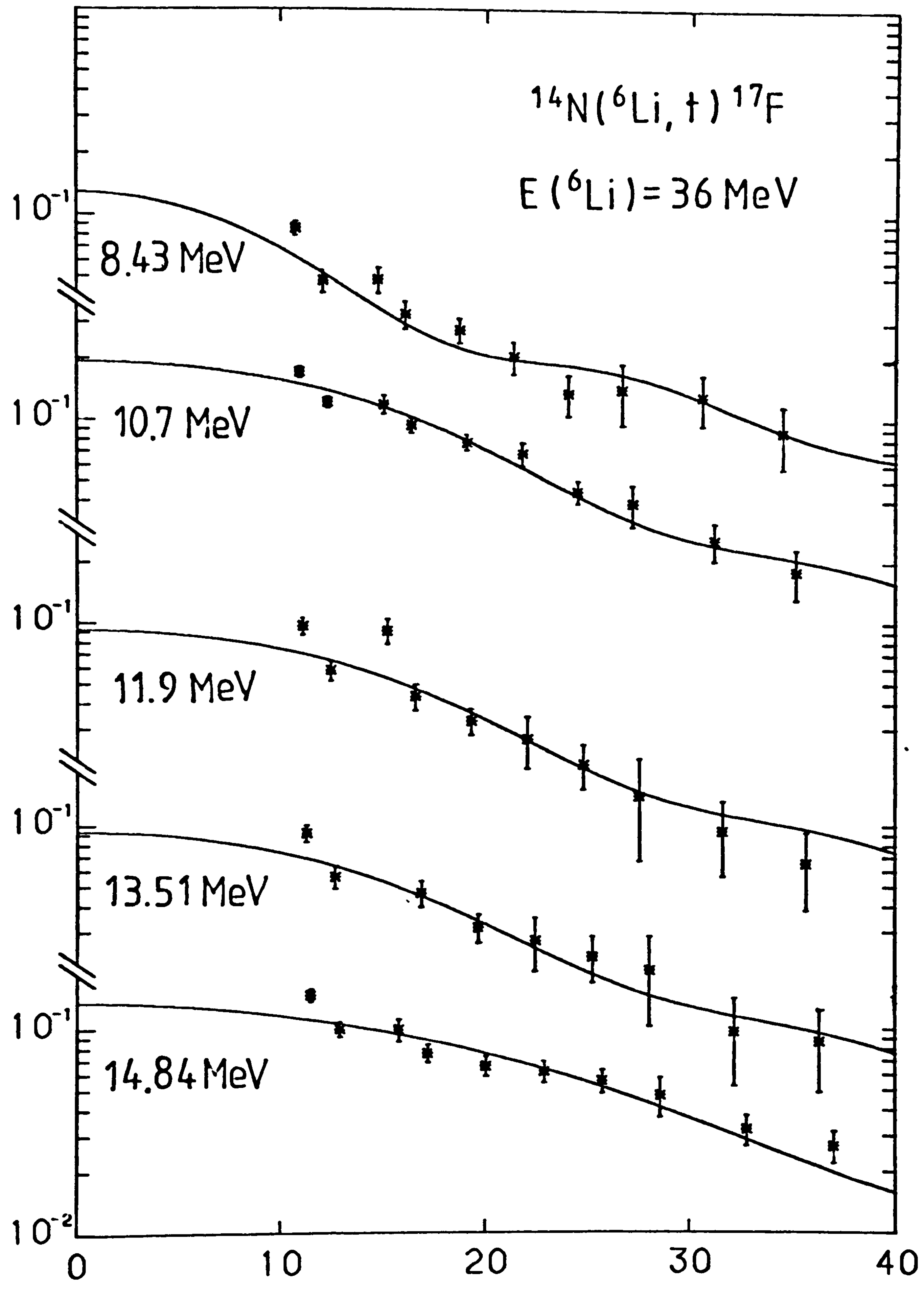

Figure 5.8 $^{14}N(^{6}Li,t)^{17}F$ at 36MeV. Angular distributions for the 8.43MeV $7/2^+$, 10.7MeV $(11/2^+)$, 11.9MeV $(7/2^+)$, 13.51MeV $(9/2^+)$ and 14.84MeV $(15/2^+)$ states. The solid curves are the normalized DWBA predictions.

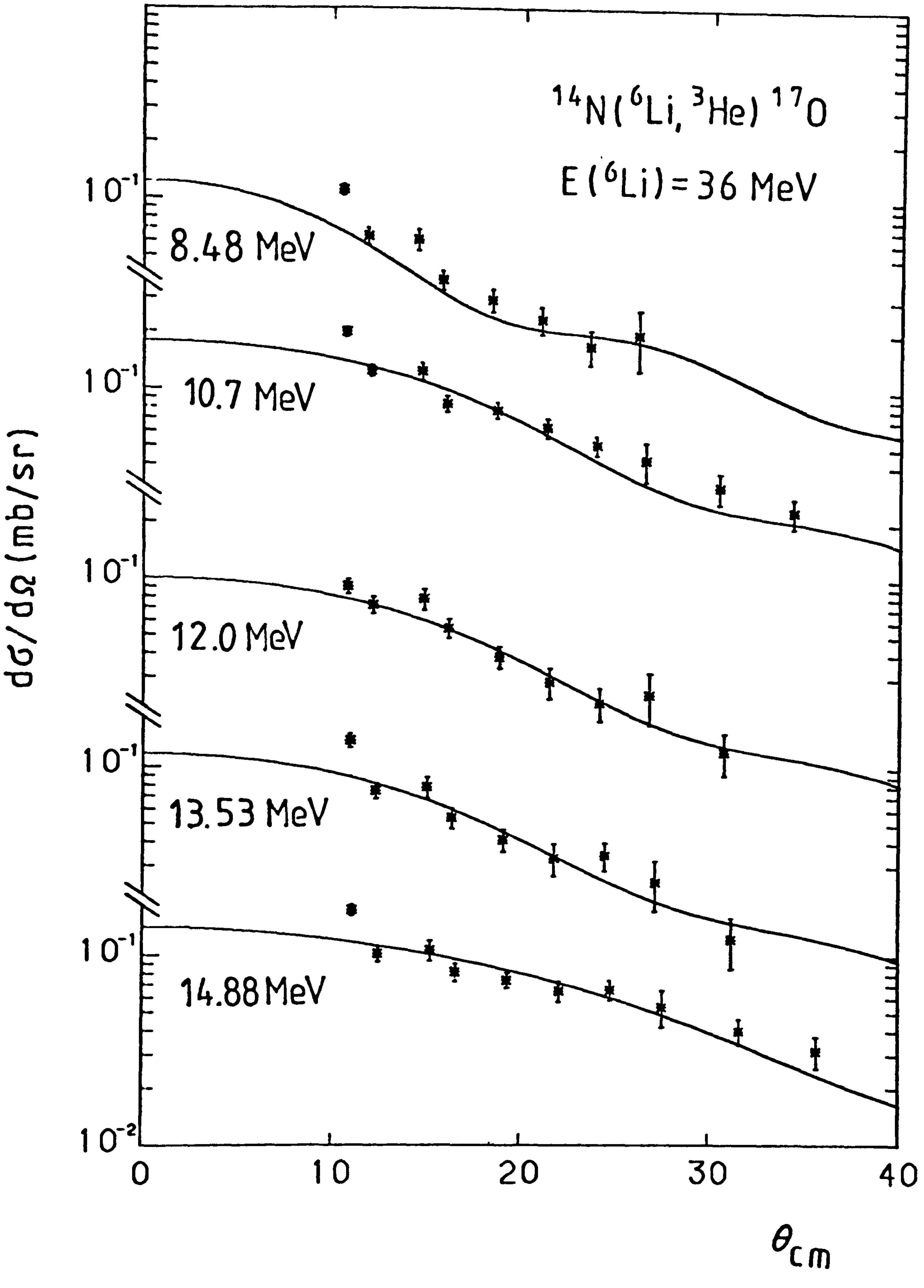

Figure 5.9 ^{14}(^{6}Li,^{3}He)^{17}O at 36 MeV. Angular distributions for the 8.48MeV $7/2^+$, 10.7MeV $(11/2^+)$, 12.0MeV $(7/2^+)$, 13.53MeV $(9/2^+)$ and 14.88MeV $(15/2^+)$ states. The solid curves are the normalized DWBA predictions.

TABLE 5.5

Normalisation factors for the three particle transfer reactions

Residual nucleus	Ex.E(MeV)	J^π	N x 10^2	N_{rel}
^{17}F	8.43	$7/2^+$	1.530	1.812
	10.7	$(11/2^+)$	0.773	0.916
	11.9	$(7/2^+)$	0.779	0.923
	13.51	$(9/2^+)$	0.844	1.0
	14.84	$(15/2^+)$	0.821	0.973
^{17}O	8.48	$7/2^+$	1.502	1.716
	10.7	$(11/2^+)$	0.776	0.886
	12.0	$(7/2^+)$	0.824	0.942
	13.53	$(9/2^+)$	0.875	1.0
	14.88	$(15/2^+)$	0.938	1.072

N = ratio of experimental cross section to DWBA calculations. For the theoretical estimations, all factors except the parentage amplitudes for the projectile system have been included.

N_{rel} = relative N-factors normalised to the 13.5 MeV state.

hand, shows that for both ^{17}F and ^{17}O, the four highest energy states give relative values in agreement with each other within 8.5% and 11%, respectively. The 8.4 MeV state does not give such an striking agreement and the normalization factor differs by factors of 1.81 (^{17}F) and 1.72 (^{17}O). Nevertheless, this sort of disagreement is commonly found even in one particle transfer reactions and it is believed that the results suggest that the spin assignments, spectroscopic amplitudes and the direct three particle transfer mechanism are consistent with the experimental data. It is nevertheless emphasised that the present spin assignments are, as already mentioned, preliminary in nature. In particular, the cross sections obtained for cases in which the relative orbital angular momentum of the cluster is the same, are very similar, thus reducing the confidence in the spin assignments.

5.5 Angular Correlations and Conclusions

Although fairly structureless angular correlations were found both theoretically as well as experimentally, some information can be drawn by following the displacement of the angular correlation symmetry axis. In all the mass 17 experimental data, the very low statistics for the coincidence events introduced large errors which at a time allowed good χ^2 fittings for many angular correlations, and no valuable χ^2 analysis could be performed, but it is interesting to observe if the spin predictions for the mass 17 states give a reasonable agreement between the theoretical and experimental angular correlations. This study would add completeness to the identifications which have been suggested. In fig. 5.10 calculated and experimental angular correlations are shown. Normalization factors have been chosen to give the best fits. The theoretical calculations for the angular correlations displayed, involved the use of the parentage amplitudes obtained from the shell model for each (L_c,S_c,J_c) set. The overall experimental data are well described by the theoretical angular correlations and the different symmetry axis displacements are fairly well represented.

It is concluded that both the DWBA and angular correlation analyses support the spin and state identifications made, although no definite assignment is made. Agreement with the predictions made by Martz [MAR78] of 8.4 MeV, 10.7 MeV and 14.8 MeV energy levels as $7/2^+$, $11/2^+$ and $15/2^+$ representing the L_c = 2,4 and 6 members of a 3p-2h rotational band, is clearly found.

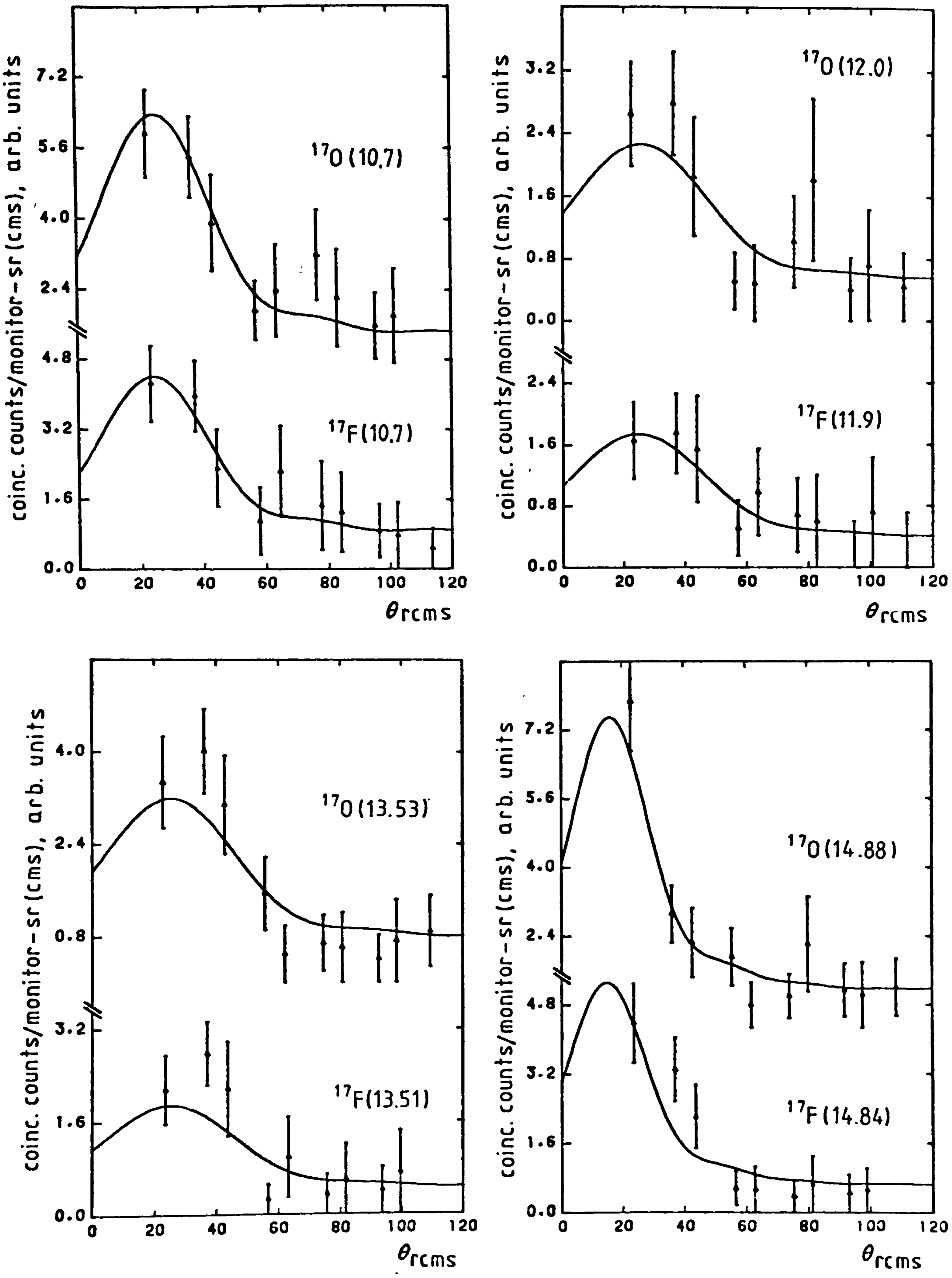

Figure 5.10 Theoretical and experimental angular correlations for ^{17}O and ^{17}F states. The theoretical predictions have been calculated with the spins and parentage amplitudes shown in Table 5.4.

Predominant contributions of 5/2 (L_c = 2), 9/2 (L_c = 4) and 13/2 (L_c = 6) are obtained for the states at 8.4 MeV, 10.7 MeV and 14.8 MeV, respectively, in accordance with Martz's predictions. Two other tentative spins are suggested ($7/2^+$ for the state at 12.0 MeV and $9/2^+$ for the state at 13.5 MeV) and a description of their probable structure has been given. The DWBA description for the three particle transfers seems to be adequate adding information on the reaction mechanims involved.

CONCLUSIONS

The particle - particle angular correlation analysis free from Litherland's [LIT61] restrictions has been used by many authors as a method for spin determination and reaction mechanism interpretation. Most of the experimental research found in the literature has been restricted to zero-spin targets, and decay reactions leading to zero-spin daughter nuclei. We have found that a remarkable richness of angular correlation structure characteristic of the recoil nucleus spin is also observed when target and daughter nuclei have non-zero spins, and therefore making possible spin determination. The oscillating structure of the angular correlations is preserved when the ejectile from the primary reaction is detected at forward angles, and shows a gradually loss of structure for increasing scattering angles. The displacement of the preferred direction in the angular correlation pattern seems to depend also on the angular momentum of the recoil nucleus, and even for structureless angular correlations, it can be considered as a valuable tool for rejecting or reinforcing spin assignments. The dependence of the angular correlation on the reaction mechanism forwards this method as useful for studying the process involved in the reaction.

For the ^{18}F states populated by α-transfer on ^{14}N, our angular correlation analyses assign $J^{\pi}=6^{+}$ to the 9.58MeV level and $J^{\pi}=8^{+}$ for the 14.1MeV state. These two states seem to be a natural extension of the 4p-2h $K^{\pi}=1^{+}$ band starting at 1.7MeV. The unbound description of these states seems to give good account of the displacement of the preferred direction. On the other hand, the 11.2MeV energy level does not show a (d-α) angular correlation characteristic of its angular momentum. Nevertheless, the χ^2 comparison limits the possible spins and parities to 6^-, 7^+ and 8^-. In addition, the energy dependence on J(J+1) for the rotational $K^\pi=1^+$ band seems to be in accordance with the identification of the 11.2MeV state as the 7^+ member of the band.

A direct cluster transfer process seems to be responsible for the selectivity observed in the population of the recoil nucleus states, and the theoretical angular correlations obtained under this assumption give relatively good agreement with the experimental data. Compound nucleus calculations, on the other hand, show angular distribution contributions of at most 10%, while the DWBA analyses give good account of the experimental cross sections. The spectroscopic factors deduced from the experimental data are in agreement with the shell model predictions and although some deviations are observed for the odd spin states, the direct transfer analysis seems to be successful. The results indicate that the $(sd)^4$ configurations are very important in the description of the states, and that the α-cluster transfer is a good model for this reaction.

For the mass 17 nuclei, the lack of structure in the angular correlations, as well as the complexity in the description of each state (several cluster angular momenta contribute to the final spin) hinder the spin identification. The large statistical errors due to the low counting rate of the experiment, and the inclusion of different angular momenta in the theoretical angular correlation, make impossible the spin assignment based on the displacement of the preferred axis. The spin suggestions for ^{17}F and ^{17}O are based on the results of shell model calculations. The shell model states showing a strong parentage with $(sd)^3$ cluster wave functions have been compared to the experimental results, and the relevant spin suggestions have been made. These suggestions agree with the predictions made by Martz for members of a 3p-2h rotational band (8.4MeV $7/2^+$, 10.7MeV $11/2^+$, 14.8MeV $15/2^+$). In accordance with the shell model estimations, two other spin suggestions are made: $7/2^+$ for the 12.0MeV and $9/2^+$ for the 13.5MeV excited states. The DWBA predictions for the tentative spins show very reasonable agreement with the experimental angular distributions. The normalization factors obtained by the cross section comparisons of the highest states, give certain degree of confidence in the spin suggestions, the calculated spectroscopic factors and the selection of the direct process as the prevalent reaction mechanism. The angular correlation comparisons seem to support the spin suggestions. Nevertheless, it is pointed out that the spin suggestions in mass 17 are tentative in nature and further definite assignments remain to be done.

APPENDIX A

A.1 Radioactive Decay of a Nucleus

Direct reactions as knock-on, stripping, or inelastic scattering can lead to orientation effects in the residual nucleus [TOB61]. When these polarization effects take place, a correlation between the direction of the outgoing ejectile and the direction of the emission of any radiation or particle subsequently emitted by the residual nucleus can be observed. We shall consider here a sequential process in which after a direct transfer reaction, the emission of a particle from the recoil nucleus occurs. The whole process is summarized in fig A.1.1

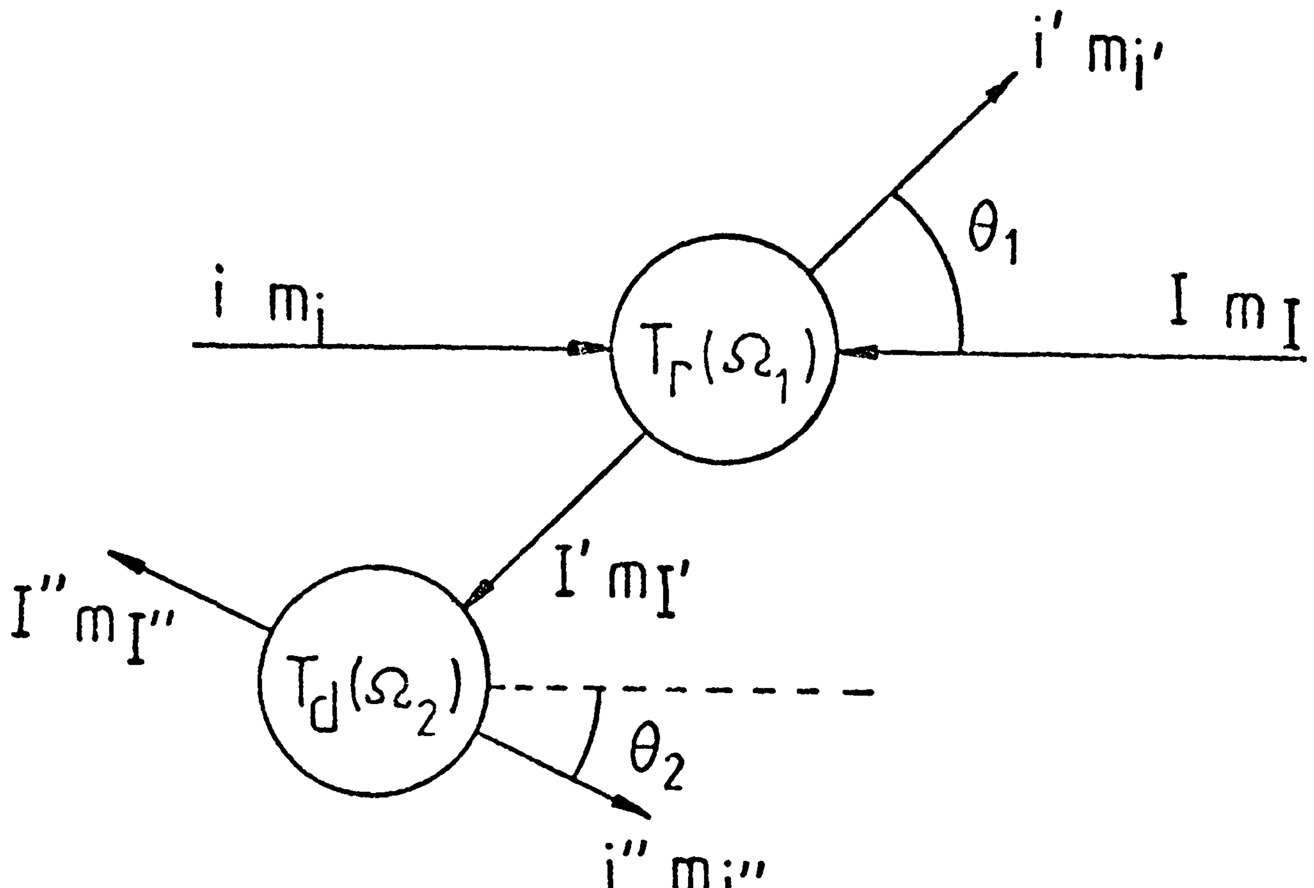

Figure A.1.1 Scheme of a transfer and decay process.

where:

i, m_i are the spin and its z-projection for the incident particle.

I, m_I spin and its z-projection for the target nucleus.

I', $m_{I'}$ spin and its z-projection for the recoil nucleus.

i', $m_{i'}$ spin and its z-projection for the ejectile.

I'', $m_{I''}$ spin and its z-projection for the residual nucleus.

i'', $m_{i''}$ spin and its z-projection for the decay particle.

The scattering angle θ_1 is measured in the total center of mass frame whereas the disintegration angle is measured in the recoil nucleus center of mass frame, and they are both defined relative to the beam direction. Tr and Td identify the transition amplitudes for the transfer and the decay processes respectively. From now on and for the sake of simplicity, only the submagnetic quantum numbers will be explicitly shown in the reaction amplitude $Tr(m_i m_I, m_{i'} m_{I'}; \Omega_1)$ and in the decay amplitude $Td(m_{I'}, m_{i''} m_{I''}; \Omega_2)$. The probability of having the decay particle emerging in the Ω_2 direction after the ejectile has been emitted in the Ω_1 direction will be given by the correlation function $W(\Omega_1,\Omega_2)$:

$$W(\Omega_1,\Omega_2) \propto \sum_{\substack{m_i\, m_I \\ m_{i'}\, m_{i''}\, m_{I''}}} \Big| \sum_{m_{I'}} Tr(m_i m_I, m_{i'} m_{I'}; \Omega_1) \times Td(m_{I'}, m_{i''} m_{I''}; \Omega_2) \Big|^2 \quad \text{(A.1.1)}$$

assuming that the ejectile has no influence on the recoil nucleus disintegration process. Giving the normalization constant N and developing the square of the absolute value in equation (A.1.1):

$$W(\Omega_1,\Omega_2) = N \sum_{\substack{m_i\\ m_I}} \sum_{\substack{m_{i'}\\ m_{i''}\\ m_{I''}}} \Big\{\Big[\sum_{m_{I'}} Tr^*(m_i m_I, m_{i'} m_{I'};\Omega_1) \times Td^*(m_{I'}, m_{i''} m_{I''};\Omega_2)\Big] \times$$

$$\times \Big[\sum_{\bar{m}_{I'}} Tr(m_i m_I, m_{i'}\bar{m}_{I'};\Omega_1) \times Td(\bar{m}_{I'}, m_{i''} m_{I''};\Omega_2)\Big]\Big\} =$$

$$= N\sum\sum\sum\sum_{\substack{m_{I'},\bar{m}_{I'},m_{i''},m_{i'}\\ m_{I''}\, m_i\, m_I}} Tr^*(m_i m_I, m_{i'} m_{I'};\Omega_1) \times Tr(m_i m_I, m_{i'}\bar{m}_{I'};\Omega_1) \times$$

$$\times Td^*(m_{I'}, m_{i''} m_{I''};\Omega_2) \times Td(\bar{m}_{I'}, m_{i''} m_{I''};\Omega_2) \qquad (A.1.2)$$

This form leads to the well known expression in terms of the statistical matrices [TOB61]:

$$W(\Omega_1,\Omega_2) \propto \sum_{\substack{m_{I'}\\ \bar{m}_{I'}}} \rho_{m_{I'},\bar{m}_{I'}}(\Omega_1) \times \rho_{m_{I'},\bar{m}_{I'}}(\Omega_2) \qquad (A.1.3)$$

using the identities:

$$\rho_{m_{I'},\bar{m}_{I'}}(\Omega_2)=\sum_{\substack{m_{i''}\\ m_{I''}}} Td^*(m_{I'}, m_{i''} m_{I''};\Omega_2) \times Td(\bar{m}_{I'}, m_{i''} m_{I''};\Omega_2)$$

$$(A.1.4)$$

$$\rho_{m_{I'},\bar{m}_{I'}}(\Omega_1)=\sum_{\substack{m_i\\ m_I\, m_{i'}}} Tr^*(m_i m_I, m_{i'} m_{I'};\Omega_1) \times Tr(m_i m_I, m_{i'}\bar{m}_{I'};\Omega_1)$$

When studying reactions in which the involved colliding nuclei or their products have intrinsic spins, it is often inconvenient to treat the process in terms of the z-projections of the spins, since these values depend on the choice of the z-direction. Clearly, the dynamics of the collision can not depend on the choice of the coordinate system. It is useful in general to work in the so called channel spin representation for both the transfer and decay processes ilustrated in Figure (A.1.1). The system before the collision will be defined by the type of incoming particles, the channel spin s, and the orbital angular momentum ℓ (in the centre of mass system) [BLA52] and can be summarized in the following scheme:

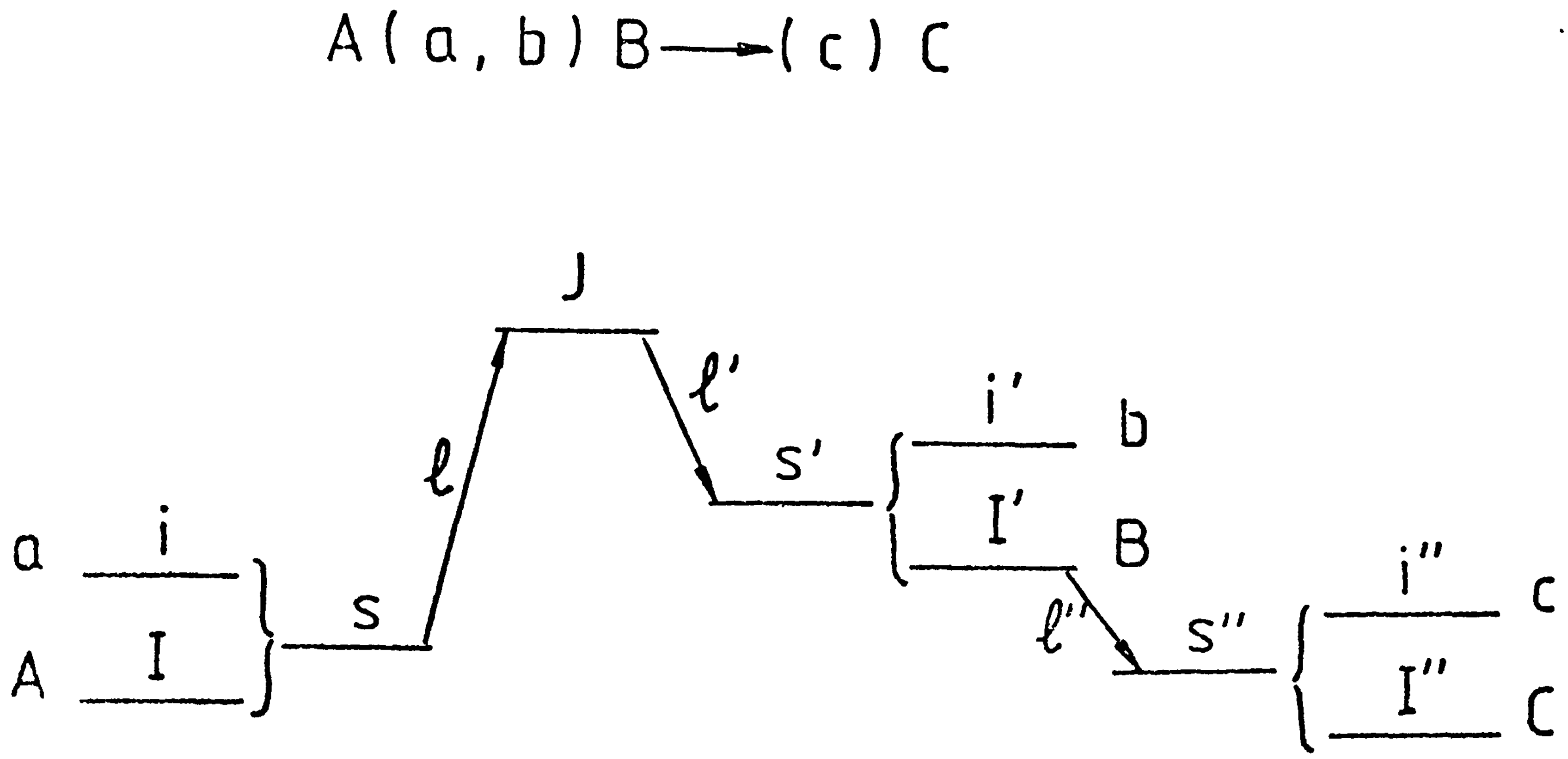

Figure A.1.2 Angular momentum notation for a transfer-decay process in the channel spin representation.

The channel spin s is the total spin in the incident channel, formed by vector addition of the spin of the projectile (i) and the spin of the target (I). This spin s and the relative orbital momentum ℓ add together to give the total angular momentum J of the system. This total J must be preserved in the collision process and as a result of this, the exit channel spin s' (formed by vector addition of spins of the ejectile (i') and recoil nucleus (I')) added to the relative orbital momentum ℓ', give the same total J. A similar channel spin representation is given in figure (A.1.2) for the decay process: the channel spin s" (formed by vector addition of the spins of the decay particle (i") and the residual nucleus (I")) and the relative orbital momentum ℓ'' combine to give the spin of the recoil nucleus (I'). When the phenomenological description of the reaction process is done in the scattering matrix formalism [WIG47, BLA52] a very general treatment is enabled. In this "black box" description only the asymptotic wave functions for the entrance and exit channels are treated explicitly. The relation between these outgoing and incoming waves gives the scattering matrix which contains all the physical information about the process. The asymptotic form of the reaction wave function in the exit channel can be given equivalently in terms of the scattering matrix as well as in terms of the reaction amplitudes, and the relation between the two is given by [BLA52]:

$$\begin{aligned} \mathrm{Tr}(m_i m_I, m_{i'} m_{I'}; \Omega_1) &= \sum_{\substack{s\, s'\, J\, \ell\, \ell' \\ m_s\, m_{s'}\, m_J\, m_{\ell'}}} \sum (2\ell+1)^{\frac{1}{2}} (I i m_I m_i | s m_s) \times (\ell s 0 m_s | J m_J) \times \\ &\times (\ell' s' m_\ell' m_s' | J m_J) \times (I' i' m_{I'} m_{i'} | s' m_s') \times S^J_{s'\ell' s\ell} \times Y^{m_{\ell'}}_{\ell'}(\Omega_1) \end{aligned} \quad \text{(A.1.5)}$$

(where $S^J_{s'\ell' s\ell}$ is given by the mechanism of the reaction). In a similar way Da Silveira [DAS76] treats the decay process in the channel spin representation, expressing the decay amplitude in terms of the disintegration matrix elements $S^{I'}_{s''\ell''}$:

$$\begin{aligned} \mathrm{Td}(m_{I'}, m_{i''} m_{I''}; \Omega_2) &= \sum_{\substack{s''\, \ell'' \\ m_{s''}\, m_{\ell''}}} \sum (I'' i'' m_{I''} m_{i''} | s'' m_{s''}) \times (s'' \ell'' m_{s''} m_{\ell''} | I' m_{I'}) \times \\ &\times S^{I'}_{s''\ell''} \times Y^{m_{\ell''}}_{\ell''}(\Omega_2) \end{aligned} \quad \text{(A.1.6)}$$

A very general expression for the correlation function is obtained replacing the transition amplitudes given above into equation (A.1.1). The $W(\Omega_1,\Omega_2)$ function would then describe behaviours as displacement from zero degrees of the symmetry axis for the decay , and any analysis of particular features like this one could be carried out. For computational reasons, since 'reduced amplitudes' ($\beta^{\ell}_{m_\ell}$) were obtained from DWBA codes, the transition amplitude for the reaction process was replaced by the form given in equation (A.2.5) (Appendix A part 2), resulting the following expression:

$$\begin{aligned} W(\Omega_1,\Omega_2) = N \sum_{\substack{m_i\, m_I \\ m_{i'}\, m_{i''}\, m_{I''}}} \Big| \sum_{m_{I'}} \Big\{ \sum_{\substack{\ell\, s \\ j}} A_{\ell s j} (-1)^{i'-m_{i'}} & (I j m_I m_j \,|\, I' m_{I'}) \times (\ell s m_\ell m_s \,|\, j m_j) \times \\ & \times (i i' m_i , -m_{i'} \,|\, s m_s) \times \beta^{\ell}_{m_\ell}(\theta_1) \Big\} \times \Big\{ \sum_{\substack{\ell''\, s'' \\ m_{\ell''}\, m_{s''}}} (I'' i'' m_{I''} m_{i''} \,|\, s'' m_{s''}) \times \\ & \times (s'' \ell'' m_{s''} m_{\ell''} \,|\, I' m_{I'}) \times S^{I'}_{s''\ell''} \times Y^{m_{\ell''}}_{\ell''}(\theta_2) \Big\} \Big|^2 \end{aligned} \qquad \text{(A.1.7)}$$

with ℓ s and j defined in equation (A.2.2) of Appendix A part 2 and where the sum rules for the z-projections of the spin in the channel spin representation must be verified

$$\begin{aligned} &\text{(a)} \quad m_{i''} + m_{I''} = m_{s''} \\ &\text{(b)} \quad m_{s''} + m_{\ell''} = m_{I''} \\ &\text{(c)} \quad m_{I''} + m_{i''} + m_{\ell''} = m_{I'} \end{aligned} \qquad \text{(A.1.8)}$$

Some authors [PAN74,DaS76] express the angular correlation in terms of the magnetic substate populations of the recoil nucleus for the primary reaction. The magnetic substate population is defined as:

$$P_{m_{I'}}(\theta_1) \propto \sum_{\substack{m_i\, m_{i'} \\ m_I}} |Tr(m_i m_I, m_{i'} m_{I'}; \Omega_1)|^2 \qquad (A.1.9)$$

in terms of the transition amplitudes. A plane wave view is generally adopted. Under this assumption, the interaction in both the initial and the final channels is neglected reducing the problem to the one of having a beam of clusters (to be transferred) impinging on the target along the momentum transfer direction. This simplified view will show an angular correlation with axial symmetry about the recoil direction. The process will present a similar geometry to that studied by Litherland and Ferguson [LIT61] for angular correlation functions at 0 or 180 degrees, where simple relationships between the spin projections will enable equation (A.1.2) to be written as:

$$W(\Omega_1,\Omega_2) = N' \sum_{m_{I'}} P_{m_{I'}}(\theta_1) \sum_{\substack{m_{i''} \\ m_{I''}}} |Td(m_{I'}, m_{i''} m_{I''}; \Omega_2)|^2 \qquad (A.1.10)$$

In this expression $P_{m_{I'}}$ represent the magnetic substate populations in the recoil direction. Inserting expression (A.1.6) for the decay amplitude into equation (A.1.10):

$$W(\Omega_1,\Omega_2) = N' \sum_{\substack{m_{I'} \\ m_{I''}\, m_{i''}}} P_{m_{I'}}(\theta_1) \Big| \sum_{\substack{s''\, \ell'' \\ m_{s''}\, m_{\ell''}}} S^{I'}_{s''\ell''} (I'' i'' m_{I''} m_{i''} | s'' m_{s''}) \times$$

$$\times\ (s'' \ell'' m_{s''} m_{\ell''} | I' m_{I'})\ Y_{\ell''}^{m_{\ell''}}(\Omega_2) \Big|^2 \qquad (A.1.11)$$

It is interesting to compare the angular correlations obtained under these assumptions with those given by the general expression (A.1.7). For that reason, computational programs were developed for both expressions and simultaneous analyses were carried out. The final angular correlations obtained for the two different approaches were similar in shape (with the angular correlations obtained by the simplified analysis shifted in angle), and as the general expression (A.1.7) included features like the displacements from the recoil direction, this was used for the final comparisons.

In the case of the emission of an alpha-particle, $i"=0$, $m_{i"}=0$ and $s" = I" + i" = I"$ ($s"$ unique) then equation (A.1.11) can be written:

$$W(\Omega_1,\Omega_2) = N' \sum_{\substack{m_{I'} \\ m_{I"}}} P_{m_{I'}}(\theta_1) \Big| \sum_{\substack{\ell" m_{\ell"} \\ m_{s"}}} (I"0m_{I"}0|I"m_{s"}) \times$$

$$\times\ (I"\ell"m_{I"}m_{\ell"}|I'm_{I'})\ S^{I'}_{s"\ell"}\ Y^{m_{\ell"}}_{\ell"}(\Omega_2)\Big|^2 \qquad \text{(A.1.12)}$$

The first Clebsch-Gordan in equation (A.1.12) gives a delta function $\delta m_{I"}m_{s"}$ for any $I"$ value, then, the correlation function becomes:

$$W(\Omega_1,\Omega_2) = N' \sum_{\substack{m_{I'} \\ m_{I"}}} P_{m_{I'}}(\theta_1) \Big| \sum_{\substack{\ell" \\ m_{\ell"}}} (I"\ell"m_{I"}m_{\ell"}|I'm_{I'}) \times$$

$$\times\ S^{I'}_{s"\ell"}\ Y^{m_{\ell"}}_{\ell"}(\Omega_2)\Big|^2 \qquad \text{(A.1.13)}$$

This is the expression for the alpha-decay of the state I'. All the different $\ell"$ contributions to the correlation function have to be included through the decay matrix $S^{I'}_{s"\ell"}$. Some particular cases can be derived when $\ell"$ is unique, since the correlation function reduces to:

$$W(\Omega_1,\Omega_2) = N' \ |S^{I'}_{s"\ell"}|^2 \sum_{m_{I'}\, m_{I"}} P_{m_{I'}}(\theta_1) |(I"\ell"m_{I"}m_{\ell"}|I'm_{I'}) \times$$

$$\times\ Y_{\ell''}^{m_{\ell''}}(\Omega_2)\,|^2 \qquad \text{(A.1.14)}$$

For this particular case equation (A.1.14) shows clearly that the decay mechanism (contained in the S-matrix) does not affect the shape of the angular correlation, acting only as part of the normalization coefficient.

A.2 Magnetic Substate Population of the Recoil Nucleus.

As mentioned before (Appendix A, part 1) orientation effects in the recoil nucleus can be expected as result of direct reactions. These polarization effects would be shown if we expressed the population of the different magnetic-substates of the recoil nucleus in terms of the reaction amplitude given by any direct reaction model:

$$P_{m_{I'}}(\theta_1) \propto \sum_{\substack{m_i\, m_I \\ m_{i'}}} |Tr(m_i m_I, m_{i'} m_{I'}; \Omega_1)|^2 \qquad \text{(A.2.1)}$$

The DWBA code "LOLA" was used in our case as source for the intermediate output to feed the reaction amplitudes into a secondary code. "LOLA" was initially developed by De Vries [DeV73], and follows the work by Austern et al. [AUS64] for a DWBA theory which includes recoil. Considering for example a stripping reaction given by: A(a,b)B, where a particle x is transferred from a=b+x (x bound to the core b with orbital angular momentum "ℓ_1") to the core A=B-x (with orbital angular momentum "ℓ_2"), we find that following the spin notation given in Appendix A part 1, the sum rules for the reaction are summarized in:

$$\begin{aligned} \vec{j} &= \vec{I} - \vec{I}' & \vec{\ell} &= \vec{\ell}_1 - \vec{\ell}_2 \\ \vec{s} &= \vec{i} - \vec{i}' & \vec{j} &= \vec{\ell} + \vec{s} \end{aligned} \qquad \text{(A.2.2)}$$

With this notation, the multipole expansion for the matrix element in the reaction amplitude Tr (see Appen. B) leads to a differential cross-section given in terms of the reduced amplitudes $\beta^{\ell}_{m_\ell}(\theta)$ (also called "partial amplitudes").

$$\frac{d\sigma}{d\Omega} = \frac{\mu_\alpha \mu_\beta}{(2\pi\hbar^2)^2} \frac{k_\beta}{k_\alpha} \frac{2I'+1}{2I+1} \sum_{\substack{\ell s \\ j}} \frac{|A_{\ell sj}|^2}{(2i+1)} \sum_{m_\ell} |\beta^\ell_{m_\ell}(\theta)|^2 \qquad \text{(A.2.3)}$$

where $\mu_\alpha(\mu_\beta)$ is the reduced mass in the entrance (exit) channel a,A (b,B) and $A_{\ell sj}$ the spectroscopic coefficient, defined by ([KAM69])

$$A_{\ell sj}=i^\ell(2\ell+1)^{\frac{1}{2}}(2i+1)^{\frac{1}{2}}J\theta_1\theta_2 W(j_1,\ell_1,j_2,\ell_2;s_x,\ell)\,\delta(s,j_1)\,\delta(j,j_2) \qquad \text{(A.2.4)}$$

Here J is the Jacobian of the coordinate transformation, θ_1 and θ_2 the real spectroscopic amplitudes for the cluster x in nuclei a and B respectively, s_x the spin of the transferred cluster, $j_1=\ell_1+s_x$ and $j_2=\ell_2+s_x$, and W the Racah coefficient for the specified quantities. On the other hand, the transition amplitude can be written in terms of $\beta^\ell_{m_\ell}(\theta)$ [TAM74]:

$$\mathrm{Tr}(\theta) = \sum_{\ell s j} (2\ell+1)^{\frac{1}{2}} A_{\ell sj} (-)^{i'-m_{i'}} (Ijm_I m_j | I'm_{I'}) (\ell s m_\ell m_s | j m_j) \times$$

$$\times (ii'm_i(-m_{i'}) | s m_s)\, \beta^\ell_{m_\ell}(\theta) \qquad \text{(A.2.5)}$$

The DWBA program "LOLA" calculates only one set s ℓ j at a time and in the formalism chooses the z-axis along the $\vec{k}_\alpha$ direction, the y axis along $\vec{k}_\alpha \times \vec{k}_\beta$ and θ the angle between $\vec{k}_\alpha$ and $\vec{k}_\beta$ in the center of mass frame. The intermediate outputs $\beta^\ell_{m_\ell}(\theta)$ were obtained from it and fed into another program which calculates the magnetic substate populations. Replacing $\mathrm{Tr}(\theta)$ of equation (A.2.5) into (A.2.1) we have:

$$P_{m_{I'}}(\theta) \propto \sum_{\substack{m_i \\ m_I \\ m_{i'}}} \Big| \sum_{\substack{\ell \\ s \\ j}} (2\ell+1)^{\frac{1}{2}} A_{\ell sj} (-)^{i'-m_{i'}} (Ijm_I m_j | I'm_{I'}) (\ell s m_\ell m_s | j m_j) \times$$

$$\times\ (ii'm_i(-m_{i'})|sm_s)\ \beta^{\ell}_{m_\ell}(\theta)\ |^2 \qquad \text{(A.2.6a)}$$

When only one set ℓ s j intervenes, $P_{m_{I'}}(\theta)$ reduces to:

$$P_{m_{I'}}(\theta) \propto (2\ell+1)|A_{\ell sj}|^2 \sum_{\substack{m_i\, m_I \\ m_{i'}}} |(-)^{i'-m_{i'}}(Ijm_Im_j\ |I'm_{I'})\ (\ell sm_\ell m_s|jm_j)\ \times$$

$$\times\ (ii'm_i(-m_{i'})|sm_s)\ \beta^{\ell}_{m_\ell}(\theta)|^2 \qquad \text{(A.2.6b)}$$

Where clearly, the spectroscopic coefficient will not affect the relative magnetic substate populations, being only a normalization factor and substantially simplifying the problem, since no information on the spectroscopic amplitudes needs to be introduced. Expression (A.2.6a) will give the magnetic substate population of the recoil nucleus in the beam direction and for the centre of mass angle θ; so if we want the $m_{I'}$ populations in the recoil direction for example, a rotation of the coordinate system towards the recoil direction has to be applied. If we obtain a set of axes (x',y',z') by rotating the original set (x,y,z) through a specific R-rotation, then the eigenstates $|J,N_J\rangle'$ of $J_{z'}$ (eigenfunctions of the square of the total angular momentum J^2) are given by rotating the corresponding eigenstates $|J,M_J\rangle$ of J_z with the axis rotation R [BRI67]

$$|J,N_J\rangle' = \sum_{M_J} |J,M_J\rangle D^J_{M_JN_J}(R) \qquad \text{(A.2.7)}$$

For the conjugate states $'\langle J,N_J|$ we have:

$$'\langle J,N_J| = \sum_{M_J} (D^J_{M_JN_J})^* \langle J,M_J| \qquad \text{(A.2.8)}$$

Since we want to express the transition amplitude Tr in the new coordinate system, let us write this distorted wave amplitude in the explicit form of the angular momenta involved:

$$\mathrm{Tr}(m_i m_I, m_{i'} m_{I'}; \Omega_1) = \int d\vec{r}_\alpha \int d\vec{r}_\beta \, \chi_\beta^{(-)*}(\vec{k}_\beta, \vec{r}_\beta) \, (i' m_{i'} I' m_{I'} |V| i m_i I m_I) \times$$

$$\times \chi_\alpha^{(}(\vec{k}_\alpha, \vec{r}_\alpha) \qquad \text{(A.2.9)}$$

where $\chi_\alpha^{(+)}$ and $\chi_\beta^{(-)}$ are the distorted wave functions for the entrance and exit channels respectively, and V is the interaction whose off-diagonal matrix elements are responsible for the transition. If we call μ_J the projections of the J value on the new set of axis, the population of the magnetic substates $\mu_{I'}$, can be written as:

$$P_{m_{I'}}(\theta_1) \propto \sum_{\substack{\mu_i \mu_I \\ \mu_{i'}}} |\mathrm{Tr}(\mu_i \mu_I, \mu_{i'} \mu_{I'}; \Omega_1)|^2 =$$

$$= \sum_{\substack{\mu_i \mu_I \\ \mu_{i'}}} \Big| \sum_{\substack{m_i m_I \\ m_{i'} m_{I'}}} \int d\vec{r}_\alpha \int d\vec{r}_\beta \chi_\beta^{(-)*}(\vec{r}_\beta) \, (D^{i'}_{m_{i'} \mu_{i'}}(R))^* (D^{I'}_{m_{I'} \mu_{I'}}(R))^* \times$$

$$\times \, (i' m_{i'} I' m_{I'} |V| i m_i I m_I) D^{i}_{m_i \mu_i}(R) D^{I}_{m_I \mu_I}(R) \, \chi_\alpha^{(+)}(\vec{r}_\alpha) \Big|^2 =$$

$$= \sum_{\substack{\mu_i \mu_I \\ \mu_{i'}}} \Big\{ \Big[\sum_{\substack{m_i m_I \\ m_{i'} m_{I'}}} \int d\vec{r}_\alpha \int d\vec{r}_\beta \chi_\beta^{(-)*} (D^{i'}_{m_{i'} \mu_{i'}}(R))^* (D^{I'}_{m_{I'} \mu_{I'}}(R))^* \times$$

$$\times \, (i' m_{i'} I' m_{I'} |V| i m_i I m_I) D^{i}_{m_i \mu_i}(R) D^{I}_{m_I \mu_I}(R) \chi_\alpha^{(+)} \Big] \times$$

$$\times \Big[\sum_{\substack{\bar{m}_i \bar{m}_I \\ \bar{m}_{i'} \bar{m}_{I'}}} \int d\vec{r}_{\bar{\alpha}} \int d\vec{r}_{\bar{\beta}} \chi_{\bar{\beta}}^{(-)} D^{i'}_{\bar{m}_{i'} \mu_{i'}}(R) \, D^{I'}_{\bar{m}_{I'} \mu_{I'}}(R) \, (i' \bar{m}_{i'} I' \bar{m}_{I'} |V| i \bar{m}_i I \bar{m}_I)^* \times$$

$$\times \, (D^{i}_{\bar{m}_i \mu_i})^* \, (D^{I}_{\bar{m}_I \mu_I})^* \chi_{\bar{\alpha}}^{(+)*} \Big] \Big\} \qquad \text{(A.2.10)}$$

We can use the sum rule for the D matrices (A.2.11) which will reduce (A.2.10) to a more compact form (A.2.12)

$$\sum_{m'} D^{j}_{m\,m'} (D^{j}_{m''m'})^{*} = \delta m\, m'' \qquad \text{(A.2.11)}$$

$$\sum_{\substack{m_i\, m_I \\ m_{i'}\, m_{I'}\, \bar{m}_{I'}}} \int d\vec{r}_{\alpha} \int d\vec{r}_{\beta} \int d\vec{r}_{\bar{\alpha}} \int d\vec{r}_{\bar{\beta}} \chi^{(-)}_{\bar{\beta}} (\chi^{(-)}_{\beta})^{*} (i'm_{i'} I'm_{I'} |V| im_i Im_I) \times$$

$$\times (i'm_{i'} I'\bar{m}_{I'} |V| im_i Im_I)^{*} (D^{I'}_{m_{I'}\mu_{I'}}(R))^{*} D^{I'}_{\bar{m}_{I'}\mu_{I'}}(R) \chi^{(+)}_{\alpha} (\chi^{(+)}_{\bar{\alpha}})^{*} =$$

$$= \sum_{\substack{m_i\, m_I \\ m_{i'}}} \Big| \sum_{m_{I'}} (D^{I'}_{m_{I'}\mu_{I'}}(R))^{*} \int d\vec{r}_{\alpha} \int d\vec{r}_{\beta} \chi^{(-)*}_{\beta} (i'm_{i'} I'm_{I'} |V| im_i Im_I) \chi^{(+)}_{\alpha} \Big|^{2} =$$

$$= \sum_{\substack{m_i\, m_I \\ m_{i'}}} \Big| \sum_{m_{I'}} (D^{I'}_{m_{I'}\mu_{I'}}(R))^{*} \,\mathrm{Tr}(m_i m_I, m_{i'} m_{I'}; \Omega_1) \Big|^{2} \qquad \text{(A.2.12)}$$

Following Brink's definition for the rotation matrix elements,

$$D^{j}_{mm'}(\alpha,\beta,\gamma) = e^{-im\alpha} d^{j}_{mm'}(\beta)\, e^{-im'\gamma}$$

$$D^{j}_{mm'}(\alpha,\beta,\gamma) = D^{j}_{m'm}(-\gamma,-\beta,-\alpha) \qquad \text{(A.2.13)}$$

$$d^{j}_{mm'}(\beta) = d^{j}_{m'm}(-\beta)$$

and choosing for the rotation R from z ≡ beam direction to z' ≡ recoil direction, a set of Euler angles $\alpha=\gamma=0$ and $\beta=\theta_{recoil}$, we have:

$$P_{\mu_{I'}}(\theta_1) \propto \sum_{\substack{m_i\, m_I \\ m_{i'}}} \Big| \sum_{m_{I'}} d^{I'}_{m_{I'}\mu_{I'}}(\theta_{rec}) \,\mathrm{Tr}(m_i m_I, m_{i'} m_{I'}; \Omega_1) \Big|^{2} \qquad \text{(A.2.14)}$$

In the centre of mass frame $\theta_{rec} = \pi+\theta_1$ which will finally give:

$$P_{\mu_{I'}}(\theta_1) \propto \sum_{\substack{m_i m_I \\ m_{i'}}} \left| \sum_{m_{I'}} d^{I'}_{m_{I'},\mu_{I'}}(\pi+\theta_1)\ \mathrm{Tr}(m_i m_I, m_{i'} m_{I'};\Omega_1) \right|^2 \qquad (A.2.15)$$

A.3 The $S^{I'}_{s''\ell''}$ Decay Matrix

As seen in Appendix A part 1, for evaluating the theoretical expression for the angular correlation (equations (A.1.7) and (A.1.11)) when more than one ℓ'' value intervenes the matrix elements $S^{I'}_{s''\ell''}$ have to be given as input data. It is important then to give a model from which their values could be obtained or at least their range of variation could be estimated. For all alpha decay analyses performed in this thesis, the cluster model picture has been followed, and according to that at most two different ℓ'' values will contribute to the theoretical expression for the angular correlation, as it is the case for certain total angular momentum values in ^{18}F leading to the ground state (1^+) of the daughter nucleus (^{14}N). On the other hand, the alpha emission of high ^{17}F excited states to the ground state ($1/2^-$) of ^{13}N leads to only one ℓ'' contribution for any spin and parity allowed in the parent nucleus. Following the cluster model picture, each of the states in ^{18}F with two allowed ℓ'' may be written as a linear combination:

$$|^{18}\mathrm{F}\ J^{\pi}\ ,T{=}0\rangle = \sum_{\ell''} C^{\alpha}_{\ell''}|^{14}\mathrm{N}\ \ 1^{+}\ ,T{=}0\rangle \otimes |\alpha\ell'' s_{\alpha} J_{\alpha}, T{=}0\rangle \qquad \text{(A.3.1)}$$

of states obtained from coupling the ^{14}N G.S. core to the α-particle orbiting around with certain ℓ'' and J_{α} orbital and total angular momenta. With the restriction of only two ℓ'' contributing, the coefficients of fractional parentage $C^{\alpha}_{\ell''}$ have to satisfy:

$$|C^{\alpha}_{\ell''_1}|^2 + |C^{\alpha}_{\ell''_2}|^2 = 1 \qquad \text{(A.3.2)}$$

These coefficients are closely related to the spectroscopic amplitudes [ANY74, KUR75] through coefficients that depend on the masses of cluster and core, and which are characteristic of the shell where each nucleon of the cluster is transferred.

$$S^{\frac{1}{2}}_{\ell''} = M\, C^{\alpha}_{\ell''} \tag{A.3.3}$$

For each $2N+\ell''$ value considered in the cluster state description this coefficient M is then a constant. On the other hand, following the study of Arima and Yoshida [ARI72] for narrow resonances $\left(\frac{\Gamma_{sp}}{E_{res}} << 1\right)$ a simple expression for the spectroscopic factor can be obtained:

$$S_{\ell''} = \frac{\Gamma^{\alpha}_{res,\ell''}}{\Gamma^{\alpha}_{sp,\ell''}} \tag{A.3.4}$$

Where the spectroscopic factor equals the partial width of the resonance divided by the single particle width of the α-unbound state. This last quantity estimates the width of the state for a particular ℓ''-value and at a specified separation energy, treated as having a pure single particle structure. It is obtained from the imaginary part of the scattering amplitude [ARI72] in potential scattering calculations. In this thesis, the single particle widths are calculated in an analogous manner, from the complex part of the energy eigenvalue in the solution of the Gamow states (Appendix C). A final relation between the coefficients of fractional parentage and the partial width can then be established:

$$(\Gamma^{\alpha}_{res,\ell''})^{\frac{1}{2}} = M\, C^{\alpha}_{\ell''}\, (\Gamma^{\alpha}_{sp,\ell''})^{\frac{1}{2}} \tag{A.3.5}$$

The double differential cross-section for coincidences between the ejectile and the decay particle will be proportional to:

$$\frac{d\sigma(\Omega_1,\Omega_2)}{d\Omega_1\, d\Omega_2} = C\times W(\Omega_1,\Omega_2) \qquad \text{(A.3.6)}$$

the angular correlation defined in Appendix A part 1 as the probability that the alpha particle should emerge in direction Ω_2 after the ejectile (deuteron) has come out in direction Ω_1. On the other hand, if we integrate $\frac{d\sigma(\Omega_1,\Omega_2)}{d\Omega_1\, d\Omega_2}$ over all Ω_1 and Ω_2 values, we will obtain:

$$\int \frac{d\sigma(\Omega_1,\Omega_2)}{d\Omega_1\, d\Omega_2}\, d\Omega_1\, d\Omega_2 = \sigma_1(\text{formation})\, \frac{\Gamma^{\alpha}}{\Gamma_{tot}} \qquad \text{(A.3.7)}$$

the product of the total cross-section for the formation of the state in ^{18}F times the probability for that state to decay by alpha emission, given by the ratio between the alpha decay width over the total decay width of the state. Recalling the most general form of $W(\Omega_1,\Omega_2)$ given in equation (A.1.1),

$$W(\Omega_1,\Omega_2) \propto \sum_{\substack{m_i m_I \\ m_{i'} m_{i''} m_{I''}}} \left| \sum_{m_{I'}} Tr(m_i m_I, m_{i'} m_{I'}; \Omega_1) \times Td(m_{I'}, m_{i''} m_{I''}; \Omega_2) \right|^2 \qquad \text{(A.3.8)}$$

where Tr is the reaction amplitude and Td is expressed in terms of the decay matrix $S^{I'}_{s''\ell''}$,

$$\mathrm{Td}(m_{I'}, m_{i''} m_{I''}; \Omega_2) = \sum_{\substack{\ell'' s'' \\ m_{\ell''} m_{s''}}} (I'' i'' m_{I''} m_{i''} | s'' m_{s''}) \times (s'' \ell'' m_{s''} m_{\ell''} | I' m_{I'}) \times \times S^{I'}_{s'' \ell''} \times Y^{m_{\ell''}}_{\ell''}(\Omega_2) \qquad \text{(A.3.9)}$$

The integral of the double differential cross-section over Ω_1 and Ω_2 can be written as:

$$\sum_{\substack{m_i\, m_I \\ m_{i'}, m_{i''} m_{I''}}} \int d\Omega_1 \Omega_2 \sum_{\substack{m_{I'} \\ \ell'' s'' \\ m_{\ell''} m_{s''}}} \sum_{\substack{\bar{m}_{I'} \\ \bar{\ell}'' \bar{s}'' \\ \bar{m}_{\ell''} \bar{m}_{s''}}} (s'' \ell'' m_{s''} m_{\ell''} | I' m_{I'}) (\bar{s}'' \bar{\ell}'' \bar{m}_{s''} \bar{m}_{\ell''} | I' \bar{m}_{I'}) (I'' i'' m_{I''} m_{i''} | s'' m_{s''}) \times$$

$$(I'' i'' \bar{m}_{I''} \bar{m}_{i''} | \bar{s}'' \bar{m}_{s''}) \; S^{I'}_{\bar{s}'' \ell''} S^{I'}_{s'' \ell''}{}^{*} \; Y^{m_{\ell''}*}_{\ell''}(\Omega_2) \; Y^{\bar{m}_{\ell''}}_{\bar{\ell}''}(\Omega_2) \quad \times$$

$$\mathrm{Tr}^{*}(m_i m_I, m_{i'} m_{I'}; \Omega_1) \; \mathrm{Tr}(m_i m_I, m_{i'} \bar{m}_{I'}; \Omega_1) \qquad \text{(A.3.10)}$$

Making use of the orthogonality property of the spherical harmonics,

$$\int Y^{m_{\ell''}*}_{\ell''}(\Omega_2) \; Y^{\bar{m}_{\ell''}}_{\bar{\ell}''}(\Omega_2) \; d\Omega_2 = \delta_{\ell'', \bar{\ell}''} \times \delta_{m_{\ell''}, \bar{m}_{\ell''}} \qquad \text{(A.3.11)}$$

and considering that for the alpha decay $i''=m_{i''}=0$, the integral can be reduced to:

$$\sum_{\substack{m_i\, m_I \\ m_{i'}, m_{i''} m_{I''}}} \int d\Omega_1 \sum_{\substack{m_{I'} \\ \ell'' s'' \\ m_{\ell''} m_{s''}}} \sum_{\substack{\bar{m}_{I'} \\ \bar{s}'' \\ \bar{m}_{s''}}} (s'' \ell'' m_{s''} m_{\ell''} | I' m_{I'}) (\bar{s}'' \ell'' \bar{m}_{s''} m_{\ell''} | I' \bar{m}_{I'}) \, \delta_{\bar{s}'' I''} \delta_{\bar{m}_{s''} m_{I''}} \times$$

$$\delta_{s'' I''} \delta_{m_{s''} m_{I''}} S^{I'}_{s'' \ell''}{}^{*} S^{I'}_{\bar{s}'' \ell''} \mathrm{Tr}^{*}(m_i m_I, m_{i'} m_{I'}; \Omega_1) \mathrm{Tr}(m_i m_I, m_{i'} \bar{m}_{I'}; \Omega_1) \qquad \text{(A.3.12)}$$

where the Clebsch-Gordan coefficients $(I'' 0 m_{I''} 0 | s'' m_{s''})$ and

$(I''0m_{I''}0|\bar{s}''\bar{m}_{s''})$ have introduced the factors $\delta_{s''I''}$, $\delta_{m_{s''}m_{I''}}$ and $\delta_{\bar{s}''I''}$, $\delta_{\bar{m}_{s''}m_{I''}}$ respectively. Using the orthogonality property for the Clebsch-Gordan coefficients,

$$\sum_{m_{\ell''}\, m_{I''}} (I''\ell''m_{I''}m_{\ell''}|I'm_{I'})\ (I''\ell''m_{I''}m_{\ell''}|I'\bar{m}_{I'}) = \delta_{m_{I'},\bar{m}_{I'}} \qquad \text{(A.3.13)}$$

the integral can be expressed in a very simple form:

$$\sum_{\ell''} |S^{I'}_{s''\ell''}|^2 \times \int d\Omega_1 \{ \sum_{\substack{m_i\, m_I \\ m_{i'}\, m_{I'}}} |\mathrm{Tr}(m_i m_I, m_{i'} m_{I'}; \Omega_1)|^2 \} \qquad \text{(A.3.14)}$$

where the expression in curly brackets is proportional to the differential cross-section $d\sigma_1(\Omega_1)/d\Omega_1$ for the formation of the state in ^{18}F. Then, grouping all the real and positive normalisation constants into γ $(\gamma \varepsilon R > 0)$, replacing (A.3.14) into (A.3.7) we obtain:

$$\sum_{\ell''} |S^{I'}_{s''\ell''}|^2 \times \sigma_1(\text{formation}) = \gamma\sigma_1(\text{formation}) \frac{\Gamma^{\alpha}}{\Gamma_{tot}} \qquad \text{(A.3.15)}$$

which gives:

$$\sum_{\ell''} |S^{I'}_{s''\ell''}|^2 = \gamma \frac{\Gamma^{\alpha}}{\Gamma_{tot}} = \gamma \frac{(\sum_{\ell''} \Gamma^{\alpha}_{\ell''})}{\Gamma_{tot}} \qquad \text{(A.3.16)}$$

For the case in which only one ℓ'' contributes, substituting (A.3.5) into (A.3.16) we can express the decay matrix in terms of the coefficients of fractional parentage and the single particle widths

$$S^{I'}_{s''\ell''} = M\,\gamma\,C^{\alpha}_{\ell''}\frac{(\Gamma^{\alpha}_{sp,\ell''})^{\frac{1}{2}}\,e^{i\phi}}{(\Gamma_{tot})^{\frac{1}{2}}} \qquad \text{(A.3.17)}$$

where $e^{i\phi}$ carries a phase. When two ℓ'' values are considered, we can see from eq. A.3.16 that the $S^{I'}_{s''\ell''}$ matrix must satisfy

$$\sum_{\ell''}\left|\frac{S^{I'}_{s''\ell''}}{(\gamma\Gamma^{\alpha}/\Gamma_{tot})^{\frac{1}{2}}}\right|^2 = 1 \qquad \text{(A.3.18)}$$

As $\dfrac{\gamma\Gamma^{\alpha}}{\Gamma_{tot}}$ is a real factor common to all ℓ'' contributions, it will not affect the structure of the angular correlation function $W(\Omega_1,\Omega_2)$, acting only as a normalisation constant. It will be possible then to estimate how different complex $S^{I'}_{s''\ell''}$ values which comply with the requirement

$$|S^{I'}_{s''\ell''_1}|^2 + |S^{I'}_{s''\ell''_2}|^2 = 1 \qquad \text{(A.3.19)}$$

influence in the final angular correlation shape. In this thesis, when two orbital angular momenta ℓ'' are required for a theoretical calculation, different values of $S^{I'}_{s''\ell''}$ have been used in the range given by equation (A.3.19), and with phases given by $\phi=0$, $\pi/2$, π and $3\pi/2$. The theoretical angular correlations have been compared to the experimental data with a χ^2 test, and the values for the best fit used in the final chi-square comparison.

APPENDIX B

Application of the DWBA Theory to Cluster Transfer Reactions

The distorted wave Born approximation (DWBA) gives a general and simple quantum mechanical approach for describing direct reaction processes. It provides approximate methods to obtain the wave function which describes the relative motion of two interacting nuclear systems. The basic direct reaction models start formulating the Schroedinger equation for the stationary-state wave function that describes the intervening nuclei in the asymptotic region [AUS70] . This stationary-state wave function is expressed as a linear combination of channel wave functions obtained by considering all possible relevant break up modes of the system into two separated nuclei.

$$H\,\Psi^{+} = E\,\Psi^{+} \tag{B.1}$$

with:

$$\Psi^{+} = \sum_{\gamma} \Phi_{c\gamma}\, \Phi_{C\gamma}\, \xi_{\gamma}(\vec{r}_{\gamma}) = \sum_{\gamma} \Psi_{\gamma}\, \xi_{\gamma}(\vec{r}_{\gamma}) \tag{B.2}$$

where $\Phi_{c\gamma}$ and $\Phi_{C\gamma}$ describes the internal wave functions of the participating nuclei (thus depending only on internal coordinates $\vec{\eta}_{\gamma}$) and ξ_{γ} the wave function of the relative motion between the two nuclei c and C in a particular channel γ (thus depending on the displacement between the centres of mass of c and C: $\vec{r}_{\gamma}$). Equation (B.1) is projected onto the internal wave function in channel β (Ψ_{β}) (with mass partition b and B), a local distorting potential ($U_{\beta}(\vec{r}_{\beta})$) is introduced, and by using Green's function techniques [AUS70] the transition amplitude for the scattering from channel α (entrance channel) to channel β (exit channel) can be obtained.

$$T_{\alpha\beta} = \langle \chi_\beta^{(-)} \Psi_\beta | V_\beta(\vec{r}_\beta, \vec{\eta}_\beta) - U_\beta(\vec{r}_\beta) | \sum_\gamma \Phi_{c_\gamma} \Phi_{C_\gamma} \xi_\gamma(\vec{r}_\gamma) \rangle \qquad (B.3)$$

where $\chi_\beta^{(-)}$ is the elastic scattering wave function governed by the potential U_β and V_β represents the two body interactions in channel β (not internal to nuclei b or B). Equation (B.3) is known as the post form of the reaction amplitude because it is based on the interaction in the exit channel. The distorted wave Born approximation emphasizes the role played by the entrance channel $\gamma = \alpha$, and splits equation (B.3) into two parts:

$$T_{\alpha\beta} = \langle \chi_\beta^{(-)} (\vec{r}_\beta) \Psi_\beta | V_\beta - U_\beta | \Phi_a \Phi_A \xi(\vec{r}_\alpha) \rangle + \\ + \langle \chi_\beta^{(-)} (\vec{r}_\beta) \Psi_\beta | V_\beta - U_\beta | \sum_{\gamma \neq \alpha} \Phi_{c\gamma} \Phi_{C\gamma} \xi_\gamma (\vec{r}_\gamma) \rangle \qquad (B.4)$$

The second term on the right hand side is neglected in the DWBA under the assumption that the coupling for the incident channel is greater than for the rest of the channels, and equation (B.4) reduces to:

$$T_{\alpha\beta} = \langle \chi_\beta^{(-)} (\vec{r}_\beta) \Psi_\beta | V_\beta - U_\beta | \Psi_\alpha \xi_\alpha (\vec{r}_\alpha) \rangle \qquad (B.5)$$

Here the DWBA introduces approximate methods for obtaining the relative wave function ξ_α. It approximates $\xi_\alpha(\vec{r}_\alpha)$ by the distorted wave function $\chi_\alpha^{(+)}(\vec{r}_\alpha)$ calculated from an optical potential (U_α).

$$T_{\alpha\beta} = \langle \chi_\beta^{(-)} (\vec{r}_\beta) \Psi_\beta | V_\beta - U_\beta | \Psi_\alpha \chi_\alpha^{(+)} (\vec{r}_\alpha) \rangle \qquad (B.6)$$

This optical potential is chosen so as to reproduce the elastic scattering in the entrance channel, and in general is a simple function of the relative distance between the centres of the colliding pair, containing no reference to internal degrees of freedom. It could be argued that this simple dependence is unreasonable for two heavy ions, since when the ions overlap the true wave functions would present a much more complicated many body problem with obvious dependence on internal coordinates. Due to strong absorption and Coulomb repulsion the direct reactions tend to be peripheral, thus taking place while the ions do not significantly overlap, and in this region the optical potentials give good account of the wave function of relative motion. The optical potential is complex, its imaginary part corresponds to any loss of flux from the elastic channel.

Out of the two assumptions made by the DWBA, the use of the distorted $\chi_\alpha^{(+)}(\vec{r}_\alpha)$ function for representing $\xi_\alpha(\vec{r}_\alpha)$ is the most accurate one. The two wave functions may differ inside the nucleus (uncertainties in details of the optical potentials) but they must be identical in the external region since they describe the same elastic scattering in channel α. Neglecting the second term on the right hand side of equation (B.4) is a more drastic assumption which implies that the transfer must go directly from the entrance to the exit channel in one step. The accuracy of the DWBA treatment will then be determined by the strength of the elastic channel relative to the other open channels.

It is important to obtain numerical evaluations of equation (B.6) in order to compare the predictions of the DWBA theory with the experimental cross sections. Expression (B.6) involves integration over the space of $\vec{r}_\alpha$ and $\vec{r}_\beta$, and this implies the evaluation of a six dimensional integral. Zero range or no-recoil approximations are often employed in order to reduce the numerical complexities of the six dimensional integration to a three dimensional integral. When heavy ions are involved in a reaction, neither zero range nor no-recoil approximations are valid and finite range treatment including recoil have to be carried out.

Let us picture our cluster (x) transfer A(a,b)B reaction with heavy ions by the diagram showed in figure B.1. With this coordinate system, the DWBA transition amplitude can be expressed with the integration over the spacial coordinates displayed:

$$T^{DWBA}_{\alpha\beta} = J_{\alpha\beta} \int d\vec{r}_\alpha \int d\vec{r}_\beta \chi^{(-)*}_\beta (\vec{k}_\beta, \vec{r}_\beta) \langle \Phi_B \Phi_b | \Delta V | \Phi_a \Phi_A \rangle \chi^{(+)}_\alpha (\vec{k}_\alpha, \vec{r}_\alpha) \quad (B.7)$$

where $J_{\alpha\beta}$ is the jacobean of the transformation from the coordinates $\vec{r}_\beta$, $\vec{r}_{Ax}$ to $\vec{r}_\beta$, $\vec{r}_\alpha$; $\Delta V = V_\beta(\vec{\eta}_\beta, \vec{r}_\beta) - U(\vec{r}_\beta)$ and $\langle \Phi_B \Phi_b | \Delta V | \Phi_a \Phi_A \rangle$ involves integrals over coordinates independent of $\vec{r}_\alpha$, $\vec{r}_\beta$. If the spins of the participating particles in the reaction are designated J_A, s_a, s_b and J_B with projections M_A, m_a, m_b and M_B respectively, the ΔV matrix element of equation (B.7) can be written:

$$\langle \Phi_B \Phi_b | \Delta V | \Phi_a \Phi_A \rangle = \langle J_B M_B s_b m_b | \Delta V | J_A M_A s_a m_a \rangle \quad (B.8)$$

It is very common [AUS64] to express the matrix element in a multipole expansion, where each term corresponds to the transfer to the target nucleus of an angular momentum $\vec{j}$, composed of a spin $\vec{s}$ and an orbital part $\vec{\ell}$, according to the vector coupling:

$$\vec{j} = \vec{J}_B - \vec{J}_A \ , \ \vec{s} = \vec{s}_a - \vec{s}_b \ , \ \vec{j} = \vec{\ell} + \vec{s} \quad (B.9)$$

The matrix element of equation (B.8) then becomes [AUS64]:

$$J_{\alpha\beta} \langle J_B M_B s_b m_b | \Delta V | J_A M_A s_a m_a \rangle =$$

$$= \sum_{\ell s j} i^{-\ell} G_{\ell s j, m}(\vec{r}_\beta, \vec{r}_\alpha; bB, aA) (-)^{s_b - m_b} \langle J_A j M_A (M_B - M_A) | J_B M_B \rangle \times$$

$$\times \langle s_a s_b m_a (-m_b) | s (m_a - m_b) \rangle \langle \ell s m (m_a - m_b) | j (M_B - M_A) \rangle \quad (B.10)$$

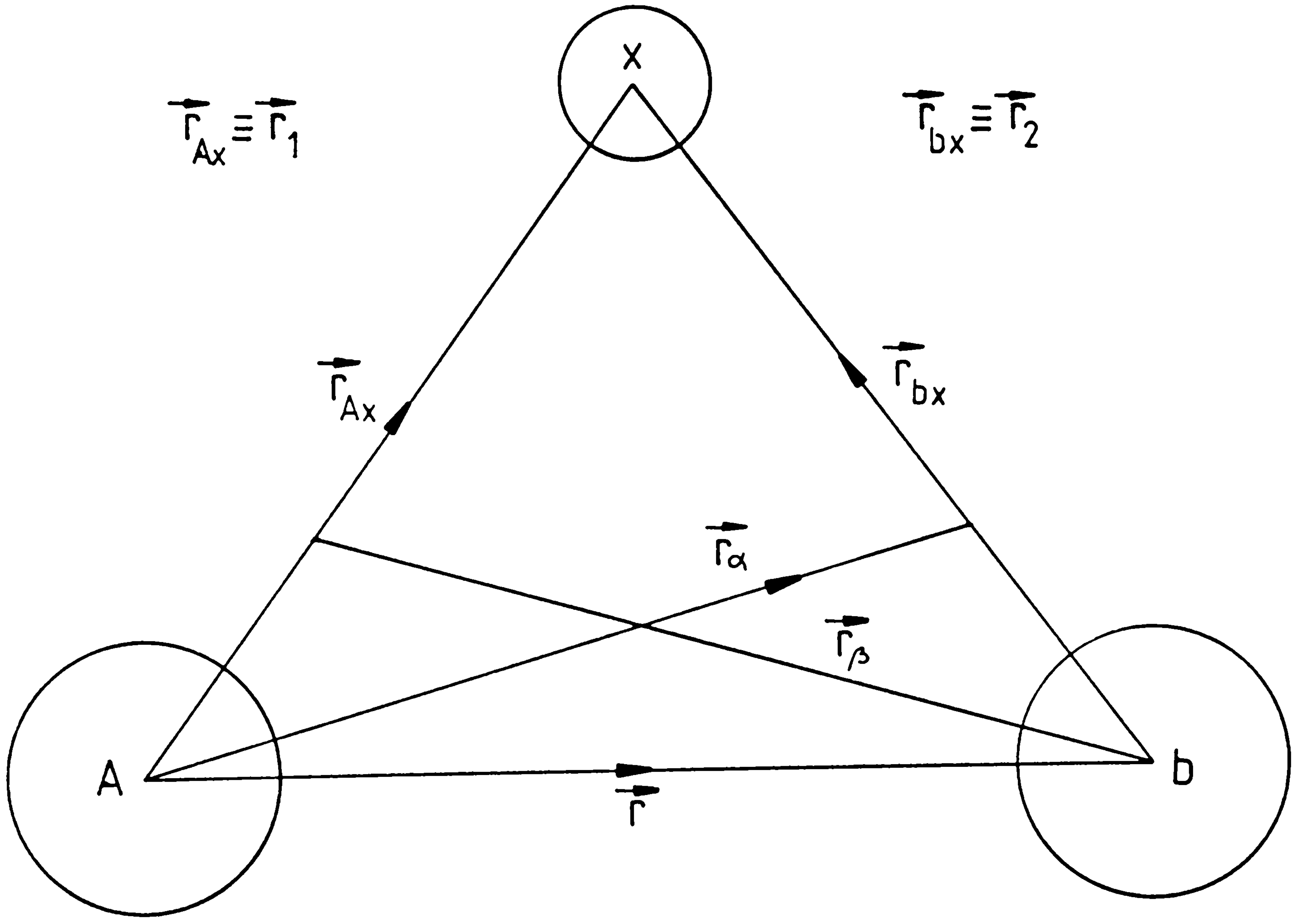

Figure B.1 Coordinate system for cluster transfer where $m=M_B+m_b-M_A-m_a$ and $G_{\ell sj,m}$ can be written as a product of two factors, a spectroscopic coefficient $A_{\ell sj}$ and a form factor $f_{\ell sj,m}$. Replacing equation (B.10) into equation (B.7), the transition amplitude is written as a sum over multipole contributions:

$$T_{\alpha\beta}^{DWBA} = \sum_{\ell s j} (2\ell+1)^{\frac{1}{2}} A_{\ell sj} (-)^{s_b-m_b} \langle J_A j M_A (M_B-M_A) | J_B M_B \rangle \times$$

$$\times \langle \ell s m (m_a-m_b) | j (m-m_b+m_a) \rangle \langle s_a s_b m_a (-m_b) | s (m_a-m_b) \rangle \; \beta_{sj}^{\ell m}(\Theta) \qquad \text{(B.11)}$$

where the reduced amplitude $\beta_{sj}^{\ell m}$ has been introduced,

$$(2\ell+1)^{\frac{1}{2}} i^{\ell} \beta_{sj}^{\ell m} = \int d\vec{r}_\alpha \int d\vec{r}_\beta \quad \chi_\beta^{(-)*}(\vec{k}_\beta, \vec{r}_\beta) \times$$

$$\times f_{\ell sj,m}(\vec{r}_\beta, \vec{r}_\alpha) \; \chi_\alpha^{(+)} (\vec{k}_\alpha, \vec{r}_\alpha) \qquad \text{(B.12)}$$

The expression for the differential cross section in terms of the reduced amplitudes is [AUS64]:

$$\frac{d\sigma}{d\Omega} = \frac{\mu_\alpha \mu_\beta}{(2\pi\hbar^2)^2} \frac{k_\beta}{k_\alpha} \frac{2J_B+1}{2J_A+1} \sum_{\ell s j} \frac{|A_{\ell sj}|^2}{2s_a+1} \sum_{m} |\beta_{sj}^{\ell m}(\Theta)|^2 \qquad \text{(B.13)}$$

where μ_α and μ_β are the reduced masses of the pairs (a,A) and (b,B) respectively. The finite range calculation consists then in evaluating the reduced amplitudes of equation (B.12). For that purpose, the distorted waves χ_α and χ_β are expressed in partial-wave expansions, and $f_{\ell sj,m}$ written in terms of spherical harmonics of $\hat{r}_\alpha$ and $\hat{r}_\beta$. The reduced amplitude $\beta^{\ell m}_{sj}$ is transformed finally by a partial wave expansion:

$$\beta^{\ell m}_{sj}(\Theta) = \frac{4\pi}{k_\alpha k_\beta} \sum_{\substack{L_\alpha \\ L_\beta}} i^{L_\alpha+L_\beta-\ell} \, (2L_\beta+1)^{\frac{1}{2}} \, \langle L_\beta \ell m(-m) | L_\alpha 0\rangle \times$$

$$\times \, \{(L_\beta-m)!/(L_\beta+m)!\}^{\frac{1}{2}} \, P^m_{L_\beta}(\Theta) \, I^{\ell}_{L_\alpha L_\beta} \qquad \text{(B.14)}$$

The radial integral $I^{\ell}_{L_\alpha L_\beta}$ is:

$$I^{\ell}_{L_\alpha L_\beta} = \int r_\alpha \, dr_\alpha \int r_\beta \, dr_\beta \chi^{(-)}_{L_\beta}(k_\beta, r_\beta) \times$$

$$\times \, F_{\ell L_\beta L_\alpha}(r_\beta, r_\alpha) \chi^{(+)}_{L_\alpha}(k_\alpha, r_\alpha) \qquad \text{(B.15)}$$

and the two dimensional form factor $F_{\ell L_\beta L_\alpha}$ is [DeV73]:

$$F_{\ell L_\beta L_\alpha}(r_\beta, r_\alpha) = \frac{1}{2} \sum_{\substack{\lambda_1 \\ \lambda_2 \\ K}} (v_1 r_\alpha)^{\ell_1-\lambda_1} (t_1 r_\beta)^{\lambda_1} (v_2 r_\alpha)^{\lambda_2} (t_2 r_\beta)^{\ell_2-\lambda_2} \times$$

$$\times \, g_K(r_\beta, r_\alpha) \sum_{\Lambda_\alpha \Lambda_\beta} (-)^{L_\beta+\ell_2+\lambda_2-\lambda_1} \, (2\ell_1+1)(2\ell_2+1)(2K+1) \times$$

$$\times [(2\Lambda_\alpha+1)(2\Lambda_\beta+1)]^{\frac{1}{2}} \langle \Lambda_\alpha K 0 0 | L_\alpha 0\rangle \langle \Lambda_\beta K 0 0 | L_\beta 0\rangle \times$$

$$\times \langle (\ell_1-\lambda_1)\lambda_2 0 0 | \Lambda_\alpha 0\rangle \langle (\ell_2-\lambda_2)\lambda_1 0 0 | \Lambda_\beta 0\rangle \, W(L_\alpha L_\beta \Lambda_\alpha \Lambda_\beta ; \ell K) \times$$

$$\times \begin{pmatrix} 2\ell_1 \\ 2\lambda_1 \end{pmatrix}^{1/2} \begin{pmatrix} 2\ell_2 \\ 2\lambda_2 \end{pmatrix}^{1/2} \begin{Bmatrix} \ell & \ell_1 & \ell_2 \\ \Lambda_\alpha & (\ell_1-\lambda_1) & \lambda_2 \\ \Lambda_\beta & \lambda_2 & (\ell_2-\lambda_2) \end{Bmatrix} \qquad \text{(B.16)}$$

with $g_K(r_\beta, r_\alpha)$ defined in terms of radial wave functions by:

$$g_K(r_\beta, r_\alpha) = \int du\ P_K(u) \frac{U_1^*(r_1)}{r_1^{\ell_1}} \Delta V \frac{U(r_2)}{r_2^{\ell_2}} \tag{B.17}$$

and u=cos(Φ) where Φ is the angle between r_α and r_β. Following figure B.1, r_1 and r_2 are obtained,

$$\begin{aligned} \vec{r}_1 &= s_1\vec{r}_\alpha + t_1\vec{r}_\beta \\ \vec{r}_2 &= s_2\vec{r}_\alpha + t_2\vec{r}_\beta \end{aligned} \tag{B.18}$$

where $s_1 = \delta$, $t_1 = -\delta\gamma$, $s_2 = \delta\varepsilon$, $t_2 = -\delta$, and for the reaction A(a,b)B where a cluster x is transferred, $\delta = (aB/((A+a)x))$, $\gamma = b/a$, $\varepsilon = A/B$. The summations in equation (B.16) are limited by the following angular momentum inequalities:

$$\begin{gathered} \Delta(L_\alpha\ \Lambda_\alpha\ K) \qquad \Delta(\Lambda_\alpha\ (\ell_1-\lambda_1)\ \lambda_2) \qquad \Delta(L_\beta\ \Lambda_\beta\ K) \\ \Delta(\ell\ L_\alpha\ L_\beta) \qquad \Delta(\ell\ \ell_1\ \ell_2) \qquad \Delta(\ell\ \Lambda_\alpha\ \Lambda_\beta) \\ \Delta(\Lambda_\beta\ (\ell_2-\lambda_2)\ \lambda_1) \end{gathered} \tag{B.19}$$

Although expression (B.16) looks rather complicated, it is relatively easy to evaluate numerically, since the form factor calculation has been reduced to an integration over an angular variable (see B.17). Expressions (B.14), (B.15) and (B.16) are evaluated by the computer code LOLA, which first computes the bound state functions ($U_1(r_1)$ and $U_2(r_2)$) and then integrates them in the kernel calculation of equation (B.17). When unbound state wave functions are required, Gamow states are read from disk for the kernel computation.

APPENDIX C

Unbound States

C.1 Gamow Functions and Cross Sections

As a result of a transfer reaction, bound states formed in the final nucleus appear as peaks in the energy spectrum of the outgoing ejectile. Long lived resonant states of the final nucleus which are unstable with respect to the decay of the transferred cluster x, are also seen as peaks in the outgoing ejectile spectrum. Many of the states observed in the transfer spectra presented in this thesis are resonant 'quasi-bound' states. In order to understand how these states arise, let us consider a typical radial form of a nuclear + Coulomb α-^{14}N potential for an $\ell = 8$ state as shown in figure C.1. If the energy of the cluster relative to the core (E) is negative, we are facing typical cases of bound states, where a finite number of energy eigenvalues will be allowed. In the case in which E falls between 0 and E_B (the highest value of the barrier) we will still have a finite number of allowed eigenstates, but these states will be unstable against emission of the transferred cluster (x). These are the 'quasi-bound' states we have referred to.

Many authors have given different approaches to how to treat these particular states. The normalization of the resonant wave function and subsequently the convergency of the DWBA transition amplitude for the transfer reaction involved have been object of numerous studies [COK73, BUN64, VIN70, COK73a, BER68, BAN69 GYA70, BER72]. In order to represent the unbound state wave function, the simplest approach very commonly

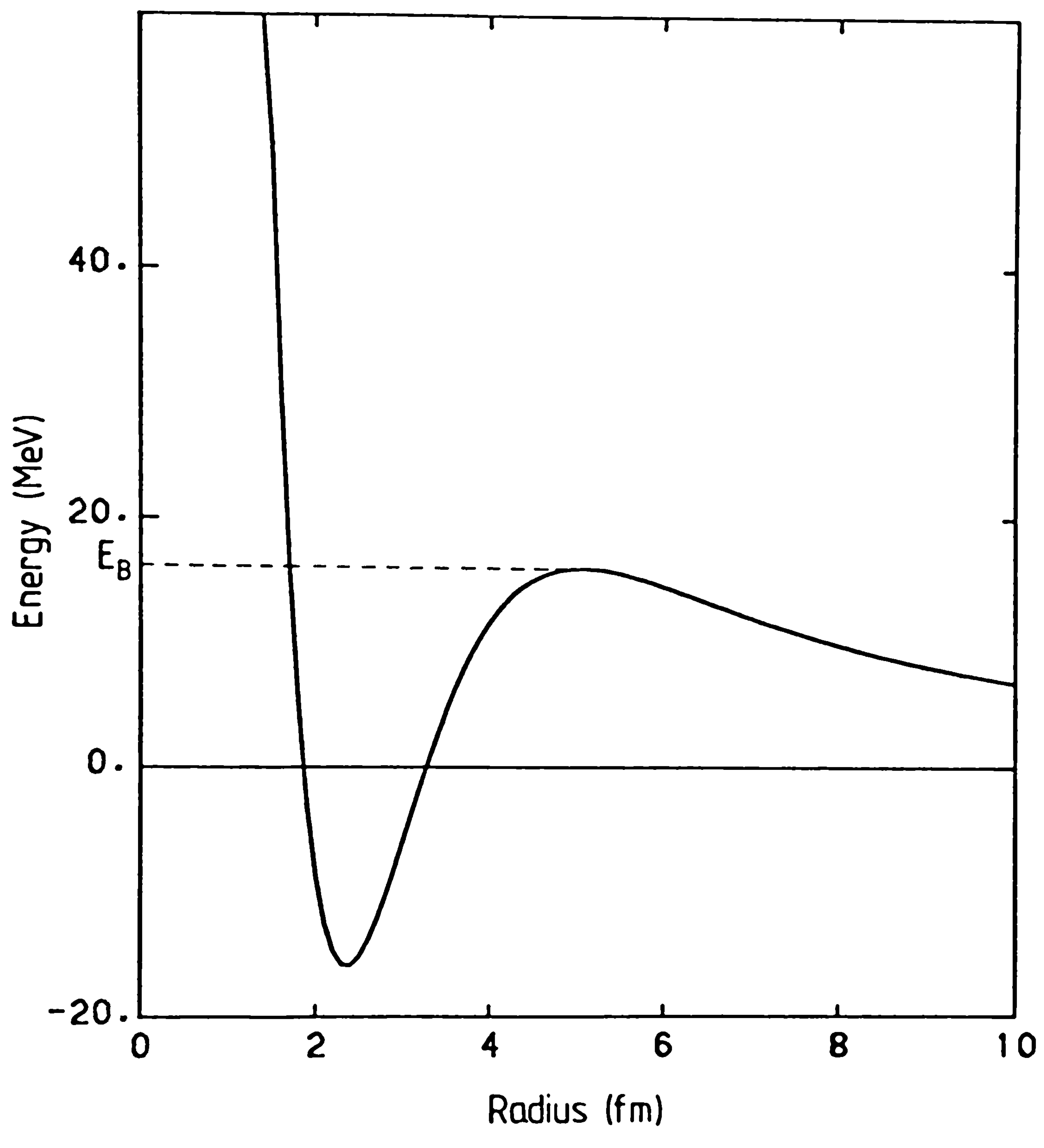

Figure C.1 Radial dependence of a nuclear plus Coulomb α-^{14}N potential for an ℓ=8 cluster state.

used is to treat the state as 'slightly bound', and then to use a small ($\sim$-0.1MeV) binding energy. A more elaborated approach presented by Coker and Hoffmann [COK73] using Gamow functions to describe the unbound state in the residual nucleus, has been followed in this thesis. The advantage of this method is that the unbound state can be treated spectroscopically in a similar way as it is done for the bound state cases. This fact will be shown in the following discussion, where the notation of Coker and Hoffmann is used.

The Gamow functions are obtained solving the eigenvalue problem for complex energy ($\tilde{E}$)

$$[\ (-\hbar^2/2\mu)\ (d^2/dr^2\ -\ell(\ell+1)/r^2)-\ \tilde{E}\ +\ U_{\ell j}(r)\ ]\ g_{\ell j}(r)\ =\ 0 \qquad (C.1.1)$$

of a system of reduced mass μ and with boundary condition at infinity of purely outgoing waves:

$$g_{\ell j}(r)\ \text{-->}\ [2\mu\Gamma/\hbar^2\tilde{k}]^{\frac{1}{2}}\ \{G_\ell(r,\tilde{k})+\ i\ F_\ell(r,\tilde{k})\} \qquad (C.1.2)$$

where G_ℓ and F_ℓ are the regular and irregular Coulomb functions respectively, and Γ stands for the imaginary part of the complex energy

$$\tilde{E} = E - i\ \Gamma/2 \qquad (C.1.3)$$

and $\tilde{k}$ is the complex wave number given by:

$$\tilde{k}\ =\ [\ 2\mu(E-i\Gamma/2)/\hbar^2\ ]^{\frac{1}{2}} \qquad (C.1.4)$$

The Gamow state is defined as [COK73a]

$$g_{\ell j}(r,\tilde{k})\ =\ (\mu\Gamma/\hbar^2\tilde{k})^{\frac{1}{2}}\ e^{i\eta}\ O_{\ell j}(r,\tilde{k}) \qquad (C.1.5)$$

where η is the so called 'background' phase shift and $O_{\ell j}$ is the solution of the Schroedinger equation for $\tilde{E}$ and which correspond to a purely outgoing wave at infinity. Coker and Hoffmann have shown that these complex energy wave functions have normalization and orthogonality properties similar to those for bound states and that they may be used as part of the eigenstate expansion of a complete basis set for the unbound system.

The cross section for a stripping process in which a cluster x is transferred to an unstable state (with respect to x) in the residual nucleus, at an energy between E and E+dE is (as given in Appendix B):

$$\frac{d^2\sigma}{d\Omega dE} = \frac{2\mu}{\pi\hbar^2\tilde{k}} \frac{\mu_\alpha\mu_\beta}{(2\pi\hbar^2)^2} \frac{k_\beta}{k_\alpha} \frac{(2J_B+1)}{(2J_A+1)} \sum_{\ell sj} \frac{|A_{\ell sj}|^2}{2s_a+1} \sum_m |\beta^{\ell m}_{sj}|^2 \qquad (C.1.6)$$

for the reaction A(a,b)B with B=A+x and a=b+x. The expression for the reduced amplitudes $\beta^{\ell m}_{sj}$ (see Appendix B) involves radial overlap integrals which include the relative wave function between A and x. Near a resonance, this scattering state wave function is given by [COK73a]:

$$\chi_{\ell j}(r,\tilde{k}) = - \frac{e^{i(\sigma\ell+2\eta)}(\Gamma/2)}{(E-E_R)+i\Gamma/2} O_{\ell j}(r,\tilde{k}) + \chi^{NR}_{\ell j}(r,\tilde{k}) \qquad (C.1.7)$$

where σ is the Coulomb phase shift and $\chi^{NR}_{\ell j}(r,\tilde{k})$ is the non resonant wave function. With the assumption that near a resonance, $\chi^{NR}_{\ell j}$ can be neglected since the (a,xb) breakup reaction contribution is approximately subtracted in the data analysis, it is possible to express $\chi_{\ell j}$ in terms of the Gamow functions by introducing the factor $(2\mu/\pi\hbar^2\tilde{k})^{\frac{1}{2}}$:

$$\chi_{\ell j}(r,\tilde{k}) = - \frac{e^{i(\sigma\ell+\eta)}(\Gamma/2\pi)^{\frac{1}{2}}}{(E-E_R)+i\Gamma/2} g_{\ell j}(r,\tilde{k}) \qquad (C.1.8)$$

The differential cross section of equation (C.1.6) can then be written:

$$\frac{d\sigma}{d\Omega}=\int_{E_R-\Delta}^{E_R+\Delta} dE\left[\frac{e^{i(\sigma\ell+\eta)}(\Gamma/2\pi)^{\frac{1}{2}}}{(E-E_R)+i\Gamma/2}\right]^2 \frac{\mu_\alpha\mu_\beta}{(2\pi\hbar^2)^2}\,\frac{k_\beta}{k_\alpha}\,\frac{(2J_B+1)}{(2J_A+1)}\sum_{\ell s j}\frac{|A_{\ell sj}|^2}{2s_a+1}\sum_m|\beta_{sj}^{\ell m}|^2 \quad (C.1.9)$$

where now the reduced amplitudes $\beta_{sj}^{\ell m}$ contain overlap integrals identical to the ones defined for the DWBA, but with Gamow wave functions for the unbound state. In order to perform the integral on E we can consider that $g_{\ell j}$ and the distorted waves involved in $\beta_{sj}^{\ell m}$ vary very slow with the energy E, in the small interval 2Δ around E_R. Then, the only factor with a clear strong energy dependence that will determine the integral on E is the one in square brackets in equation (C.1.9). The integral to be calculated is then:

$$\int_{E_R-\Delta}^{E_R+\Delta} dE\left[\frac{e^{i(\sigma\ell+\eta)}(\Gamma/2\pi)^{\frac{1}{2}}}{(E-E_R)+i(\Gamma/2)}\right]^2 = (\Gamma/2\pi)\int_{E_R-\Delta}^{E_R+\Delta}\frac{dE}{(E-E_R)+\Gamma^2/4} =$$

$$=\frac{\Gamma}{2\pi}\,\frac{2}{\Gamma}\,\mathrm{arctg}\left(\frac{E-E_R}{(\Gamma/2)}\right)\Big|_{E_R-\Delta}^{E_R+\Delta}=\frac{2}{\pi}\,\mathrm{arctg}\left(\frac{\Delta}{(\Gamma/2)}\right) \quad (C.1.10)$$

The energy range 2Δ will be given [COK73] by the addition of the single particle width of the resonance (Γ) and the energy resolution of the detection system (D)

$$\Delta=(\Gamma+D)/2 \quad (C.1.11)$$

and then, assuming that $\Gamma \ll D$, since we are suppose to be dealing with narrow resonances, arctg(Δ/(Γ/2)) in (C.1.11) is approximately π/2. The integral will be then equal to unity, and the cross section of equation (C.1.6) will show identical form to the usual DWBA estimation, with the only exception that the resonant state in the form factor is described by a Gamow function.

C.2 Convergence of the DWBA Calculations for Unbound States

It is well known that Gamow states diverge exponentially with the radius ($e^{\gamma r}$ when $r \longrightarrow \infty$) [COK73]. The use of Gamow states in the transition amplitude calculation have originated different approaches in order to obtain convergence of the DWBA integrals. Coker [COK73a] and Bang [BAN69] for example, had to weight by a Gaussian factor ($e^{-\alpha r^2}$) the Gamow functions in the zero range (ZR) DWBA integrals, and then require $\alpha \longrightarrow 0$ in order to get the searched convergence. In exact finite range (EFR) DWBA calculations such procedure is not necessary since the interaction potentials included in the form factor integrals can assure the convergence. This was found by Bukanov [BUK70] who overcame the problem transforming the integral on the cluster-core wave function to the prior form. In the following, the conditions for radial convergence of the EFR-DWBA transition amplitudes will be discussed.

It has been shown in Appendix B that the radial dependence of the form factor $F_{\ell L_\alpha L_\beta}(r_\alpha, r_\beta)$ of equation (B.16) is contained in the factors:

$$(s_1 r_\alpha)^{\ell_1 - \lambda_1} (t_1 r_\beta)^{\lambda_1} (s_2 r_\alpha)^{\lambda_2} (t_2 r_\beta)^{\ell_2 - \lambda_2} \, g_K(r_\beta, r_\alpha) \qquad \text{(C.2.1)}$$

where the kernel $g_K(r_\beta, r_\alpha)$ is given by an integral on the radial wave functions $U_1(r_1)$ and $U_2(r_2)$

$$g_K(r_\beta, r_\alpha) = \int du \, P_K(u) \, \frac{U_1^*(r_1)}{(r_1)^{\ell_1}} \, \Delta V \, \frac{U_2(r_2)}{(r_2)^{\ell_2}} \qquad \text{(C.2.2)}$$

With the definition given for r_1 and r_2 in terms of r_α and r_β in equation (B.18), we can see that the multiplicative terms of (C.2.1) will cancel under the effect of $r^{-\ell_1}$ and $r^{-\ell_2}$ in $g_K(r_\beta, r_\alpha)$. The radial dependence that remains to be examined for convergence appears on the factor $U_1^*(r_1)\ \Delta V\ U_2(r_2)$ when $U_1(r_1)$ is a Gamow state (residual nucleus), $U_2(r_2)$ is a bound state (projectile), and where for simplicity the nuclear potential ΔV is considered as having an exponential asymptotic behaviour. The asymptotic dependence of a Gamow state has been given by Coker and Hoffmann [COK73] as:

$$g_{\ell j}(r,\tilde{k}) \xrightarrow[r\to\infty]{} \exp(i(\tilde{k}r - \eta \ln(2\tilde{k}r) - \frac{\ell\pi}{2} + \xi) \qquad \text{(C.2.3)}$$

which can be expressed asymptotically as approximately proportional to $e^{K_1 r}$ where $K_1 = (\mu\Gamma/\hbar^2)^{½}$. In a similar way we can express the asymptotic behaviour of the bound state as

$$U_2(r_2) \xrightarrow[r\to\infty]{} \exp(-K_2 r_2) \qquad \text{(C.2.4)}$$

where $K_2 = (2\nu E/\hbar^2)^{½}$, being E the separation energy of the cluster x in the projectile and ν the reduced mass for the x+b system. When using post representation and for large values of r_1 and r_2, the term $U_1^*(r_1) V_{bx}(r_2) U_2(r_2)$ will be proportional to:

$$e^{K_1 r_1}\ e^{-wr_2}\ e^{-K_2 r_2} \qquad \text{(C.2.5)}$$

where W gives the asymptotic behaviour of $V_{bx}(r_2)$. As r_1 and r_2 are independent vectors, we can consider large values for r_α and r_β where r_1 increases but not r_2. This will cause expression (C.2.5) to diverge for unbound residual states. On the other hand, if we use the prior form in $g_K(r_\beta, r_\alpha)$, and consider all the interaction terms as well (V_{Ax}, V_{Ab} and U_{aA}), we will have:

$$U_1^*\ (r_1)\ V_{Ax}(r_1)\ U_2(r_2) \longrightarrow e^{(K_1 - x) r_1}\ e^{-K_2 r_2}$$
$$U_1^*(r_1)\ V_{Ab}(r)\ U_2(r_2) \longrightarrow e^{K_1 r_1}\ e^{-y|\vec{r}_1 - \vec{r}_2|}\ e^{-K_2 r_2} \qquad \text{(C.2.6)}$$

$$U_1^*(r_1)\ U_{aA}(r_\alpha)\ U_2(r_2) \longrightarrow e^{K_1 r_1}\ e^{-z|\vec{r}_1 - \frac{b}{a}\vec{r}_2|}\ e^{-K_2 r_2}$$

which clearly will converge if x,y and $z > K_1$. In the case of a Woods-Saxon potential the factors w, x y and z which give the asymptotic dependence of the potentials are the inverse of the diffuseness, and this will give figures typically of the order of one fm^{-1} or bigger. On the other hand, the K_1 value for resonances and for the upper limit of 4 for an alpha reduced mass, is 0.33 fm^{-1}. As no resonance wider than or even as wide as 1 MeV is analyzed in this thesis, the nuclear interaction terms will converge for the prior representation.

REFERENCES

AJZ78 F.Ajzenberg-Selove, Nucl.Phys., A300(1978)1

ANA79 N.Anantaraman, H.E.Gove, R.A.Lindgren, J.Toke and J.P.Trentelman, Nucl.Phys., A313(1979)445

ANY74 N.Anyais-Weiss, J.C.Cornell, P.S.Fisher, P.N.Hudson, A.Menchaca-Rocha, D.J.Millener, A.D.Panagiotou, D.K.Scott, D.Strottman, D.M.Brink, B.Buck, P.J.Ellis and T.Engeland, Phys.Rep., C12(1974)203

ARI72 A.Arima and S.Yoshida, Phys.Lett., B40(1972)15

ARM69 D.D.Armstrong, J.G.Beery, E.R.Flynn, W.S.Hall, P.W.Keaton and M.P.Kellogg, Nucl.Inst & Methods, 70(1969)69

ART76 K.P.Artemov, V.Z.Goldberg, I.P.Petrov, V.P.Rudakov, V.A.Timofeev, R.Wolski and J.Szmider, Sov.Jour.Nucl.Phys., 22(1976)125

AUS64 N.Austern, R.Drisko, E.Halbert and G.R.Satchler, Phys.Rev., B3(1964)133

AUS70 N.Austern, 'Direct Nuclear React.Theories', Wiley (1970)

AVR75 M.Avril,M.Lepareux, N.Saunier, A.Foti, G.Pappalardo and A.Strazzeri, Le Jour. de Phys., 36(1975)229

BAC68 D.Bachelier, M.Bernas, C.Detraz, P.Radvanyi and M.Roy, Phys.Lett. 26B(1968)283

BAN69 J.Bang and J.Zimanyi, Nucl.Phys., A139(1969)534

BAY58 B.F.Bayman and A.Bohr, Nucl.Phys., 9(1958/59)596

BER68 T.Berggren, Nucl.Phys., A109(1968)265

BER72 T.Berggren, Phys.Lett., B38(1972)61

BIN73 H.G.Bingham, H.T.Fortune, J.D.Garrett and R.Middleton, Phys.Rev., C7(1973)57

BLA52 J.M.Blatt and L.C.Biedenharn, Rev.of Mod.Phys., 24(1952)258

BRA77 H.S.Bradlow, D.Phil. Thesis, Oxford University (1977) (unpublished)

BRI79 D.M.Brink and G.R.Satchler, 'Angular Momentum', Oxford University Press, (1979)

BUC75 B.Buck, C.B.Dover and J.P.Vary, Phys.Rev., C11(1975)1803

BUC77 B.Buck and A.A.Pilt, Nucl.Phys., A280(1977)133

BUC77a B.Buck, H.Friedrich and A.A.Pilt, Nucl.Phys., A290(1977)205

BUC79 B.Buck, A.C.Merchant, N.Rowley, Nucl.Phys., A327(1979)29

BUK70 V.E.Bukanov, Nucl.Phys., A140(1970)241

COB77 M.E.Cobern and P.D.Parker, Phys.Rev., C15(1977)1929

COH71 B.L.Cohen, 'Concepts of Nuclear Physics', McGraw-Hill (1971)

COK73 W.R.Coker, Phys.Rev., C7(1973)2426

COK73a W.R.Coker and G.W.Hoffmann, Z.fur Physik, 263(1979)445

COT76 S.R.Cotanch and C.M.Vincent, Phys.Rev., C14(1976)1739

CUN81 A.Cunsolo, A.Foti, G.Imme, G.Pappalardo and G.Raciti, Phys.Rev., C24(1981)476

CUN81a A.Cunsolo, A.Foti, G.Imme, G.Pappalardo and G.Raciti, Phys.Rev., C24(1981)2127

DaS76 E.F.Da Silveira, 'Contribution to XIV Winter Meeting on Nuclear Physics', Bormio (1976)

DAV63 R.H.Davies, 'Proc.Third Conf.React.between Complex Nuclei', (Univ.of California Press) (1963)61

DEH70 D.Denhard and H.M.Hintz, Phys.Rev., C1(1970)460

DeV73 R.M.DeVries, computer code LOLA (unpublished - see DeV73a)

DeV73a R.M.DeVries, Phys.Rev., C8(1973)951

DeV75 R.M.DeVries, Phys.Rev., C11(1075)2105

EIC73 H.Eichner, H.Stehle and P.Heiss, Nucl.Phys., A205(1973)249

FIT67 W.Fitz, R.Jahr and R.Santo, Nucl.Phys., A101(1967)449

GLO65 R.N.Glover and A.D.W.Jones, Phys.Lett., 16(1965)69

GOD79 N.S.Godwin and W.D.M.Rae, Oxford Shell Model Code (unpublished)

GYA70 B.Gyarmati, T.Vertse, J.Zimanyi and M.Zimanyi, Phys.Rev., C1(1970)1

HAM76 M.Hamm, Ph.D. Thesis, Texas A & M University, (1976) (unpublished)

HAN68 L.F.Hansen, M.L.Stelts, J.G.Vidal, J.J.Wesolowski and V.A.Madsen, Phys.Rev., 174(1968)1155

HAS67 H.Hasegawa and S.Nagata, Prog.Theor.Phys., 38(1967)1188

ICH73 M.Ichimura, A.Arima, E.C.Halbert and T.Terasawa, Nucl.Phys., A204(1973)225

KAM69 T.Kammuri and H.Yoshida, Nucl.Phys., A129(1969)265

KUB72 K.I.Kubo and M.Hirata, Nucl.Phys., A187(1972)186

KUR73 D.Kurath, Phys.Rev., C7(1973)1390

KUR75 D.Kurath and D.J.Millener, Nucl.Phys., A238(1975)269

LAM71 J.M.Lambert, P.A.Treado, D.Haddad, R.A.Moyle and J.C.Sessler, Phys.Rev.Lett., 27(1971)820

LAN60 L.D.Landau and E.M.Lifshitz, 'Mecahnics', Pergamon Press, (1960)

LAN72 J.Lang, J.F.Valley, R.Muller and P.Marmier, Phys.Rev.Lett., (28(1972)623

LIT61 A.E.Litherland and A.J.Ferguson, Can.J.Phys., 39(1961)788

LUT63 H.F.Lutz, J.B.Mason and M.D.Karvelis, Nucl.Phys., 47(1963)521

MAR68 J.B.Marion and F.C.Young, 'Nuclear Reaction Analysis Graphs and Tables', North Holl., (1968)

MAR78 L.M.Martz, D.Phil Thesis, Yale University (1978) (unpublished)

MEI68 K.Meier-Ewert, K.Bethge and K.O.Pfeiffer, Nucl.Phys., A110(1968)142

MID68 R.Middleton, L.M.Polsky, C.H.Holbrow and K.Bethge, Phys.Rev.Lett. 21(1968)1398

MOS59 M.Moshinsky, Nucl.Phys., A13(1959)104

PAN74 A.D.Panagiotou, J.C.Cornell, N.Anyas-Weiss, P.N.Hudson, A.Menchaca-Rocha, D.K.Scott and B.E.F.Macefield, Jour.Phys., 7(1974)1748

PER76 C.M.Perey and F.G.Perey, Atomic Data & Nuclear Data Tables 17(1976)1

RAE77 W.D.M.Rae and N.S.Godwing, DWAVF Oxford code (unpublished)

REE73 B.S.Reehal and B.H.Wildenthal, Part. & Nuclei, 6(1973)137

ROL73 C.Rolfs, H.P.Trautvetter, R.E.Azuma and A.E.Litherland, Nucl.Phys., A199(1973)289

ROO65 J.R.Rook, Nucl.Phys., 61(1965)219

ROW77 N.Rowley, Phys.Lett., B69(1977)25

SAT60 G.R.Satchler, Nucl.Phys., 18(1960)110

SAT74 G.R.Satchler, Proc.Int.Conf. on Rections between Complex Nuclei, Nashville, 2(1974)59

SMI71 W.R.Smith, Phys.Lett., 34B(1971)252

STO72 R.G.Stokstad, Wright Nuclear Struct. Research Lab., Int.Rep.52 Yale University (1972) (unpublished)

SWI73 R.DeSwiniarski, A.Genoux-Lubain, G.Bagieu, J.F.Cavaignac D.H.Worledge and J.Raynal, Phys.Lett., 43B(1973)27

TAM69 T.Tamura, Phys.Rep., 14(1974)59

TAM74 T.Tamura and K.S.Low, Comp.Phys.Comm., 8(1974)349

THO67 D.R.Thompson and Y.C.Tang, Phys.Rev., 159(1967)806

TOB61 W.Tobocman, 'Theory of direct Nuclear Reactions', Oxford University Press, (1961)

TOB73 W.Tobocman, R.Ryan, A.J.Baltz and S.H.Kahana, Nucl.Phys., A205(1973)193

VIN70 C.M.Vincent and H.T.Fortune, Phys.Rev., C2(1970)782

WIG47 E.P.Wigner and L.Eisenbud, Phys.Rev., 72(1947)29

WOO81 C.L.Woods, D.Phil Thesis, Oxford University (1981) (unpublished)

YOU70 A.M.Young, S.L.Blatt and R.G.Seyler, Phys.Rev.Lett., 25(1970)1764